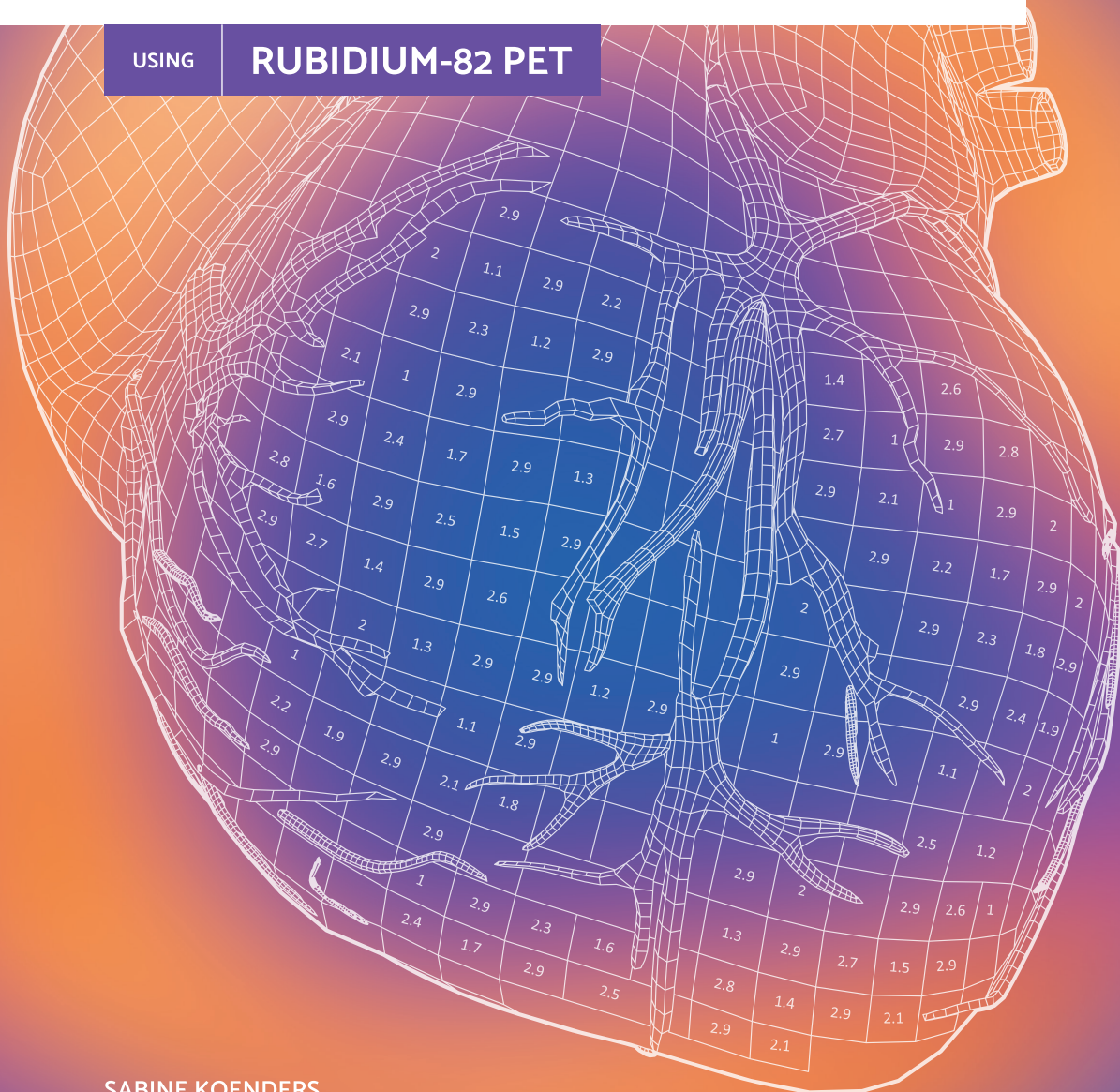


# MYOCARDIAL BLOOD FLOW QUANTIFICATION

USING

RUBIDIUM-82 PET



SABINE KOENDERS





MYOCARDIAL BLOOD  
FLOW QUANTIFICATION  
USING RUBIDIUM-82 PET

SABINE SUSANNA KOENDERS

## **Graduation committee**

### *Chairman and secretary*

Prof. dr. J.N. Kok (University of Twente)

### *Supervisor*

Prof. dr. ir. C.H. Slump (University of Twente)

### *Co-supervisor*

Dr. J.D. van Dijk, MSc, MBA (Isala)

Dr. J.A. van Dalen (Isala)

### *Referee*

Dr. M.E. Kamphuis (University of Twente)

### *Committee Members*

Prof. dr. ir. G.J.M. Krijnen (University of Twente)

Prof. dr. R.H.J.A. Slart (University of Twente)

Prof. dr. W.J.G. Oyen (Radboudumc)

Prof. dr. R. Boellaard (Amsterdam UMC)

Cover design: Maartje Kuipers

Printed by: Ipskamp Printing

Lay-out: Maartje Kuipers

ISBN: 978-90-365-5404-6

DOI: 10.3990/1.9789036554046

© 2022 Sabine Susanna Koenders, The Netherlands. All rights reserved. No parts of this thesis may be reproduced, stored in a retrieval system or transmitted in any form or by any means without permission of the author. Alle rechten voorbehouden. Niets uit deze uitgave mag worden vermenigvuldigd, in enige vorm of op enige wijze, zonder voorafgaande schriftelijke toestemming van de auteur.

Financial support by the foundation Nucleaire Geneeskunde Isala, University of Twente (Technical Medical Centre), the Zwolle Research Foundation (WMI) and The Dutch Heart Foundation for publication of this thesis is gratefully acknowledged.

# MYOCARDIAL BLOOD FLOW QUANTIFICATION USING RUBIDIUM-82 PET

PROEFSCHRIFT

ter verkrijging van  
de graad van doctor aan de Universiteit Twente,  
op gezag van de rector magnificus,  
prof. dr. ir. A. Veldkamp,  
volgens besluit van het College voor Promoties  
in het openbaar te verdedigen  
op vrijdag 30 september 2022 om 14.45 uur

door

**SABINE SUSANNA KOENDERS**

geboren op 30 oktober 1993  
te Almelo, Nederland

**Dit proefschrift is goedgekeurd door:**

*Promotor*

Prof. dr. ir. C.H. Slump

*Co-promotoren*

Dr. J.D. van Dijk, MSc, MBA

Dr. J.A. van Dalen

## **Paranimfen**

Dr. E.N.M. Lesscher

A.G. Tegelaar, BSc



# TABLE OF CONTENTS

---

<b>CHAPTER 1</b>	Introduction	9
------------------	--------------	---

---

## **PART I**

---

<b>CHAPTER 2</b>	Editorial: The next step in improving (semi-) quantitative MPI PET	27
------------------	--	----

<b>CHAPTER 3</b>	Value of SiPM PET in myocardial perfusion imaging using Rubidium-82	35
------------------	---	----

<b>CHAPTER 4</b>	Effect of temporal sampling protocols on myocardial blood flow measurements using Rubidium-82 PET	53
------------------	---	----

<b>CHAPTER 5</b>	Impact of regadenoson-induced myocardial creep on dynamic Rubidium-82 PET myocardial blood flow quantification	71
------------------	--	----

<b>CHAPTER 6</b>	How to detect and correct myocardial creep in myocardial perfusion imaging using Rubidium-82 PET	87
------------------	--	----

---

---

## PART II

---

<b>CHAPTER 7</b>	Diagnostic value of regional myocardial flow reserve measurements using Rubidium-82 PET	101
<b>CHAPTER 8</b>	Patient-tailored risk assessment of obstructive coronary artery disease using Rubidium-82 PET-based myocardial flow quantification with visual interpretation	117
<b>CHAPTER 9</b>	Machine learning based model to diagnose obstructive coronary artery disease using calcium scoring, PET imaging and clinical data	131
<b>CHAPTER 10</b>	Summary and future perspectives	151
<b>CHAPTER 11</b>	Nederlandse samenvatting en toekomstperspectieven	163
<b>APPENDICES</b>	List of abbreviations	178
	List of publications	180
	Curriculum Vitae	182
	Dankwoord	184

---



# INTRODUCTION

## **Authors**

Sabine S. Koenders<sup>1,2</sup>

## **Author Affiliations**

1. Department of Nuclear Medicine, Isala Hospital, Zwolle, the Netherlands
2. Technical Medical Centre, University of Twente, Enschede, the Netherlands

**Unpublished**

## INTRODUCTION

Cardiovascular disease was accountable for 22% of all deaths in the Netherlands in 2020<sup>1</sup>. Of these deaths, 22% were due to coronary artery disease (CAD)<sup>1</sup>. CAD is mainly caused by atherosclerosis, a process that leads to the build-up of atherosclerotic plaques in the coronary arteries<sup>2</sup>. Atherosclerosis is a progressive disease that will eventually narrow the coronary arteries (stenosis), resulting in a reduced blood flow to the heart<sup>3</sup>. During stress (exercise) the oxygen demand of the myocardium is higher as compared to during rest. If a possible stenosis results in a decreased myocardial perfusion causing an inadequate oxygen supply during stress, it is called ischemia. Early detection and accurate treatment of obstructive CAD are essential to prevent CAD from worsening and resulting in an infarction<sup>4</sup>.

### **Cardiac imaging**

In patients suspected of having obstructive CAD with an intermediate pre-test probability, non-invasive cardiac imaging is recommended<sup>4</sup>. There are two types of non-invasive CAD imaging: anatomical and functional imaging. Computed tomography (CT) based coronary artery calcium scoring (CACS) and coronary computed tomography angiography (CCTA) are used to obtain anatomical information about the coronaries. Stress echocardiography, stress cardiac magnetic resonance (CMR) imaging and perfusion imaging (MPI) using single photon emission computed tomography (SPECT) or positron emission tomography (PET) are the functional imaging modalities<sup>4</sup>. Of these modalities, stress CMR and PET MPI have the best diagnostic performance to detect obstructive CAD<sup>5</sup>. Availability and expertise eventually determine the imaging modality that is used in clinical practice. This thesis focuses on PET as imaging modality in the detection of obstructive CAD.

### **Advantages of PET myocardial perfusion imaging**

PET is well validated and can be used to visualize the perfusion in the different regions of the myocardium relative to the region with the highest tracer uptake to detect obstructive CAD<sup>6</sup>. The drawback of measuring relative myocardial perfusion is that a global reduction can remain unnoticed and that the extent of a possible stenosis may be underestimated<sup>6</sup>. To overcome these problems PET MPI offers the possibility to quantify the volume of blood per minute per gram of myocardial tissue (myocardial blood flow, MBF in mL/min/g).

To be able to detect obstructive CAD using PET, a rest and stress scan are required where stress is usually induced pharmacologically while the patient is lying inside the PET scanner<sup>7, 8</sup>. The ratio of MBF during maximal coronary vasodilatation (stress) to resting MBF constitutes the myocardial flow reserve (MFR). In other words, MFR is a measure for the extent to which the coronary circulation can increase when the heart needs to work harder. MBF and MFR quantification therefore provide additional and quantitative information about the extent and functional importance of possible stenosis in addition to the visual evaluation of myocardial perfusion images. This is important in the detection and evaluation of obstructive CAD. Moreover, MBF and MFR have also been demonstrated to provide valuable prognostic information<sup>6, 9-11</sup>.



### Data acquisition and reconstruction in cardiac perfusion PET

For quantitative PET MPI it is important that the PET scanner used is capable of dealing with the accompanying high count-rates to prevent detector saturation<sup>12,13</sup>. Inaccurate count-rate measurements can result in unreliable MBF and MFR values<sup>14</sup>. Recent developments in PET technology include PET systems using silicon photomultipliers (SiPM) with digital readout instead of conventional photomultiplier tubes (PMTs)<sup>15-18</sup>. These SiPM-based PET systems have a relatively high count-rate capability and an improved spatial and timing resolution as compared to PMT-based PET<sup>15-17, 19, 20</sup>. First oncology-PET studies showed that SiPM provides an improved image quality over PMT and therefore its use in PET MPI seems promising<sup>20-23</sup>. Studies demonstrating the clinical value of SiPM for PET MPI are therefore of interest.

There are several tracers available for PET MPI: Fluorine-18 flurpiridaz (F-18), Nitrogen-13 (N-13) ammonia, Oxygen-15 (O-15) labeled water, and Rubidium-82 (Rb-82)<sup>6</sup>. This thesis focuses on Rb-82 PET MPI. The advantage of Rb-82 over N-13 ammonia or O-15 water is that it is widely available as it requires a strontium-82/Rb-82 generator instead of a cyclotron. Moreover, Rb-82 has a short half-life (76 seconds) as compared to O-15 water (2.06 minutes), N-13 ammonia (9.96 minutes) and F-18 flurpiridaz (109 minutes)<sup>24</sup>. The short half-life means that radioactivity rapidly disappears. In this way a rest acquisition is not influenced by a preceding stress acquisition, or vice versa. With Rb-82 all data can therefore be acquired within 30 minutes<sup>25</sup>. One disadvantage of Rb-82 is that it has a rather large positron range (8.6 mm) as compared to O-15 water (4.1 mm), N-13 ammonia (2.5 mm), and F-18 flurpiridaz (1.0 mm)<sup>24</sup>. Another disadvantage is the low extraction of Rb-82 from blood to the myocardium which will be further explained in the tracer kinetic modeling paragraph<sup>6</sup>. The acquisition of PET data starts after administration of Rb-82. Despite the wide clinical use of Rb-82, the amount of activity that is used varies widely and is currently not standardized.

Cardiac perfusion PET data are usually acquired in list-mode. A list-mode acquisition results in a file containing information of all coincidences including their time stamp<sup>26</sup>. This allows to freely choose the number and duration of time frames for image reconstruction. For relative and electrocardiogram (ECG)-gated PET MPI, only the last part of the rest and stress acquisition (data acquired >2:15 minutes after Rb-82 injection) is used to reconstruct the static (see Figure 1) and gated images as the activity is then primarily present in the myocardium<sup>27</sup>. However, to be able to quantify the MBF and MFR, all data over time (dynamic) are needed from filling of the left ventricle (LV), which is called the first-pass phase, till the phase where the activity is primarily present in the myocardium, which is called the tissue phase.

For the acquisition of the stress PET data, there are three commonly used vasodilators that can be used to induce stress: adenosine, dipyridamole, and regadenoson. All three allow accurate calculation of quantitative MBF values in MPI using Rb-82 PET<sup>28-32</sup>. The disadvantages of adenosine and dipyridamole over regadenoson are that these agents induce short-term side-effects as general discomfort, chest pain, and hypotension, and more severe side-effects such as atrioventricular block or bronchospasm. Regadenoson is better tolerated by patients but is more expensive<sup>28, 29, 33-38</sup>. Another advantage of regadenoson is that it results in lower degree

of patient motion compared to adenosine, which can influence MBF quantification<sup>6, 39-42</sup>. However, a change in respiratory levels may occur when using regadenoson. This may lead to a repositioning of the heart that slowly moves back to its original position once the vasodilator stimulus is worn off. It is of interest to study the effect of correcting for this myocardial creep on MBF and MFR values.

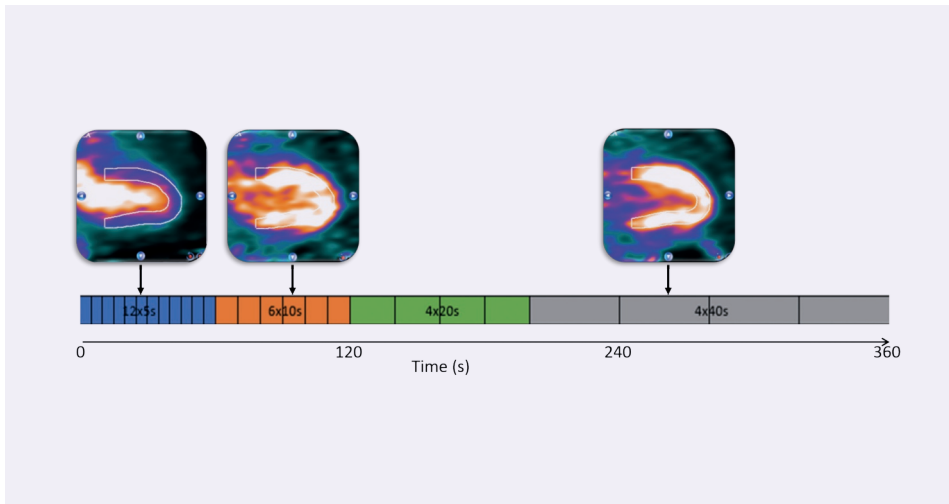
### Myocardial blood flow quantification

The acquired PET data are divided into several time frames as defined by a temporal sampling protocol to quantify MBF. For every time frame, an image is reconstructed, as illustrated in Figure 2. To calculate the MBF for the whole myocardium or for a specific region, the activity concentration in the corresponding myocardial area and the LV (blood pool) is measured in each of the reconstructed images using regions of interest (ROIs) methodology. This is done for both the dynamic rest and stress data. A myocardium contour is drawn in a reconstructed image using the data acquired during the tissue phase. Next, ROIs of the myocardium and LV are copied to all the reconstructed images. Subsequently time activity curves (TACs), as shown in Figure 3, can be calculated for each ROI<sup>43</sup>. The TACs are usually calculated for three vascular territories, the left anterior descending (LAD), left circumflex (LCX), and right coronary artery (RCA), and for the myocardium as a whole (global).

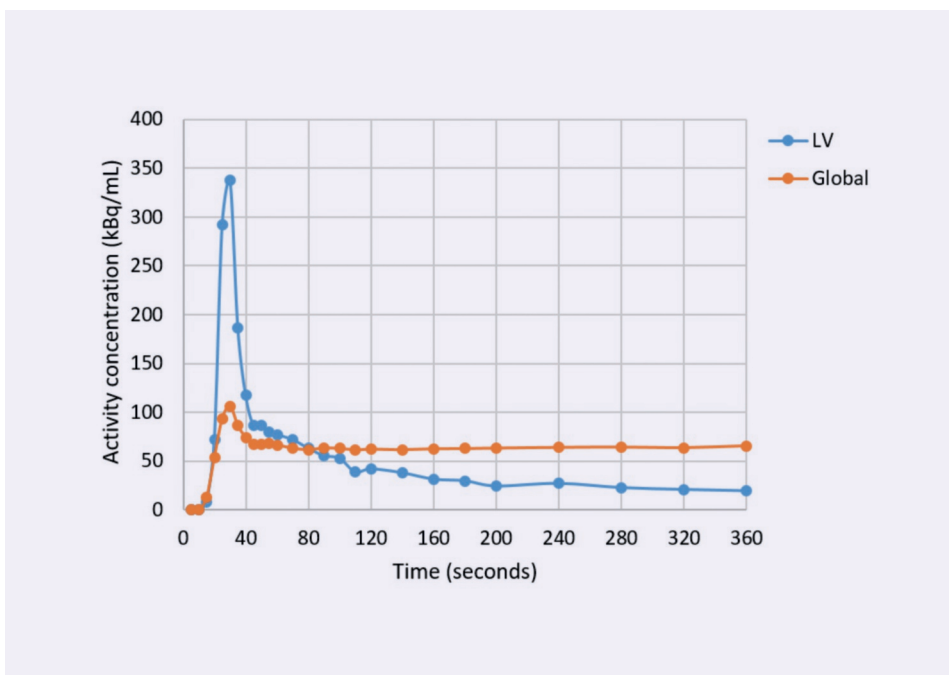
It is important that the measurements resulting in the TACs are accurate as they are used as input for compartmental analysis to calculate the MBF, which will be further explained in the next section<sup>6, 43, 44</sup>. Both the length and the number of time frames in the temporal sampling protocol may influence the measured TACs and may therefore alter MBF and MFR measurements<sup>45</sup>. There is a variety of temporal sampling protocols being used clinically to measure MBF. It is therefore interesting to assess the effect of different temporal sampling protocols on MBF and MFR quantification in Rb-82 PET.



Figure 1. Relative Rb-82 PET perfusion images showing a decreased uptake in the anteroseptal wall during stress compared to rest indicating ischemia (arrow). From left to right: short axis view, horizontal long axis view and vertical long axis view.



**Figure 2.** Illustration of a temporal sampling protocol based on 26 time-frames (12x5s, 6x10s, 4x20s and 4x40s). For each of the time frames, an image is reconstructed. Three phases can be distinguished: the first pass phase i.e. filling of the left ventricle (LV), the intermediate phase (activity in both the LV and myocardium) and the tissue phase (activity in myocardium).



**Figure 3.** Time activity curves (TACs) showing the first pass phase where there is a peak for the left ventricle (LV) followed by the tissue phase where a steady state is reached for the whole myocardium (global).

### Tracer kinetic modelling

The PET-based time activity curves (TACs) of the LV,  $C_{LV}(t)$  and the myocardium,  $C_{PET}(t)$ , are used as input function for a tracer kinetic model that quantifies the MBF. Such a model describes the uptake and wash-out of a tracer from the blood to the myocardium and vice versa, as illustrated in Figure 4<sup>46-49</sup>. The true activity concentration at a specified time in the myocardium ( $C_m(t)$ ) primarily depends on two factors: the MBF from the blood to the myocardium and secondly, the tracer activity concentration in the LV ( $C_{LV}(t)$ )<sup>47</sup>. The tracer uptake rate from the LV to the myocardium is related to the MBF and is defined as  $K_1$ . The wash-out of the tracer from the tissue back into the LV blood pool is defined as  $k_2$ . The one-tissue compartment model of Lortie et al. is mostly used for Rb-82 PET to describe this dynamic exchange of the tracer to quantify the MBF<sup>50</sup>.

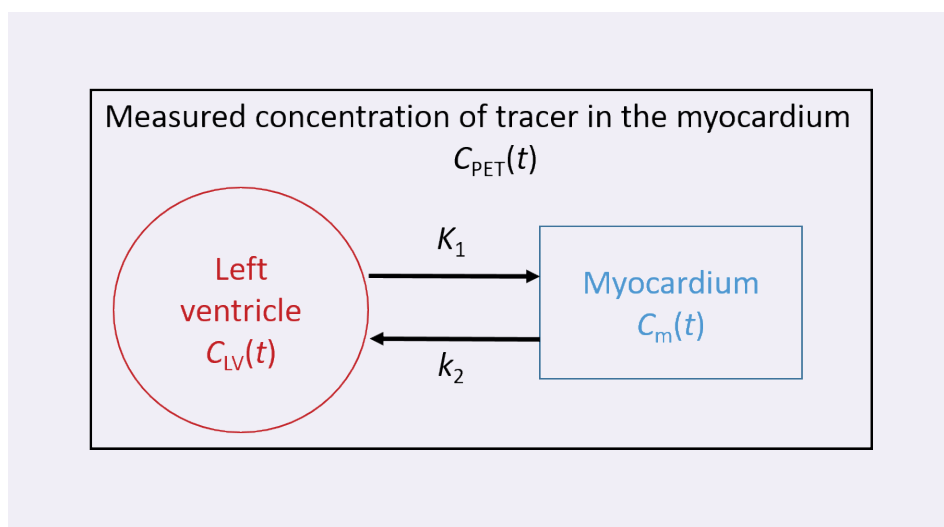


Figure 4. Compartment model of the myocardium showing transport of tracer between the left ventricle (LV) “blood pool” and tissue adapted from Klein et al.<sup>43</sup>  $C_{LV}(t)$  is the activity concentration over time in the LV.  $C_m(t)$  is the activity concentration over time in the myocardium and  $C_{PET}(t)$  the measured activity concentration in the myocardium based on e.g. ROIs methodology on PET images. Due to the limited spatial resolution of PET, spillover effects are introduced. Therefore,  $C_{PET}(t)$  consists of contributions from both  $C_{LV}(t)$  and  $C_m(t)$ .  $K_1$  is the tracer uptake rate from the left ventricle to the myocardium,  $k_2$  is the wash-out of tracer from the myocardium back into the left ventricle.

Mathematically, this model can be described by differential equation 1:

$$\frac{dC_m(t)}{dt} = K_1 C_{LV}(t) - k_2 C_m(t) \quad (1)$$

where  $C_m(t)$  is in kBq/g,  $K_1$  in mL/min/g and  $C_{LV}(t)$  is in kBq/mL. The general solution of the differential equation can then be written as a convolution integral as in equation 2:

$$C_m(t) = K_1 e^{-k_2 t} \otimes C_{LV}(t) \quad (2)$$

Due to the limited spatial resolution of PET of typically 9-12 mm, partial volume and spillover effects are introduced. Partial volume effects are the loss of apparent activity in small regions or on edges (myocardial wall) resulting in an underestimation of the tracer activity<sup>51, 52</sup>. The spillover effect is an increase of apparent activity in small regions or on edges that have much lower uptake than their surrounding tissue. Consequently, the PET-based measured activity concentration in the myocardium  $C_{PET}(t)$  is not equal to the true activity concentration in the myocardium  $C_m(t)$ . Because of partial volume and spillover effects, two correction factors are applied to equation (2). First, a regional estimate of the myocardial partial volume recovery coefficient (RC, ratio of apparent activity concentration to true activity concentration)<sup>43, 51</sup>. Second, the fractional blood volume (*FBV*) representing the ROI's signal associated with the LV blood pool<sup>43</sup>. It is assumed that the LV TAC,  $C_{LV}(t)$ , is free of partial volume effects and that the measured tracer concentration in the myocardium PET,  $C_{PET}(t)$ , consists of contributions from the LV ( $C_{LV}(t)$ ) and myocardium tissue  $C_m(t)$ , due to the spillover effect<sup>46</sup>.

It is assumed that the ROI's total signal recovery consists only of LV blood pool or myocardium signal<sup>43</sup>. Therefore, *RC* equals to  $1-FBV$  resulting in the 1-tissue compartment model of Lortie et al., described by equation 3<sup>50</sup>:

$$C_{PET}(t) = FBV C_{LV}(t) + (1 - FBV)K_1 e^{-k_2 t} \otimes C_{LV}(t) \quad (3)$$

Measurements of  $C_{LV}(t)$ ,  $C_{PET}(t)$  and the model allow us to estimate the model parameters  $K_1$ ,  $k_2$  and  $FBV$ <sup>47</sup>. The least-squares estimation is used to find the rate constants that provide the best fit to the myocardium measurements<sup>47</sup>. Next,  $K_1$  can be converted to MBF using the extraction fraction correction as Rb-82 does not accumulate in the myocardium linearly proportional to perfusion, as shown in Figure 5. The extraction function (4) corrects  $K_1$  to estimate the MBF:

$$K_1 = EF \times MBF = (1 - a e^{-b/MBF}) MBF \quad (4)$$

where the values for *a* and *b* were experimentally determined by Lortie et al. to be 0.77 and 0.63, respectively<sup>50</sup>.



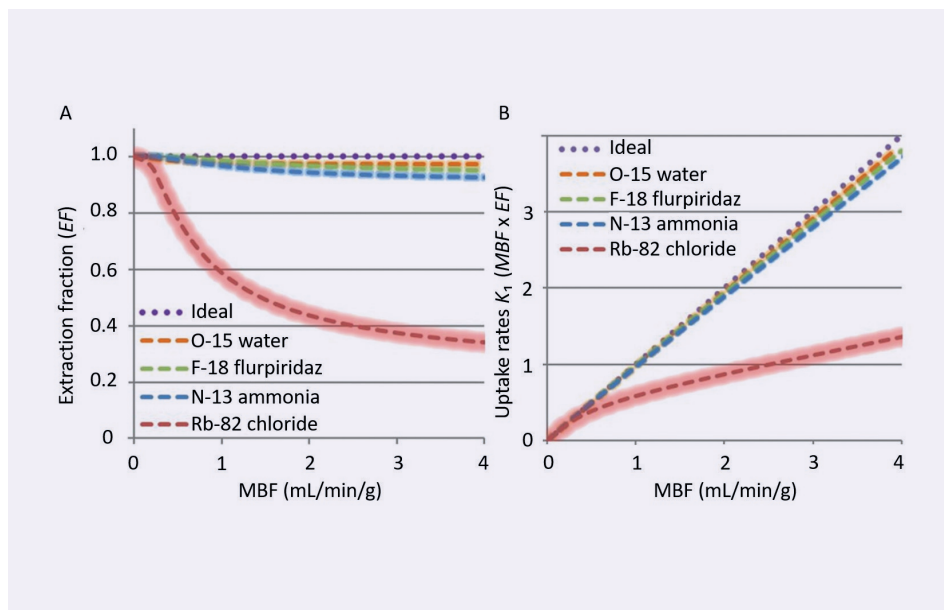


Figure 5. Tracer extraction fractions (A) and uptake rates (B) adapted from Murthy et al.<sup>6</sup>. The purple line shows the ideal situation where  $K_1 = MBF$ . As Rb-82 does not accumulate in the myocardium linearly proportional to  $MBF$ ,  $K_1$  should be converted to  $MBF$  using the extraction fraction correction:  $K_1 = EF \times MBF = (1 - ae^{-b/MBF}) \times MBF$ . The values for  $a$  and  $b$  were experimentally determined by Lortie et al. to be 0.77 and 0.63, respectively<sup>22</sup>.

### Optimization of myocardial blood flow quantification

Implementation of  $MBF$  and  $MFR$  quantification is not straightforward as there are several pitfalls in the process of data acquisition, image reconstruction, post-processing and interpretation of quantitative myocardial PET perfusion that can result in unreliable  $MBF$  and  $MFR$  values<sup>44</sup>. Although the knowledge about these technical difficulties increases, there are still questions to solve, as mentioned in the sections above. In order for  $MBF$  and  $MFR$  quantification to achieve its full clinical potential, the technical aspects of  $MBF$  and  $MFR$  quantification must be well understood and standardized so that reliable  $MBF$  and  $MFR$  values can be routinely produced<sup>44</sup>.

## THESIS OUTLINE

Therefore, the aim of this thesis was to study and optimize technical aspects to obtain reliable MBF and MFR values with Rb-82 PET MPI. Furthermore, we studied the clinical value of MFR. This thesis is therefore divided into two parts.

### **PART I – Optimizing MBF quantification**

Part I of this thesis consists of five chapters in which we determined how different steps in the process from data acquisition to image reconstruction and processing can affect quantitative myocardial PET perfusion. Accordingly, we described how to deal with these aspects to obtain reliable MBF and MFR values.

The first step in performing MPI with PET is the data acquisition which requires the administration of Rb-82 activity. **Chapter 2** contains an editorial with our view on the study performed by Hoff et al. in which their focus was to describe the effect of the injected Rb-82 activity on MBF quantification<sup>53</sup>. They compared the effect of different administered activities (1110 versus either 740 or 370 MBq) on relative perfusion images and MBF and MFR values. The study by Hoff et al. has extended our current knowledge on the technical pitfalls in MBF and MFR quantification using PET and contributes to the integration of flow quantification in clinical practice.

There are different types of PET scanners available for MBF quantification with Rb-82 PET. Recent developments in PET technology include PET systems using SiPM with digital readout instead of PMT<sup>15, 16, 18</sup>. However, studies demonstrating the value of SiPM PET for MPI are still lacking. In **Chapter 3** we determined the value of a SiPM-based PET in MPI as compared to a PMT-based PET. We performed a prospective study in 30 patients who underwent MPI on both PET systems within 3 weeks. We compared image quality, defect interpretation, interpreter's confidence, MBF, and MFR values between both systems.

After acquiring the data, the PET images are reconstructed and processed. A temporal sampling protocol is used to reconstruct the dynamic images which are used in a kinetic model for MBF and MFR quantification. To interchange and interpret MBF and MFR values across different centers, it is important to know the effect of temporal sampling on MBF and MFR values. In **Chapter 4** we determined the effect of different temporal sampling protocols on MBF and MFR quantification. PET images of 20 patients were reconstructed using 14 different temporal sampling protocols. MBF and MFR values were calculated for all protocols and compared to a reference protocol with 26 frames.

Myocardial motion can influence TACs of the LV and myocardium, in particular when using ROIs methodology, thereby affecting blood flow measurements<sup>6, 39-42</sup>. In particular motion can be expected during stress imaging when using regadenoson. This vasodilator may cause a change in respiratory levels, thereby a repositioning of the heart (myocardial creep) that gradually moves back to its original position once the regadenoson stimulus is terminated. In **Chapter 5** we determined the effect of correcting for

this myocardial creep on MBF and MFR values. We retrospectively included 119 patients and visually assessed the presence of myocardial creep. Next, we compared uncorrected and corrected MBF and MFR values for the three vascular territories (LAD, LCX, and RCA) and for the myocardium as a whole. In **Chapter 6** we provided instructions on how to detect and correct for myocardial creep for better integration of flow quantification in clinical practice.

## **PART II – Clinical value of MBF quantification**

This part covers the clinical value of MBF and MFR quantification using Rb-82 PET. As small regional blood flow deficits may go unnoticed when only assessing *global* blood flow values, it is of interest to study the value of *regional* blood flow. We compared the diagnostic value of regional MFR to global MFR in **Chapter 7**, to achieve the full potential of MFR values. We retrospectively included 1519 patients without prior history of CAD referred for rest and regadenoson-induced stress Rb-82 PET/CT. Receiver operating characteristic (ROC) analyses were conducted to evaluate and compare the diagnostic value of global and regional MFR. The primary endpoint was a diagnosis of obstructive CAD on invasive coronary angiography (ICA).

In assessing patient's risk of oCAD it is unclear how MFR should be combined with visual assessment, especially when they are discordant. In **Chapter 8** we determined the probability of obstructive CAD based on visual assessment of Rb-82 PET scans and MFR values. We retrospectively included 1519 patients without a prior history of CAD referred for rest and regadenoson-induced stress Rb-82 PET/CT. Next, the probability of obstructive CAD for both visually normal and abnormal Rb-82 PET scans was determined as a function of MFR. The primary endpoint was obstructive CAD on ICA.

After non-invasive imaging, cardiologists combine the imaging data, clinical data and type of complaints to estimate a post-test likelihood and, if needed, determine a specific treatment strategy. However, the human ability to interpret and integrate all available data into one post-test likelihood of obstructive CAD is limited. In **Chapter 9** we aimed to develop and validate a machine learning (ML)-based model to diagnose obstructive CAD using the available data. In addition, we compared the diagnostic performance of this ML-model to that of expert physicians. We retrospectively included a consecutive cohort of 1007 patients with no prior history of obstructive CAD. ROC analysis was conducted for the ML-model and we compared the accuracy, sensitivity, and specificity achieved by expert physicians to that of the ML-model.

In **Chapter 10** a summary of the key findings is provided and future perspectives are discussed. In **Chapter 11** a Dutch summary is provided.

## REFERENCES

1. Y. Koop, R.H. Wimmers, I. Vaartjes, M.L. Bots. Hart- en vaatziekten in nederland 2021, Cijfers over incidentie, prevalentie, ziekte en sterfte. 2021.
2. Buja LM. Coronary Artery Disease. Springer London; 2015. p. 1-20.
3. Shah P, Bajaj S, Virk H, Bikkina M, Shamoon F. Rapid progression of coronary atherosclerosis: A review. *Thrombosis*. 2015.
4. Montalescot G, Sechtem U, Achenbach S, Andreotti F, Arden C, Budaj A, et al. 2013 ESC guidelines on the management of stable coronary artery disease: The task force on the management of stable coronary artery disease of the european society of cardiology. *Eur Heart J*. 2013;34:2949-3003.
5. Knuuti J, Ballo H, Juarez-Orozco LE, Saraste A, Kolh P, Rutjes AWS, et al. The performance of non-invasive tests to rule-in and rule-out significant coronary artery stenosis in patients with stable angina: A meta-analysis focused on post-test disease probability. *Eur Heart J*. 2018;39:3322-30.
6. Murthy V, Bateman T, Beanlands R, Berman D, Borges-Neto S, Chareonthaitawee P, et al. Clinical quantification of myocardial blood flow using PET: Joint position paper of the SNMMI cardiovascular council and the ASNC. *J Nucl Cardiol*. 2018;25:269-97.
7. Machac J. Cardiac PET and PET/CT Imaging. Springer; 2007. p. 73-82.
8. Saraste A, Kajander S, Han C, Nesterov SV, Knuuti J. PET: Is myocardial flow quantification a clinical reality? *J Nucl Cardiol*. 2012;19:1044-59.
9. Ziadi MC, deKemp RA, Williams KA, Guo A, Chow BJ, Renaud JM, et al. Impaired myocardial flow reserve on rubidium-82 positron emission tomography imaging predicts adverse outcomes in patients assessed for myocardial ischemia: Cardiac imaging. 2011;58:740-8.
10. Sciagra R, Passeri A, Bucerus J, Verberne HJ, Slart, Riemer H. J. A., Lindner O, et al. Clinical use of quantitative cardiac perfusion PET: Rationale, modalities and possible indications. position paper of the cardiovascular committee of the european association of nuclear medicine (EANM). *Eur J Nucl Med Mol Imaging*. 2016;43:1530-45.
11. Murthy VL, Naya M, Foster CR, Hainer J, Gaber M, Di Carli G, et al. Improved cardiac risk assessment with noninvasive measures of coronary flow reserve. *Circulation*. 2011;124:2215-24.
12. van Dijk J, Jager P, van Osch J, Khodaverdi M, van Dalen J. Comparison of maximal rubidium-82 activities for myocardial blood flow quantification between digital and conventional PET systems. *J Nucl Cardiol*. 2019;26:1286-91.
13. Renaud JM, Yip K, Guimond J, Trottier M, Pibarot P, Turcotte E, et al. Characterization of 3-dimensional PET systems for accurate quantification of myocardial blood flow. *J Nucl Med*. 2017;58:103-9.
14. DeKemp RA, Yoshinaga K, Beanlands RSB. Will 3-dimensional PET-CT enable the routine quantification of myocardial blood flow? *J Nucl Cardiol*. 2007;14:380-97.
15. Slomka PJ, Pan T, Germano G. Recent advances and future progress in PET instrumentation. *Semin Nucl Med*. 2016;46:5-19.
16. Miller M, Zhang J, Binzel K, Griesmer J, Laurence T, Narayanan M, et al. Characterization of the vereos digital photon counting PET system. *J Nucl Med*. 2015;56(supplement 3):434.

17. van Sluis JJ, de Jong J, Schaar J, Noordzij W, van Snick P, Dierckx R, et al. Performance characteristics of the digital biograph vision PET/CT system. *J Nucl Med.* 2019;60:1031-6.
18. Hsu DFC, Ilan E, Peterson WT, Uribe J, Lubberink M, Levin CS. Studies of a next-generation silicon-Photomultiplier–Based time-of-flight PET/CT system. *J Nucl Med.* 2017;58:1511-8.
19. Slomka PJ, Pan T, Berman DS, Germano G. Advances in SPECT and PET hardware. *Prog Cardiovasc Dis.* 2015;57:566-78.
20. Van der Vos CS, Koopman D, Rijnsdorp S, Arends AJ, Boellaard R, van Dalen JA, et al. Quantification, improvement, and harmonization of small lesion detection with state-of-the-art PET. *Eur J Nucl Med Mol Imaging.* 2017;44:4-16.
21. López-Mora DA, Flotats A, Fuentes-Ocampo F, Camacho V, Fernández A, Ruiz A, et al. Comparison of image quality and lesion detection between digital and analog PET/CT. *Eur J Nucl Med Mol Imaging.* 2019;46:1383-90.
22. van Sluis J, Boellaard R, Somasundaram A, van Snick P, Borra R, Dierckx R, et al. Image quality and semi-quantitative measurements of the siemens biograph vision PET/CT: Initial experiences and comparison with siemens biograph mCT PET/CT. *J Nucl Med.* 2020;61:129-35.
23. Nguyen NC, Vercher-Conejero JL, Sattar A, Miller MA, Maniawski PJ, Jordan DW, et al. Image quality and diagnostic performance of a digital PET prototype in patients with oncologic diseases: Initial experience and comparison with analog PET. *J Nucl Med.* 2015;56:1378-85.
24. Maddahi J, Packard RRS. Cardiac PET perfusion tracers: Current status and future directions. *Semin Nucl Med.* 2014;44:333-43.
25. Nakazato R, Berman DS, Alexanderson E, Slomka P. Myocardial perfusion imaging with PET. 2013;5:35-46.
26. Cherry SR, Sorenson JA, Phelps ME. *Physics in Nuclear Medicine (Fourth Edition).* W.B. Saunders; 2012. p. 307-43.
27. van Dijk JD, Huizing ED, van Dalen JA, Timmer JR, Jager PL. Minimal starting time of data reconstruction for qualitative myocardial perfusion rubidium-82 positron emission tomography imaging. 2018;39:533-8.
28. Iskandrian AE, Bateman TM, Belardinelli L, Blackburn B, Cerqueira MD, Hendel RC, et al. Adenosine versus regadenoson comparative evaluation in myocardial perfusion imaging: Results of the ADVANCE phase 3 multicenter international trial. *J Nucl Cardiol.* 2007;14:645-58.
29. Cerqueira MD, Nguyen P, Staehr P, Underwood SR, Iskandrian AE. Effects of age, gender, obesity, and diabetes on the efficacy and safety of the selective A2A agonist regadenoson versus adenosine in myocardial perfusion imaging. 2008;1:307.
30. Cullom SJ, Case JA, Courter SA, McGhie AI, Bateman TM. Regadenoson pharmacologic rubidium-82 PET: A comparison of quantitative perfusion and function to dipyridamole. *J Nucl Cardiol.* 2013;20:76-83.
31. Hsiao E, Ali B, Blankstein R, Skali H, Ali T, Bruyere J, John, et al. Detection of obstructive coronary artery disease using regadenoson stress and 82Rb PET/CT myocardial perfusion imaging. 2013;54:1748-54.



32. Goudarzi B, Fukushima K, Bravo P, Merrill J, Bengel FM. Comparison of the myocardial blood flow response to regadenoson and dipyridamole: A quantitative analysis in patients referred for clinical  $^{82}\text{Rb}$  myocardial perfusion PET. *Eur J Nucl Med Mol Imaging*. 2011;38:1908-16.
33. Jager PL, Buiting M, Mouden M, Oostdijk AHJ, Timmer J, Knollema S. Regadenoson as a new stress agent in myocardial perfusion imaging. Initial experience in The Netherlands. *Revista espanola de medicina nuclear e imagen molecular*. 2014 Nov;33(6):346.
34. Sara G Johnson, Scott Peters. Advances in pharmacologic stress agents: Focus on regadenoson. *J Nucl Med Technol*. 2010;38:163-71.
35. Luiz Belardinelli, John C. Shryock, Stephen Snowdy, Yi Zhang, Angela Monopoli, Gianluca Lozza, et al. The A<sub>2A</sub> adenosine receptor mediates coronary vasodilation. 1998;284:1066.
36. Hendel RC, Bateman TM, Cerqueira MD, Iskandrian AE, Leppo JA, Blackburn B, et al. Initial clinical experience with regadenoson, a novel selective A<sub>2A</sub> agonist for pharmacologic stress single-photon emission computed tomography myocardial perfusion imaging. *J Am Coll Cardiol*. 2005;46:2069.
37. Cerqueira MD, Verani MS, Schwaiger M, Heo J, Iskandrian AS. Safety profile of adenosine stress perfusion imaging: Results from the adenoscan multicenter trial registry. *J Am Coll Cardiol*. 1994;23:384-9.
38. Ranhosky A, Kempthorne-Rawson J. The safety of intravenous dipyridamole thallium myocardial perfusion imaging. intravenous dipyridamole thallium imaging study group. 1990;81:1205-9.
39. Memmott M, Tonge C, Saint K, Arumugam P. Impact of pharmacological stress agent on patient motion during rubidium-82 myocardial perfusion PET/CT. *J Nucl Cardiol*. 2018;25:1286-95.
40. Hunter, Chad R. R. N., Klein R, Beanlands RS, DeKemp RA. Patient motion effects on the quantification of regional myocardial blood flow with dynamic PET imaging. 2016;43:1829-40.
41. Koshino K, Watabe H, Enmi J, Hirano Y, Zeniya T, Hasegawa S, et al. Effects of patient movement on measurements of myocardial blood flow and viability in resting  $^{15}\text{O}$ -water PET studies. *J Nucl Cardiol*. 2012;19:524-33.
42. Piccinelli M, Votaw JR, Garcia EV. Motion correction and its impact on absolute myocardial blood flow measures with PET. *Curr Cardiol Rep*. 2018;20:1-8.
43. Klein R, Beanlands R, deKemp R. Quantification of myocardial blood flow and flow reserve: Technical aspects. *J Nucl Cardiol*. 2010;17:555-70.
44. Moody J, Lee B, Corbett J, Ficaro E, Murthy V. Precision and accuracy of clinical quantification of myocardial blood flow by dynamic PET: A technical perspective. *J Nucl Cardiol*. 2015;22:935-51.
45. Lee B, Moody J, Weinberg R, Corbett J, Ficaro E, Murthy V. Optimization of temporal sampling for  $^{82}\text{Rb}$  rubidium PET myocardial blood flow quantification. *J Nucl Cardiol*. 2017;24:1517-29.
46. Klein R. Initial steps to tracer kinetic modeling and MBF quantification. *Ann Nucl Cardiol*; 2018;4:68-73.
47. Carson RE. *Positron Emission Tomography: Basic Sciences*. Springer London; 2005. p. 127-59.
48. Anderson DH. *Compartmental modeling and tracer kinetics*. : Springer Science & Business Media; 2013.
49. Robertson JS. *Compartmental distribution of radiotracers*. Milton: CRC Press; 1983.

50. Lortie M, Beanlands R, Yoshinaga K, Klein R, DaSilva J, deKemp R. Quantification of myocardial blood flow with  $^{82}\text{Rb}$  dynamic PET imaging. *Eur J Nucl Med Mol Imaging*. 2007;34:1765-74.
51. Cherry SR, Sorenson JA, Phelps ME. *Physics in Nuclear Medicine (Fourth Edition)*. W.B. Saunders; 2012. p. 279-306.
52. Hutchins GD, Caraher JM, Raylman RR. A region of interest strategy for minimizing resolution distortions in quantitative myocardial PET studies. 1992;33:1243-50.
53. Hoff CM, Sørensen J, Christensen NL, Bouchelouche K, Tolbod L. Activity regimes for  $^{82}\text{Rb}$  cardiac PET: Effects on absolute MBF and MPI. *J Nucl Cardiol*. 2020;Epub ahead of print doi:10.1007/s12350-020-02266-2.





The background of the page is a solid orange color with a white wireframe grid pattern. The grid is composed of irregular polygons of various sizes, creating a mesh-like appearance. Scattered throughout this grid are several numerical values in a light orange or white color. These values include 1.4, 2.7, 2.9, 2, 2.9, 2.9, 1, and 2.9. The numbers are positioned at various points within the grid, some appearing to be associated with specific nodes or areas of the mesh.

**PART I**

# **OPTIMIZING MBF QUANTIFICATION**



**EDITORIAL:**

# **THE NEXT STEP IN IMPROVING (SEMI-) QUANTITATIVE MPI PET**

## **Authors**

S. S. Koenders<sup>1,2</sup>

J. A. van Dalen<sup>3</sup>

J. D. van Dijk<sup>1</sup>

## **Author Affiliations**

1. Department of Nuclear Medicine, Isala Hospital, Zwolle, the Netherlands
2. Technical Medical Centre, University of Twente, Enschede, the Netherlands
3. Department of Medical Physics, Isala Hospital, Zwolle, the Netherlands

## **Published in**

Journal of Nuclear Cardiology 2020; Epub ahead of print

## BACKGROUND

Myocardial blood flow (MBF) quantification with PET results in an improved risk assessment of coronary artery disease (CAD) in addition to semi-quantitative myocardial perfusion imaging<sup>1</sup>. A decrease in the myocardial flow reserve (MFR, MBF in stress/MBF in rest) or an increasing area of perfusion deficits results in a higher risk on cardiac mortality, as shown in Figure 1. To be able to quantify MBF, tracer uptake in the left ventricle and the myocardium during the scan has to be calculated from the imaging data. However, in the process of data acquisition, reconstruction, post-processing and interpretation of the data, there are several pitfalls that one should be aware of as these pitfalls can result in unreliable uptake calculations and hence MBF measurements<sup>2</sup>.

Multiple pitfalls for MBF quantification and corresponding solutions have been identified in the last decade. First, it is important that the PET scanner has a sufficient count-rate capability to prevent detector saturation during the first-pass phase which can lead to artificially high MBF values<sup>3,4</sup>. Secondly, to increase the reproducibility of MBF measurements, a constant activity infusion profile is required<sup>5</sup>. Yet not all Strontium-82/Rubidium-82 generators are able to produce such a constant activity bolus. Third, misregistration of PET with CT data that is used for attenuation correction can result in altered MBF measurements<sup>6</sup>. Fourth, reconstruction settings and post-processing software packages can result in a MBF bias as well<sup>7,8</sup>. Although the reproducibility is often unaffected when changing reconstruction settings or shifting to different software, a bias may occur. Fifth, patient motion and repositioning of the heart after administration of a stress agent can also negatively affect the reliability of MBF measurements<sup>9,10</sup>. However, this influence can be limited by correcting the dynamic time-frames for possible motion and “myocardial creep”<sup>11</sup>. Last, the test-retest reliability of MBF quantification is relatively large with a typical uncertainty of 21%<sup>12</sup>. This implies that there is a large ‘grey area’ in distinguishing reduced and normal MBF values and physicians should be aware of this during interpretation.

Although our knowledge of and solutions to pitfalls increases, several issues remain. For example, how to prevent scans in which there is not a well-defined activity bolus? Or how to correct for a delayed myocardial activity uptake in patients with coronary artery bypass grafts which may hamper MBF quantification. Or how to deal with MBF measurements that are based on different administered activities?

In this issue of the *Journal of Nuclear Cardiology*, Hoff et al.<sup>13</sup> addressed the latter issue by studying the effect of the injected Rubidium-82 activity on the MBF measurements and the relative myocardial perfusion images. They scanned forty patients twice using the lowest tracer activity of 1110 MBq as recommended in the prescribing information versus either 740 MBq or 370 MBq. Next, they compared the quantitative outcomes by comparing the MBF and MFR measurements and relative outcomes by comparing the ejection fraction (EF) and the semi-quantitative parameter total perfusion deficit (TPD).



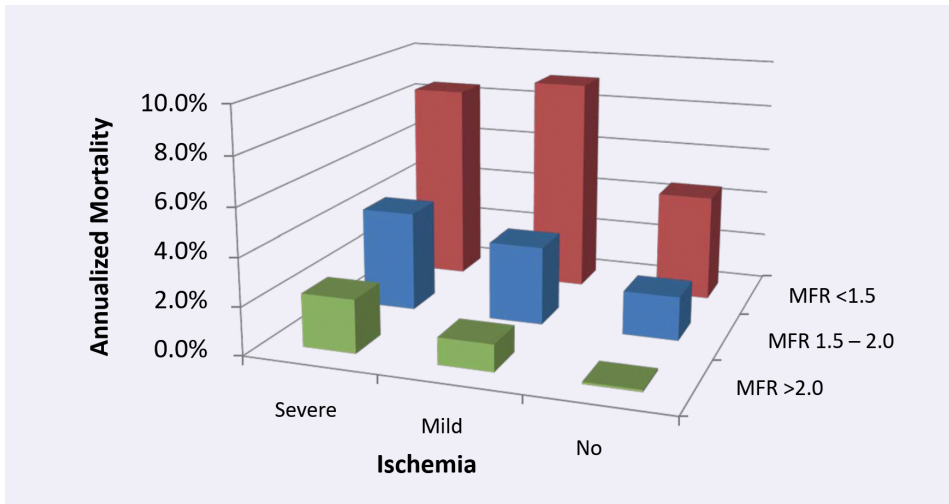


Figure 1. Annualized mortality by myocardial flow reserve (MFR) and severity of ischemia adapted from Murthy et al.<sup>1</sup> based on PET MPI examinations of 2783 patients and a median follow-up of 1.4 years (IQR: 0.7-3.2 years). With increasing ischemia and decreasing MFR, the annualized mortality increases.

Hoff et al. reported that peak count rate per injected activity decreased and peak dead time correction factors increased due to detector saturation in the first-pass phase. Reducing the activity from 1100 MBq to 740 and further to 370 MBq led to a bias and decreasing correlations for TPD and EF. This can be explained by the decreasing count statistics in the late tissue phase when lowering the administered activity. Acceptable image quality for visual interpretation was still obtained when using 740 MBq but the images became too noisy when using 370 MBq.

Although the authors showed that a lower tracer activity affects the image quality, MBF quantification was only marginally different. The global and regional MBF measurements correlated well for both activities (370 MBq and 740 MBq) with 1110 MBq ( $R^2 > 0.97$ ). Good correlations ( $R^2 = 0.96$ ) were also found for global MFR regarding both activities (370 MBq and 740 MBq) to 1110 MBq and no bias was observed. An injected activity of 740 MBq resulted in a small positive bias in global and regional (RCA and LCX) MBF values as compared to 1110 MBq. Using 370 MBq resulted in a small negative MBF bias on a global level and specifically in the LAD territory, as compared to 1110 MBq. To summarize, it seems that the low tracer activity of 740 MBq is sufficient for both semi-quantitative and quantitative MPI while the injected tracer activity of 370 MBq only provided acceptable quantitative MPI as compared to 1110 MBq.

Two comments can be made considering the results obtained by Hoff et al.<sup>13</sup> First, they reported a lower mean peak dead time factor for conventional PET using photomultiplier tubes (PMT) than for new generation PET using solid-state photodetectors at a comparable activity. This suggests that the

optimal activity regime for the new generation PET scanners is lower than for conventional PET scanners using PMT. This is remarkable as other studies show better count-rate capability for PET scanners based on solid-state photodetectors as compared to PMT PET<sup>3, 4</sup>. Secondly, it is questionable if lowering the activity to 740 MBq, as suggested by Hoff et al., can be generalized to previous generation PMT PET scanners as they often have low count-rate capabilities<sup>3, 4</sup>.

Hoff et al. showed that both MBF and MFR measurements correlated well between the reduced administered Rb-82 activity (740 MBq) and the recommended Rb-82 activity (1100 MBq). However, where MFR resulted in no bias but large limits of agreement, biases were observed for MBF with smaller limits of agreement. This raises an important question: should we use stress MBF or MFR, or perhaps both, in clinical practice? Literature still shows conflicting answers regarding this question. Some suggest that stress MBF is the preferred parameter<sup>14</sup> while others propose MFR as the parameter to use<sup>15, 16</sup>. In addition, Gould et al.<sup>17</sup> suggest a method that integrates the stress MBF and MFR into a parameter called coronary flow capacity. However, the clinical value of this parameter over MFR or stress MBF has yet to be determined. Furthermore, MBF and MFR measurements are often only assessed on a global or vascular level whereas visual images are assessed on smaller regional levels. Hence, it is still unknown whether we should use MBF, MFR or coronary flow capacity and whether we should do this on a global, vascular or regional level to obtain the best prognostic information.

Altogether, the study of Hoff et al. clearly shows that the amount of tracer activity to be administered should be chosen with care for MBF and MFR measurements using PET. Therefore, each center that wants to start with MBF quantification should determine the activity that results in sufficient count statistics for relative perfusion imaging or semi-quantitative imaging but does not lead to detector saturation during the first-pass phase for MBF or MFR quantification. The study by Hoff et al.<sup>13</sup> has extended our current knowledge on the (technical) pitfalls in MBF and MFR quantification using PET. This greatly contributes to integration of flow quantification in clinical practice. Solving the remaining issues will likely result in even more reliable blood flow measurements and thus a further improvement in the diagnostic accuracy and prognostic value of PET MPI in the near future.

## REFERENCES

1. Murthy VL, Naya M, Foster CR, Hainer J, Gaber M, Di Carli G, et al. Improved cardiac risk assessment with noninvasive measures of coronary flow reserve. *Circulation*. 2011;124:2215-24.
2. van Dijk JD, Jager PL, van Dalen JA. Pitfalls in myocardial blood flow quantification with rubidium-82 PET. *Tijdschr voor Nucl Geneesk*. 2017;39:1822-9.
3. Renaud JM, Yip K, Guimond J, Trottier M, Pibarot P, Turcotte E, et al. Characterization of 3-dimensional PET systems for accurate quantification of myocardial blood flow. *J Nucl Med*. 2017;58:103-9.
4. van Dijk J, Jager P, van Osch J, Khodaverdi M, van Dalen J. Comparison of maximal rubidium-82 activities for myocardial blood flow quantification between digital and conventional PET systems. *J Nucl Cardiol*. 2019;26:1286-91.
5. Klein R, Ocneanu A, Renaud J, Ziadi M, Beanlands R, deKemp R. Consistent tracer administration profile improves test-retest repeatability of myocardial blood flow quantification with 82Rb dynamic PET imaging. *J Nucl Cardiol*. 2018;25:929-41.
6. Rajaram M, Tahari AK, Lee AH, Lodge MA, Tsui B, Nekolla S, et al. Cardiac PET/CT misregistration causes significant changes in estimated myocardial blood flow. *J Nucl Med*. 2013;54:50-4.
7. Tahari AK, Lee A, Rajaram M, Fukushima K, Lodge MA, Lee BC, et al. Absolute myocardial flow quantification with (82)rb PET/CT: Comparison of different software packages and methods. *Eur J Nucl Med Mol Imaging*. 2014;41:126-35.
8. Armstrong I, Tonge C, Arumugam P. Impact of point spread function modeling and time-of-flight on myocardial blood flow and myocardial flow reserve measurements for rubidium-82 cardiac PET. *J Nucl Cardiol*. 2014;21:467-74.
9. Koenders SS, van Dijk JD, Jager PL, Ottervanger JP, Slump CH, van Dalen JA. Impact of regadenoson-induced myocardial creep on dynamic rubidium-82 PET myocardial blood flow quantification. *J Nucl Cardiol*. 2019;26:719-28.
10. Memmott M, Tonge C, Saint K, Arumugam P. Impact of pharmacological stress agent on patient motion during rubidium-82 myocardial perfusion PET/CT. *J Nucl Cardiol*. 2018;25:1286-95.
11. Koenders SS, van Dijk JD, Jager PL, Ottervanger JP, Slump CH, van Dalen JA. How to detect and correct myocardial creep in myocardial perfusion imaging using rubidium-82 PET? *J Nucl Cardiol*. 2019;26:729-34.
12. Kitkungvan D, Johnson NP, Roby AE, Patel MB, Kirkeeide R, Gould KL. Routine clinical quantitative rest stress myocardial perfusion for managing coronary artery disease: Clinical relevance of test-retest variability. *JACC Cardiovasc Imaging*. 2017;10:565-77.
13. Hoff CM, Sørensen J, Christensen NL, Bouchelouche K, Tolbod L. Activity regimes for 82Rb cardiac PET: Effects on absolute MBF and MPI. *J Nucl Cardiol*. 2020. <https://doi.org/10.1007/s12350-020-02266-2> (Epub ahead of print).
14. Farhad H, Dunet V, Bachelard K, Allenbach G, Kaufmann PA, Prior JO. Added prognostic value of myocardial blood flow quantitation in rubidium-82 positron emission tomography imaging. *Eur Heart J Cardiovasc Imaging*. 2013;14:1203-10.

15. Ziadi MC, deKemp RA, Williams KA, Guo A, Chow BJ, Renaud JM, et al. Impaired myocardial flow reserve on rubidium-82 positron emission tomography imaging predicts adverse outcomes in patients assessed for myocardial ischemia. *Cardiac imaging*. 2011;58:740-8.
16. Patel KK, Spertus JA, Chan PS, Sperry BW, Al Badarin F, Kennedy KF, et al. Myocardial blood flow reserve assessed by positron emission tomography myocardial perfusion imaging identifies patients with a survival benefit from early revascularization. *Eur Heart J*. 2020;41:759-68.
17. Gould KL, Johnson NP, Roby AE, Nguyen T, Kirkeeide R, Haynie M, et al. Regional, artery-specific thresholds of quantitative myocardial perfusion by PET associated with reduced myocardial infarction and death after revascularization in stable coronary artery disease. *J Nucl Med*. 2019;60:410-7.





# VALUE OF SIPM PET IN MYOCARDIAL PERFUSION IMAGING

USING RUBIDIUM-82

## Authors

S. S. Koenders<sup>1,2</sup>

J. A. van Dalen<sup>3</sup>

P. L. Jager,<sup>1</sup>

S. Knollema<sup>1</sup>

J. R. Timmer<sup>4</sup>

M. Mouden<sup>4</sup>

C. H. Slump<sup>2</sup>

J. D. van Dijk<sup>1</sup>

## Author Affiliations

1. Department of Nuclear Medicine, Isala Hospital, Zwolle, The Netherlands
2. Technical Medical Centre, University of Twente, Enschede, the Netherlands
3. Department of Medical Physics, Isala Hospital, Zwolle, The Netherlands
4. Department of Cardiology, Isala Hospital, Zwolle, The Netherlands

## Published in

Journal of Nuclear Cardiology 2020; Epub ahead of print





## ABSTRACT

### Background

PET scanners using silicon photomultipliers with digital readout (SiPM PET) have an improved temporal and spatial resolution compared to PET scanners using conventional photomultiplier tubes (PMT PET). However, the effect on image quality and visibility of perfusion defects in myocardial perfusion imaging (MPI) is unknown. Our aim was to determine the value of a SiPM PET scanner in MPI.

### Methods

We prospectively included 30 patients who underwent rest and regadenoson-induced stress Rubidium-82 (Rb-82) MPI on the D690 PMT PET (GE Healthcare) and within three weeks on the Vereos SiPM PET (Philips Healthcare). Two expert readers scored the image quality and assessed the existence of possible defects. In addition, interpreter's confidence, myocardial blood flow (MBF), and myocardial flow reserve (MFR) values were compared.

### Results

Image quality improved ( $p=0.03$ ) using the Vereos as compared to the D690. Image quality of the Vereos and the D690 was graded fair in 20% and 10%, good in 60% and 50%, and excellent in 20% and 40%, respectively. Defect interpretation and interpreter's confidence did not differ between the D690 and the Vereos ( $p>0.50$ ). There were no significant differences in rest MBF ( $p\geq 0.29$ ), stress MBF ( $p\geq 0.11$ ), and MFR ( $p\geq 0.51$ ).

### Conclusion

SiPM PET provides an improved image quality in comparison with PMT PET. Defect interpretation, interpreter's confidence, and absolute blood flow measurements were comparable between both systems. SiPM PET is therefore a reliable technique for MPI using Rb-82.

### Keywords

SiPM PET; Rb-82; myocardial blood flow; PET; myocardial perfusion imaging.

## INTRODUCTION

Myocardial perfusion imaging (MPI) using positron emission tomography (PET) is increasing in popularity over single photon emission computed tomography (SPECT) in the last years due to the increased availability of Strontium-82/Rubidium-82 (Rb-82) generators, higher spatial resolution, and higher sensitivity and specificity<sup>1</sup>. In addition, PET enables quantification of myocardial blood flow (MBF), which provides valuable additional prognostic information about the extent and functional importance of possible stenosis over visual assessment<sup>2-4</sup>.

Recently, new PET systems using silicon photomultipliers with digital readout (SiPM PET) have become available for clinical use<sup>5-8</sup>. In terms of system performance, the SiPM PET design results in an improved spatial and timing resolution and a relatively high count-rate capability as compared to PET scanners using conventional photomultiplier tubes (PMT PET)<sup>5-7,9,10</sup>. First oncology-PET studies showed that SiPM PET provides an improved image quality over PMT PET<sup>10-13</sup>. However, studies demonstrating the value of SiPM PET for MPI are still lacking. Hence, our aim was to determine the value of SiPM PET in comparison with PMT PET in MPI using Rb-82.

## MATERIALS AND METHODS

### Study design

We performed a prospective single-center study and included 30 consecutive patients referred for MPI using PMT PET (Discovery 690, GE Healthcare; D690) with Rb-82 for the evaluation of coronary artery disease. Within three weeks after the first PET scan, patients underwent a second MPI PET scan on a SiPM PET scanner (Vereos, Philips Healthcare). The local institutional ethics committee approved the study protocol and informed consent was obtained from all individual participants included in the study.

### Patient preparation and data acquisition

Patients were asked to refrain from caffeine containing beverages for at least 24 h before both scans. All patients underwent a rest scan followed by a regadenoson-induced stress scan on both scanners. First, a low-dose computed tomography (CT)-scan was performed for attenuation correction purposes. The CT scan on the D690 was performed using 0.8 s rotation time, pitch of 0.97, collimation of 32×0.625 mm, tube voltage of 120 kV, and tube current of 10 mA. On the Vereos, the CT scan was acquired using 1.5 s rotation time, pitch of 0.83, collimation of 64×0.625 mm, tube voltage of 120 kV, and tube current of 22 mA. The PET acquisition protocol was similar for the D690 and Vereos. A fixed activity of 740 MBq Rb-82 was intravenously administered with a flow rate of 50 mL/min using a strontium-82/Rb-82 generator (CardioGen-82, Bracco Diagnostics Inc.) immediately followed by a seven-minute PET acquisition. Ten minutes after the first activity bolus, stress was pharmacologically induced by administering 400 µg (5 mL) regadenoson over 10 seconds. After a 5 mL saline flush (NaCl 0.9%), the second activity bolus of 740 MBq was administered followed by a seven-minute stress PET acquisition. To obtain patient's effective radiation dose for both PET examinations we used the conversion factors of 0.00126 mSv/MBq

for rest and 0.00128 mSv/MBq for stress<sup>14,15</sup> resulting in a total dose of 1.9 mSv. To calculate the effective dose for the attenuation CT, we used a conversion factor of 0.014 mSv/(mGy·cm)<sup>16</sup> resulting in 0.2 mSv for the D690 based on an average dose length product (DLP) of 11.8 mGy·cm and 0.8 mSv for the Vereos based on an average DLP of 60.5 mGy·cm.

### Image reconstruction

CT data associated with the D690 were reconstructed using an iterative reconstruction method (70% adaptive statistical iterative reconstruction algorithm, ASIR) and a slice thickness of 5 mm. CT data associated with the Vereos were reconstructed using an iterative reconstruction method (iDose level 4) and a slice thickness of 3 mm.

We applied attenuation correction to all acquired PET data after semi-automatic registration of the CT and PET using the PET data acquired between 2:30 and 7:00 minutes<sup>17</sup>. We reconstructed the images of the D690 with a 3D-ordered subset expectation maximization (OSEM) technique using 2 iterations and 24 subsets and a Gaussian post-smoothing filter of 12 mm, as recommended by the manufacturer. The voxel size of the D690 was 3.3×3.3×3.3 mm<sup>3</sup>. Images of the Vereos were reconstructed with 3D OSEM using 3 iterations and 15 subsets and a Gaussian post-smoothing filter of 6 mm. The voxel size of the Vereos was 4.0×4.0×4.0 mm<sup>3</sup>. These Vereos settings were determined prior to our study (see appendix available online), based on measurements using an anthropomorphic torso phantom with a cardiac insert (model ECT/TOR/P, Data Spectrum Corp.). Intensity profiles through the cardiac insert were collected for several reconstruction settings to compare the full width at half maximum value to that of the D690. This way we obtained reconstruction settings resulting in an equivalent image resolution. For both the D690 and the Vereos data, corrections were performed for decay, scatter and random coincidences, and dead time effects. We used data acquired from 2:30 to 7:00 minutes for both rest and stress scans to obtain static images. Dynamic data sets were reconstructed using 26 time frames (12×5s, 6×10s, 4×20s and 4×40s). All reconstructed images were post-processed using Corridor4DM software (v2016).

### Visual assessment

Each set of static rest and stress PET images, showing the relative perfusion, was analyzed by two expert readers in consensus. They scored the image quality, visibility of perfusion defects, and interpreter's confidence. Image quality of the static images was assessed using a four-point grading scale: 1) poor, 2) fair, 3) good, and 4) excellent. Readers assessed the image quality based on myocardial count density and uniformity in well-perfused areas, signal to background noise, and shape of the left ventricle (LV). Static images were visually characterized as normal or abnormal. Abnormal scans were characterized as ischemic and/or irreversible. The interpreter's confidence was scored as either definite or equivocal. Readers were unaware of the patient's history or other clinical findings. Images were presented in random order and readers were blinded for the PET system.

### **MBF quantification**

Activity concentrations were measured in the 26 reconstructed time frames to calculate the time activity curves (TACs) for the LV, for the three vascular territories: left anterior descending (LAD), left circumflex (LCX) and right coronary (RCA) artery, and for the whole myocardium (global). The one-tissue compartment model of Lortie et al. based on a ROI methodology was used to calculate the MBF from the TACs<sup>18</sup>. Rest MBF was calculated without rate-pressure product correction. Furthermore, myocardial flow reserve (MFR) was calculated as the ratio between the stress and rest MBF. We categorized the global MFR values into three categories: high risk on cardiac failure with MFR <1.5, intermediate risk with MFR between 1.5 and 2.0, and low risk with MFR >2.0<sup>2,19</sup>.

Rest or stress MBF and MFR values were excluded from the comparison evaluation in case of unreliable TACs. Unreliable TACs were defined as TACs without a clear LV peak during the first-pass phase or a lack of steady state for the three vascular territories during the tissue phase, as previously described<sup>20</sup>. Test–retest precision was calculated as the standard deviation (SD) of the relative MBF and MFR differences, as previously defined by Kitkungvan et al.<sup>21</sup>. A test–retest precision  $\leq 21\%$  was considered acceptable<sup>21</sup>.

### **Statistical analysis**

Patient-specific parameters and characteristics were determined as mean  $\pm$  SD, or as percentages using SPSS (IBM SPSS Statistics for Windows, Version 24.0). Image quality, MBF and MFR measurements were compared using the Wilcoxon signed rank test. In addition, the visibility of perfusion defects and interpreter's confidence were compared using the McNemar test. The level of statistical significance was set to 0.05 for all statistical analyses.

## **RESULTS**

### **Baseline characteristics**

The baseline characteristics of the included patients are summarized in Table 1.

### **Visual assessment**

Image quality of the static images improved ( $p=0.03$ ) using the Vereos as compared to the D690. Image quality of the D690 and the Vereos was graded fair in 20% (6/30) and 10% (3/30), good in 60% (18/30) and 50% (15/30), and excellent in 20% (6/30) and 40% (12/30), respectively, as illustrated in Figure 1. None of the images using either the D690 or the Vereos were scored as poor. An example of the image quality for patients with high and low BMI is shown in Figure 2.

Defect interpretation did not differ in 93% (28/30) of the patient scans between the D690 and the Vereos ( $p=0.50$ ). In the 7% (2/30) of patient scans where defect interpretation differed, the scans were scored as normal on the D690, whereas they were interpreted to show ischemia on the Vereos (Figures 3 and 4). Patient scans were scored as normal in 80% (24/30) and 73% (22/30) for the D690

**Table 1.** Baseline characteristics of all included patients (N=30) who underwent clinically indicated Rb-82 PET MPI.

Characteristic	All patients (N=30)
Age (years)	64 ± 9
Male gender (%)	80
Weight (kg)	87 ± 15
Height (cm)	176 ± 9
BMI (kg/m <sup>2</sup> )	28.0 ± 4.4
Current smoker (%)	13
Hypertension (%)	50
Diabetes (%)	20
Dyslipidemia (%)	40
Family history (%)	53

*Data are presented as mean ± SD or as percentage*

and the Vereos, respectively. Furthermore, 10% (3/30) and 17% (5/30) was interpreted as showing ischemia and for both PET scanners 13% (4/30) was scored as showing an irreversible defect. There was no difference in interpreter's confidence as all scans were scored as definite.

### MBF quantification

Of the 30 included patients, both rest and stress MBF values of one patient were excluded due to unreliable rest and stress TACs. Furthermore, rest MBF values of another patient and stress MBF values of four other patients were excluded due to unreliable TACs. The main reason for an unreliable TAC was no clear or absent LV peak, which would be most likely caused by a pinched vein<sup>22</sup>. The remaining PET scans provided a paired comparison of 28 rest MBF values, 25 stress MBF values, and 24 MFR values.

There were no significant differences in any of the vascular territories nor in the whole myocardium regarding the rest MBF ( $p \geq 0.29$ ), stress MBF ( $p \geq 0.11$ ) or MFR ( $p \geq 0.51$ ), as shown in Table 2 and Figure 5. When categorizing the global MFR values into high, intermediate, and low risk on cardiac failure, 25% (6/24) of the patients were reclassified when using the Vereos. More specifically, one patient was reclassified from intermediate risk to high risk, three from intermediate risk to low risk, and two patients from low risk to intermediate risk. None of the patients were reclassified from low risk to high risk or vice versa. Moreover, test–retest precision of global rest MBF, stress MBF, and MFR was 18%, 16%, and 21%, respectively, and was considered to be within the previously reported test–retest precision of 21%, as shown in Figure 6.

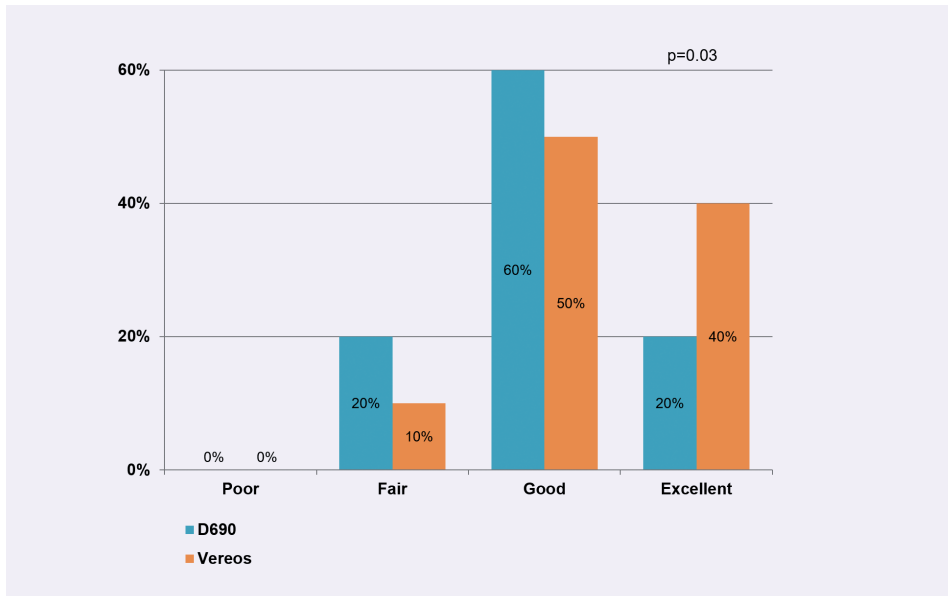


Figure 1. Barplot showing the percentage of images scored as poor, fair, good, and excellent for the D690 and Vereos PET system. Image quality improved for the Vereos ( $p=0.03$ ).

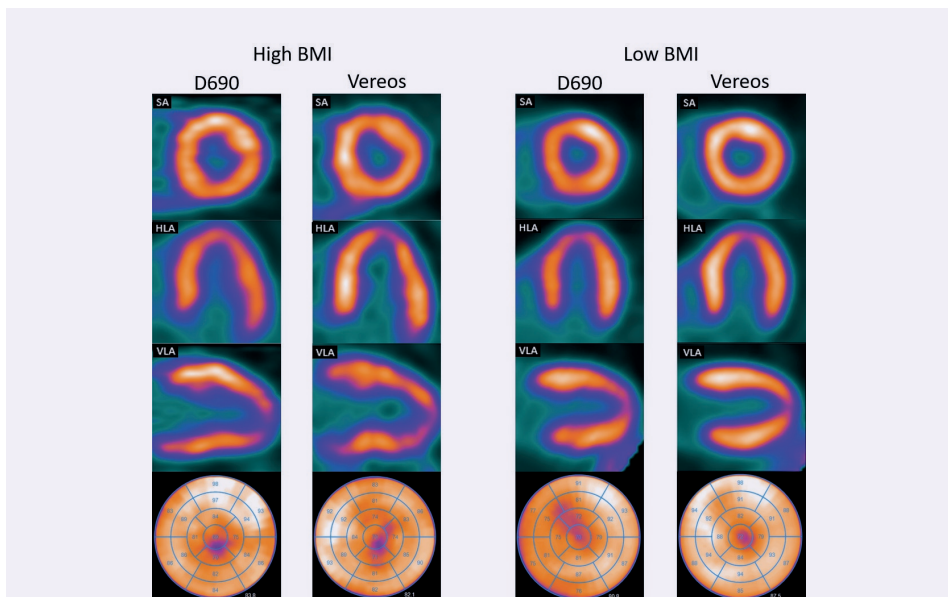


Figure 2. Example of the rest study from two patients scanned on the D690 and Vereos PET system. The images on the left are from a patient with a high BMI ( $36.5 \text{ kg/m}^2$ ) and on the right of a patient with a low BMI ( $19.2 \text{ kg/m}^2$ ). From top to bottom: SA; short axis, HLA; horizontal long axis, VLA; vertical long axis, bull's eye.

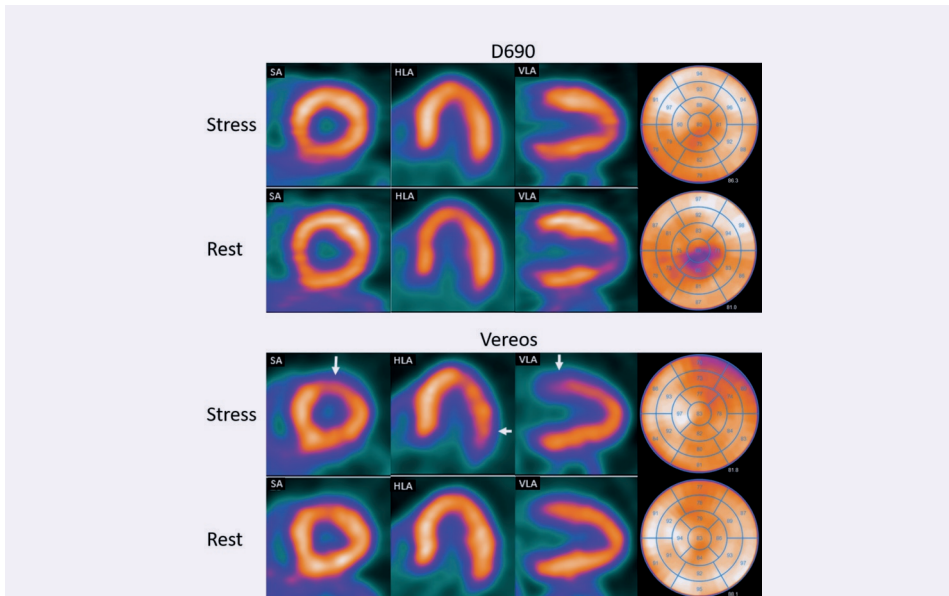


Figure 3. Example of a rest and stress study from the same patient scanned on the D690 (top) and Vereos (bottom). The images of the D690 show no defect while the images of the Vereos show a small reversible defect in the basal anterolateral wall (white arrows). From left to right: SA; short axis, HLA; horizontal long axis, VLA; vertical long axis, bull's eye.

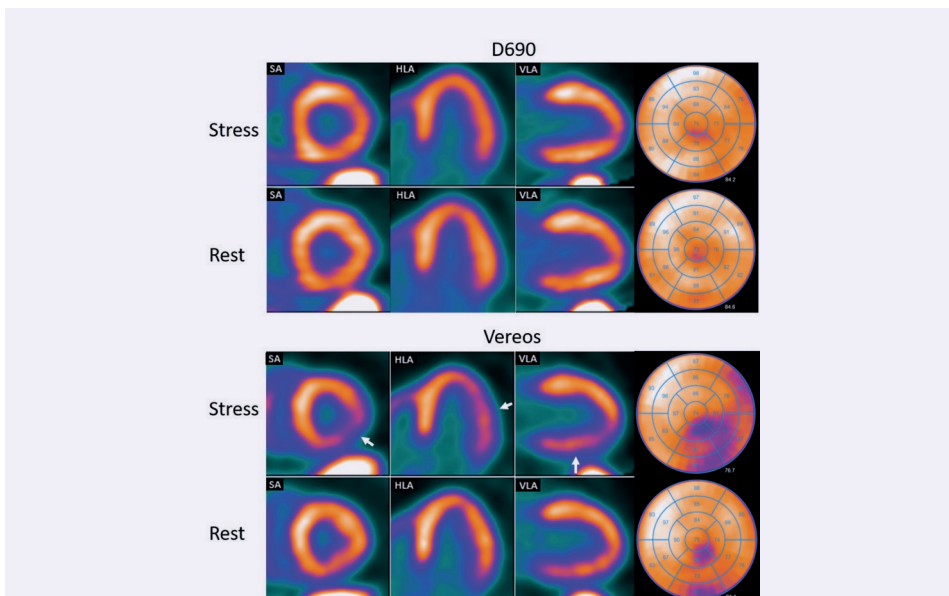


Figure 4. Example of a rest and stress study from the same patient scanned on the D690 (top) and Vereos (bottom). The images of the D690 show no defect while the images of the Vereos show a moderate reversible defect in the inferolateral wall (white arrows). From left to right: SA; short axis, HLA; horizontal long axis, VLA; vertical long axis, bull's eye.

**Table 2.** Rest and stress MBF (mL/min/g) and MFR values calculated for the D690 and the Vereos PET scans, for the three vascular territories (LAD, LCX, and RCA) and the whole myocardium (global). No significant differences were observed between the D690 and the Vereos PET ( $p \geq 0.11$ )

Territory	PET scanner	Rest MBF (N=28)	Stress MBF (N=25)	MFR (N=24)
LAD	D690	0.9 [0.7-1.1]	2.0 [1.8-2.5]	2.3 [2.0-2.8]
	Vereos	0.9 [0.7-1.0]	2.2 [1.7-2.4]	2.3 [2.0-2.7]
LCX	D690	0.9 [0.7-1.1]	2.2 [1.9-2.5]	2.3 [2.0-2.9]
	Vereos	0.9 [0.7-1.1]	2.1 [1.6-2.3]	2.3 [1.8-2.7]
RCA	D690	0.9 [0.7-1.1]	2.2 [2.0-2.5]	2.3 [2.0-3.0]
	Vereos	0.9 [0.7-1.2]	2.3 [2.0-2.9]	2.4 [1.9-3.3]
Global	D690	0.9 [0.7-1.0]	2.0 [1.8-2.5]	2.3 [2.0-2.9]
	Vereos	0.9 [0.7-1.0]	2.1 [1.7-2.5]	2.3 [2.0-2.8]

Data are presented as median (interquartile range)

LAD, left anterior descending; LCX, left circumflex; MBF, myocardial blood flow; MFR, myocardial flow reserve; and RCA, right coronary artery

## DISCUSSION

In this study, we showed that the Vereos SiPM PET scanner provided an improved image quality for MPI using Rb-82 as compared to the D690 PET scanner using conventional photomultiplier tubes. There were no significant differences in defect interpretation or in quantitative MBF and MFR measurements.

According to previously performed phantom and patients studies,<sup>6, 10-13</sup> SiPM PET showed an improved image quality and lesion detection for oncology patients as compared to PMT PET. It seems that these results can be generalized to cardiac imaging as shown in our study. In addition, scan interpretation might change as well when shifting from PMT PET to SiPM PET. In our population, images from two out of 30 patients showed ischemia on the Vereos PET scan, whereas these images were interpreted as normal on the D690 PET scan. Of these patients, one had no follow-up imaging and no events within the first year after the Vereos PET scan (Figure 3). Global MFR values of this patient were 2.15 using the D690 (low risk) and 1.87 using the Vereos (intermediate risk). In the other patient (Figure 4), a subtotal stenosis was seen in the circumflex area during coronary angiography one month after the second PET scan, corresponding to the ischemic area in the Vereos PET images. Global MFR values of this patient were 1.72 using the D690 (intermediate risk) and 1.40 using the Vereos (high risk). It is well known that perfusion defects can be introduced due to misregistration of attenuation CT and PET data<sup>23-25</sup>. For each scan, we verified the co-registration between CT and PET data. In none of the scans, a misregistration was observed.

For MBF quantification, the Vereos showed reliable MBF and MFR measurements using Rb-82. This is in line with the results of the study by Van Dijk et al. who performed a cardiac-phantom study and



concluded that the D690 and the Vereos scanner showed a comparable count-rate performance for Rb-82 activities up to approximately 1000 MBq<sup>26</sup>. However, in our study, 25% (6/24) of the patients were reclassified according to the global MFR values from intermediate risk to low/high risk or vice versa when shifting to the Vereos. The relative differences of these six patients were 38%, 15%, 10%, -14%, -19% and -21%. Although 25% seems to be a large percentage, it is possible that a patient classified as having an intermediate risk may be classified as having a low/high risk when repeating the scan and reprocessing the data, solely due to the relatively large test–retest precision in MBF and MFR measurements of typically 21%<sup>21</sup>. Therefore, reclassification in 25% of the patients is not solely due to the differences in scanner performance. Furthermore, test–retest precision was calculated as the SD of the relative MBF and MFR differences for all patients. Therefore, by definition, approximately 68% of all test–retest values should be within the test–retest precision of 21%.

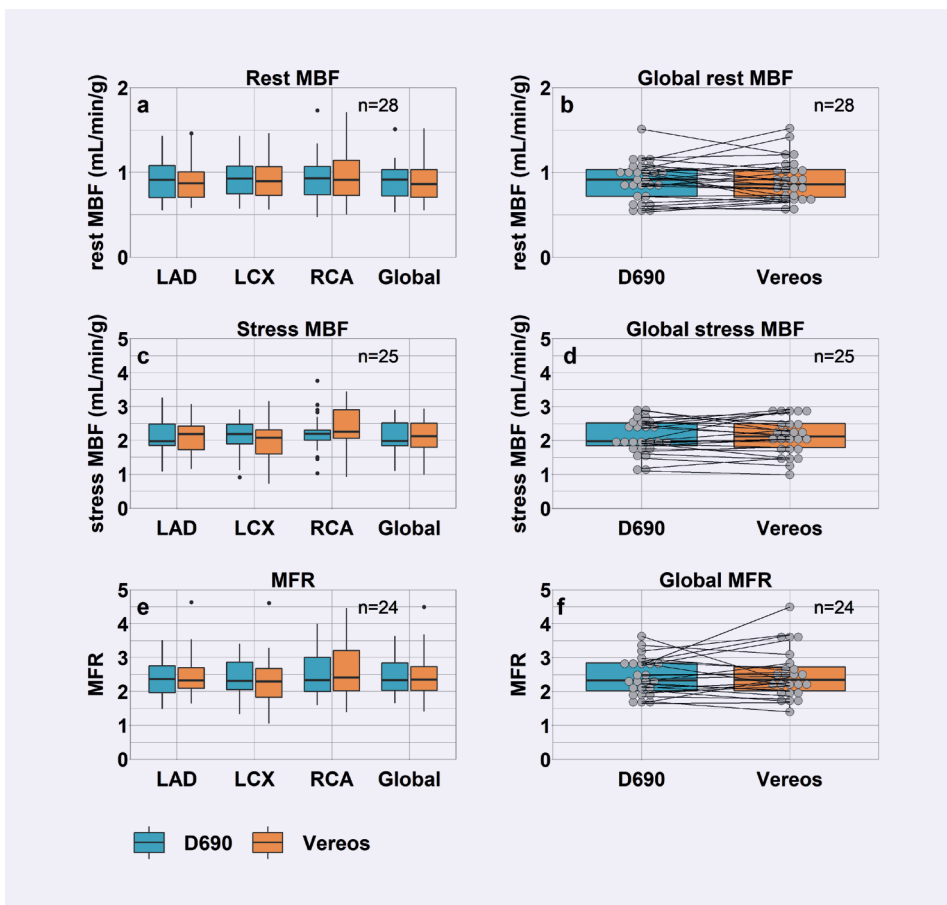


Figure 5. Boxplots showing (a+b) comparable rest (N=28) and (c+d) stress (N=25) myocardial blood flows (MBFs) and (e+f) myocardial flow reserves (MFRs) (N=24) for the three vascular territories and for the whole myocardium (global) between the D690 and Vereos PET system. The individual global (b) rest MBF, (d) stress MBF and (f) MFR values are shown as well.

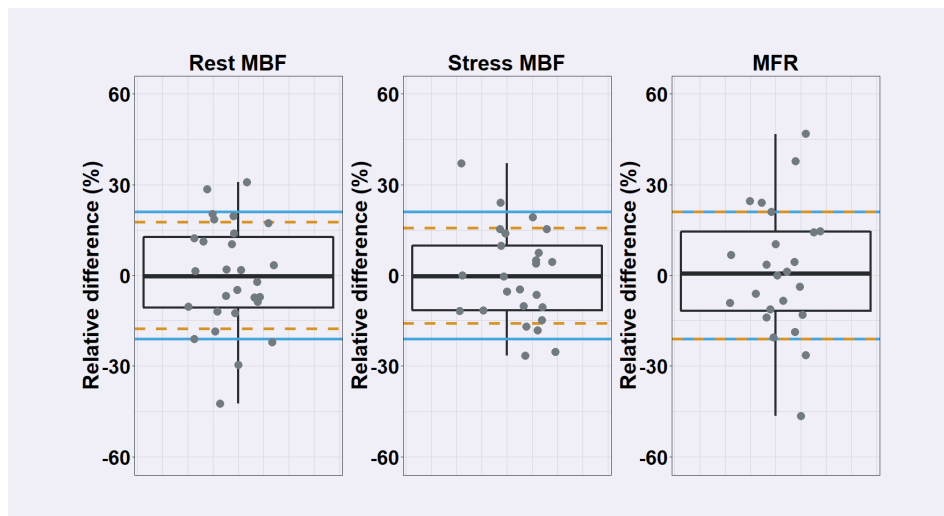


Figure 6. Boxplots showing individual relative differences (%) of the rest MBF (N=28), stress MBF (N=25), and MFR (N=24) when comparing the D690 with the Vereos PET system. The SD of the relative differences by the orange dashed lines and the test–retest precision of 21% by the blue solid lines. Each dot represents a single patient. As the MFR is the ratio between stress and rest MBF, large MFR differences presumably arise from a large change in stress MBF and minimal change in rest MBF or vice versa.

This study had several limitations that should be recognized. First, our study population was relatively small (N=30). Still, the interpreter’s confidence was scored as definite in 100% of the scans so it is unlikely that including more patients will give a significant change in the interpreter’s confidence between the Vereos and D690. However, our study did show a change in defect interpretation in 2 patients. Inclusion of more patients is necessary to find out if there is a significant change in defect interpretation and validation studies are required to determine a possible superior diagnostic performance of the Vereos SiPM PET over the D690 PMT PET. Furthermore, we found relative MBF and MFR differences within the 21% test–retest precision. It is not likely that this will change when more patients are included.

Secondly, some elements of the acquisition have to be addressed. As we used Rb-82, the positron range (5.9 mm) is rather large compared to for example  $^{13}\text{N}$ -ammonia (1.5 mm), which results in a worse image resolution compared to using other PET MPI tracers<sup>27</sup>. The higher spatial resolution of the SiPM PET as compared to PMT PET may therefore result in an even better image quality when using other PET tracers than Rb-82. Moreover, the injected activity used in this study is lower than generally recommended (740 MBq vs. 1110 MBq),<sup>2</sup> but sufficient for MBF quantification<sup>26, 28</sup>. In addition, we used a PMT PET scanner with a relatively high count-rate capability. Therefore, our results may not be generalizable to older PMT PET scanners as they might not be able to process the high count-rates adequately due to dead time effects<sup>26, 28</sup>. Inaccurate count-rate measurements can result in unreliable MBF and MFR measurements<sup>29</sup>.

Lastly, expert readers had no access to clinical information, i.e., gender, age, or calcium score when interpreting the images. Although there was no significant difference in defect interpretation, it still differed in two patients. Access to clinical information might have altered their decision-making and could have overcome this different interpretation.

### **Clinical implications**

The Vereos scanner was the first SiPM PET scanner available for clinical use<sup>6</sup> after which two other SiPM PET scanners became available, namely, the Biograph Vision PET/CT (Siemens Healthineers) and the Discovery MI (GE healthcare)<sup>7, 8</sup>. As the performance characteristics of SiPM PET are in general better than those of PMT PET, image quality is expected to improve for all three SiPM PET scanners. Moreover, flow measurements are expected to be similar or possibly more accurate as compared to using PMT PET, provided that PMT PET has a sufficient count-rate capability<sup>7, 8, 26, 28, 29</sup>.

Whereas the MFR was shown to be robust when using different advanced reconstruction settings or software packages, one should be cautious in the occurrence of possible systematic changes in MBF measurements<sup>30, 31</sup>. Furthermore, one has to be aware of a relatively large test–retest precision in MBF and MFR measurements of typically 21%. In general, a MFR<1.5 is associated with an increased risk on cardiac failure while patients with a MFR>2.0 are associated with a reduced risk on cardiac failure.<sup>2, 19</sup> Hence, it is possible that a patient classified as having an intermediate risk may be classified as a low/high-risk patient when repeating the scan and reprocessing the data, solely due to the test–retest variation.

### **New knowledge gained**

The use of the Vereos SiPM system in PET Rb-82 MPI results in an improved image quality and no significant differences for visual interpretation or interpreter’s confidence in comparison with the conventional D690 PMT PET scanner. Furthermore, no significant differences were found in MBF and MFR quantification. We did find a change in visual defect interpretation in two patients. Defect interpretation may therefore differ and it could be possible that the Vereos SiPM PET system has a superior diagnostic performance over the conventional D690 PMT PET system. Additional studies with a larger patient population are required to confirm this.

## **CONCLUSIONS**

PET using silicon photomultipliers with digital readout is a reliable technique for MPI using Rb-82 as it provides an improved image quality and similar interpreter’s confidence, defect interpretation, and absolute blood flow measurements as compared to PET using conventional photomultiplier tubes.

**Disclosures**

This work was supported by a research grant of Philips Healthcare. The content of the article was solely the responsibility of the authors.

**Ethical approval**

All procedures performed in studies involving human participants were in accordance with the ethical standards of the institutional and/or national research committee (METC Isala Zwolle, NL63853.075.17) and with the 1964 Helsinki declaration and its later amendments or comparable ethical standards.

**Informed consent**

Informed consent was obtained from all individual participants included in the study.

## REFERENCES

1. Mc Ardle BA, Dowsley TF, deKemp RA, Wells GA, Beanlands RS. Does rubidium-82 PET have superior accuracy to SPECT perfusion imaging for the diagnosis of obstructive coronary disease?: A systematic review and meta-analysis. *J Am Coll Cardiol* 2012;60:1828-37.
2. Murthy V, Bateman T, Beanlands R, Berman D, Borges-Neto S, Chareonthaitawee P, et al. Clinical quantification of myocardial blood flow using PET: Joint position paper of the SNMMI cardiovascular council and the ASNC. *J Nucl Cardiol* 2018;25:269-97.
3. Ziadi M, deKemp R, Williams K, Guo A, Renaud J, Chow B, et al. Does quantification of myocardial flow reserve using rubidium-82 positron emission tomography facilitate detection of multivessel coronary artery disease? *J Nucl Cardiol* 2012;19:670-80.
4. Sciagra R, Passeri A, Bucerus J, Verberne HJ, Slart, Riemer H. J. A., Lindner O, et al. Clinical use of quantitative cardiac perfusion PET: Rationale, modalities and possible indications. position paper of the cardiovascular committee of the european association of nuclear medicine (EANM). *Eur J Nucl Med Mol Imaging* 2016;43:1530-45.
5. Slomka PJ, Pan T, Germano G. Recent advances and future progress in PET instrumentation. *Semin Nucl Med* 2016;46:5-19.
6. Miller M, Zhang J, Binzel K, Griesmer J, Laurence T, Narayanan M, et al. Characterization of the vereos digital photon counting PET system. *J Nucl Med* 2015;56(supplement 3):434.
7. van Sluis JJ, de Jong J, Schaar J, Noordzij W, van Snick P, Dierckx R, et al. Performance characteristics of the digital biograph vision PET/CT system. *J Nucl Med* 2019;60:1031-6.
8. Hsu DFC, Ilan E, Peterson WT, Uribe J, Lubberink M, Levin CS. Studies of a next-generation silicon-Photomultiplier–Based time-of-flight PET/CT system. *J Nucl Med* 2017;58:1511-8.
9. Slomka PJ, Pan T, Berman DS, Germano G. Advances in SPECT and PET hardware. *Prog Cardiovasc Dis* 2015;57:566-78.
10. Van der Vos CS, Koopman D, Rijnsdorp S, Arends AJ, Boellaard R, van Dalen JA, et al. Quantification, improvement, and harmonization of small lesion detection with state-of-the-art PET. *Eur J Nucl Med Mol Imaging* 2017;44:4-16.
11. López-Mora DA, Flotats A, Fuentes-Ocampo F, Camacho V, Fernández A, Ruiz A, et al. Comparison of image quality and lesion detection between digital and analog PET/CT. *Eur J Nucl Med Mol Imaging* 2019;46:1383-90.
12. van Sluis J, Boellaard R, Somasundaram A, van Snick P, Borra R, Dierckx R, et al. Image quality and semi-quantitative measurements of the siemens biograph vision PET/CT: Initial experiences and comparison with siemens biograph mCT PET/CT. *J Nucl Med* 2020;61:129-35.
13. Nguyen NC, Vercher-Conejero JL, Sattar A, Miller MA, Maniawski PJ, Jordan DW, et al. Image quality and diagnostic performance of a digital PET prototype in patients with oncologic diseases: Initial experience and comparison with analog PET. *J Nucl Med* 2015;56:1378-85.
14. Senthamizhchelvan S, Bravo PE, Esaias C, Lodge MA, Merrill J, Hobbs RF, et al. Human biodistribution and radiation dosimetry of <sup>82</sup>Rb. *J Nucl Med* 2010;51:1592-9.

15. Senthamizchelvan S, Bravo PE, Lodge MA, Merrill J, Bengel FM, Sgouros G. Radiation dosimetry of  $^{82}\text{Rb}$  in humans under pharmacologic stress. *J Nucl Med* 2011;52:485-91.
16. Deak PD, Smal Y, Kalender WA. Multisection CT protocols: Sex- and age-specific conversion factors used to determine effective dose from dose-length product. *Radiol* 2010;257:158-66.
17. van Dijk JD, Jager PL, Ottervanger JP, Slump CH, van Dalen JA. No need for frame-wise attenuation correction in dynamic rubidium-82 PET for myocardial blood flow quantification. *J Nucl Cardiol* 2019;26:738-45.
18. Lortie M, Beanlands R, Yoshinaga K, Klein R, DaSilva J, deKemp R. Quantification of myocardial blood flow with  $^{82}\text{Rb}$  dynamic PET imaging. *Eur J Nucl Med Mol Imaging* 2007;34:1765-74.
19. Murthy V, Di Carli M. Non-invasive quantification of coronary vascular dysfunction for diagnosis and management of coronary artery disease. *J Nucl Cardiol* 2012;19:1060-72.
20. Koenders SS, van Dijk JD, Jager PL, Ottervanger JP, Slump CH, van Dalen JA. Impact of regadenoson-induced myocardial creep on dynamic rubidium-82 PET myocardial blood flow quantification. *J Nucl Cardiol* 2019;26:719-28.
21. Kitkungvan D, Johnson NP, Roby AE, Patel MB, Kirkeeide R, Gould KL. Routine clinical quantitative rest stress myocardial perfusion for managing coronary artery disease: Clinical relevance of test-retest variability. *JACC Cardiovasc Imaging* 2017;10:565-77.
22. van Dijk JD, Jager PL, van Dalen JA. Pitfalls in myocardial blood flow quantification with rubidium-82 PET. *Tijdschr voor Nucl Geneeskde* 2017;39:1822-9.
23. Loghin C, Sdringola S, Gould KL. Common artifacts in PET myocardial perfusion images due to attenuation-emission misregistration: Clinical significance, causes, and solutions. *J Nucl Med* 2004;45:1029.
24. Martinez-Moller A, Souvatzoglou M, Navab N, Schwaiger M, Nekolla SG. Artifacts from misaligned CT in cardiac perfusion PET/CT studies: Frequency, effects, and potential solutions. *J Nucl Med* 2007;48:188.
25. Gould KL, Pan T, Loghin C, Johnson NP, Guha A, Sdringola S. Frequent diagnostic errors in cardiac PET/CT due to misregistration of CT attenuation and emission PET images: A definitive analysis of causes, consequences, and corrections. *J Nucl Med* 2007;48:1112-21.
26. van Dijk J, Jager P, van Osch J, Khodaverdi M, van Dalen J. Comparison of maximal rubidium-82 activities for myocardial blood flow quantification between digital and conventional PET systems. *J Nucl Cardiol* 2019;26:1286-91.
27. Jødal L, Le Loirec C, Champion C. Positron range in PET imaging: An alternative approach for assessing and correcting the blurring. *Phys Med Biol* 2012;57:3931-43.
28. Renaud JM, Yip K, Guimond J, Trottier M, Pibarot P, Turcotte E, et al. Characterization of 3-dimensional PET systems for accurate quantification of myocardial blood flow. *J Nucl Med* 2017;58:103-9.
29. deKemp RA, Yoshinaga K, Beanlands RSB. Will 3-dimensional PET-CT enable the routine quantification of myocardial blood flow? *J Nucl Cardiol* 2007;14:380-97.
30. Tahari AK, Lee A, Rajaram M, Fukushima K, Lodge MA, Lee BC, et al. Absolute myocardial flow quantification with ( $^{82}\text{Rb}$ ) PET/CT: Comparison of different software packages and methods. *Eur J Nucl Med Mol Imaging* 2014;41:126-35.

31. Armstrong I, Tonge C, Arumugam P. Impact of point spread function modeling and time-of-flight on myocardial blood flow and myocardial flow reserve measurements for rubidium-82 cardiac PET. *J Nucl Cardiol* 2014;21:467-74.





# EFFECT OF TEMPORAL SAMPLING PROTOCOLS ON MYOCARDIAL BLOOD FLOW MEASUREMENTS

## USING RUBIDIUM-82 PET

### Authors

S. S. Koenders<sup>1,2</sup>

J. D. van Dijk<sup>1</sup>

P. L. Jager<sup>1</sup>

M. Mouden<sup>3</sup>

A. G. Tegelaar<sup>1</sup>

C. H. Slump<sup>2</sup>

J. A. van Dalen<sup>4</sup>

### Author Affiliations

1. Department of Nuclear Medicine, Isala Hospital, Zwolle, The Netherlands
2. Technical Medical Centre, University of Twente, Enschede, the Netherlands
3. Department of Cardiology, Isala Hospital, Zwolle, The Netherlands
4. Department of Medical Physics, Isala Hospital, Zwolle, The Netherlands

### Published in

Journal of Nuclear Cardiology 2021; Epub ahead of print



## ABSTRACT

### Background

A variety of temporal sampling protocols is used worldwide to measure myocardial blood flow (MBF). Both the length and number of time frames in these protocols may alter MBF and myocardial flow reserve (MFR) measurements. We aimed to assess the effect of different clinically used temporal sampling protocols on MBF and MFR quantification in Rubidium-82 (Rb-82) PET imaging.

### Methods

We retrospectively included 20 patients referred for myocardial perfusion imaging using Rb-82 PET. A literature search was performed to identify appropriate sampling protocols. PET data were reconstructed using 14 selected temporal sampling protocols with time frames of 5-10 seconds in the first-pass phase and 30-120 seconds in the tissue phase. Rest and stress MBF and MFR were calculated for all protocols and compared to the reference protocol with 26 time frames.

### Results

MBF measurements differed ( $p < 0.003$ ) in six (43%) protocols in comparison to the reference protocol, with mean absolute relative differences up to 16% (range 5%-31%). Statistically significant differences were most frequently found for protocols with tissue phase time frames  $< 90$  seconds. MFR did not differ ( $p \geq 0.11$ ) for any of the protocols.

### Conclusions

Various temporal sampling protocols result in different MBF values using Rb-82 PET. MFR measurements were more robust to different temporal sampling protocols.

### Keywords

Myocardial blood flow; PET myocardial perfusion imaging; Rb-82; temporal sampling; regadenoson.

## INTRODUCTION

Quantification of myocardial blood flow (MBF) and myocardial flow reserve (MFR) using Rubidium-82 (Rb-82) PET is increasingly used in daily clinical practice. It provides valuable prognostic information in addition to the visual evaluation of myocardial perfusion imaging (MPI) PET data in the detection and evaluation of coronary artery disease (CAD)<sup>1-5</sup>. The increasing use of MBF and MFR quantification among multiple hospitals performing Rb-82 PET MPI and the lack of consensus in literature and guidelines on reconstruction protocols has led to a wide variety of temporal sampling protocols that could limit accuracy and data comparison between centers<sup>6,7</sup>.

A temporal sampling protocol is used to reconstruct dynamic images. These dynamic images are then used to determine the tracer activity concentration in the blood pool (left ventricle (LV)) and myocardial tissue over time in order to quantify MBF and MFR<sup>3</sup>. It is important that these measurements are accurate as the resulting time–activity curves (TACs) are used as input for compartmental analysis to calculate the MBF<sup>3,8,9</sup>. Both the length and the number of time frames in the temporal sampling protocol may influence the measured TACs and may therefore alter MBF and MFR measurements<sup>10</sup>. In order to interchange and interpret MBF and MFR values across different centers, it is important to know the effect of temporal sampling on absolute MBF and MFR measurements. Therefore, our aim was to assess the effect of various clinically used temporal sampling protocols on MBF and MFR quantification.

## MATERIALS AND METHODS

### Temporal sampling protocol selection

A literature search was performed using the Scopus database to find articles available in September 2020. The search strategy to identify all possible temporal sampling protocols used in clinical practice involved the use of the following terms in the title, keywords or abstract: “Rubidium” or “Rb,” and “myocardial blood flow” or “MBF” or “flow,” and “quantification” or “sampling” or “dynamic” or “time frame” or “frame time,” and not “dog” or “canine” or “rabbit,” or “animal.” The full texts of all the articles that were found were screened for temporal sampling protocols used for Rb-82 PET MPI. Exclusion criteria were study populations consisting of animals and phantom or simulation studies. Furthermore, Lee et al. suggest not to use time frames <5 seconds during the first-pass (blood pool) phase, as these may contain inadequate count statistics<sup>6,10</sup>. Therefore, protocols using time frames <5 seconds during the first-pass phase were excluded. Protocols using time frames >10 seconds in the first-pass phase were also excluded as these are likely to result in under-sampling of the left ventricle TAC<sup>3</sup>.

### Study design

We retrospectively included 20 patients referred for MPI using Rb-82 PET/CT (Vereos, Philips Healthcare) who underwent dynamic rest and regadenoson-induced stress imaging. These 20 patients comprised 10 patients with a scan interpreted as normal by a nuclear medicine physician and 10 in whom the Rb-82 PET scan was interpreted as abnormal (ischemic or irreversible defect). In this way, we ensured the

applicability not only in patient scans interpreted as normal but also in patient scans with less perfusion. Approval by the medical ethics committee was not required according to Dutch law as this study was performed retrospectively. Nevertheless, all patients provided written informed consent for the use of their data for research purposes.

### **Patient preparation and data acquisition**

All subjects were asked to abstain from caffeine-containing substances for 24 hours and to discontinue dipyridamole-containing medication for 48 hours before imaging. Preceding to MPI, a low-dose CT scan was acquired using 1.5 seconds rotation time, a pitch of 0.83, a collimation of  $64 \times 0.625$  mm, a tube voltage of 120 kV, and a tube current of 22 mA. Next, 740 MBq Rb-82 was administered intravenously with a flow rate of 50 mL/min using a Strontium-82/Rb-82 generator (CardioGen-82, Bracco Diagnostics Inc.). Ten minutes after the first elution, we induced pharmacological stress by administering 400  $\mu$ g (5 mL) of regadenoson over 10 seconds. After a 5 mL saline flush (NaCl 0.9%), we administered a second dose of 740 MBq Rb-82. We acquired seven-minute PET list-mode acquisitions on the PET system after both Rb-82 administrations. CT-based attenuation correction was applied after registration of CT and PET data.

### **Data processing**

CT data were reconstructed using an iterative reconstruction method (iDose level 4) and a slice thickness of 3 mm. PET images were reconstructed with 3D ordered subset expectation maximization (OSEM) using 2 iterations and 15 subsets and a 3D Gaussian post-smoothing filter of 6 mm. Corrections were performed for decay, attenuation, scatter and random coincidences, and dead time effects. The reconstructed dynamic images were post-processed by the same experienced operator using Corridor4DM software (v2017).

Myocardium contours were automatically detected in both rest and stress scans based on the static images which were reconstructed from the data acquired between 2:30 and 7:00 minutes (tissue phase). Furthermore, a region of interest (ROI) was automatically placed in the images. If needed, this ROI was manually replaced to the location of the mitral valve to estimate the activity in the blood pool as shown in Figure 1<sup>11</sup>. This was done by assigning an imaginary line between the septal and lateral wall which has to run through the center of the ROI as shown in Figure 1. We manually checked and corrected the dynamic images for the presence or myocardial creep<sup>12</sup>. The activity concentrations in the myocardium contour and ROI were measured in the reconstructed time frames of the different temporal sampling protocols to calculate the TACs for the LV, the whole myocardium (global), and the three vascular territories: left anterior descending (LAD), left circumflex (LCX), and right coronary artery (RCA). The one-tissue compartment (1-TCM) model of Lortie et al. based on an ROI methodology was used to calculate the absolute MBF from the TACs using Corridor4DM<sup>13</sup>. Furthermore, the MFR, defined as the stress MBF divided by the rest MBF, was automatically calculated as well.

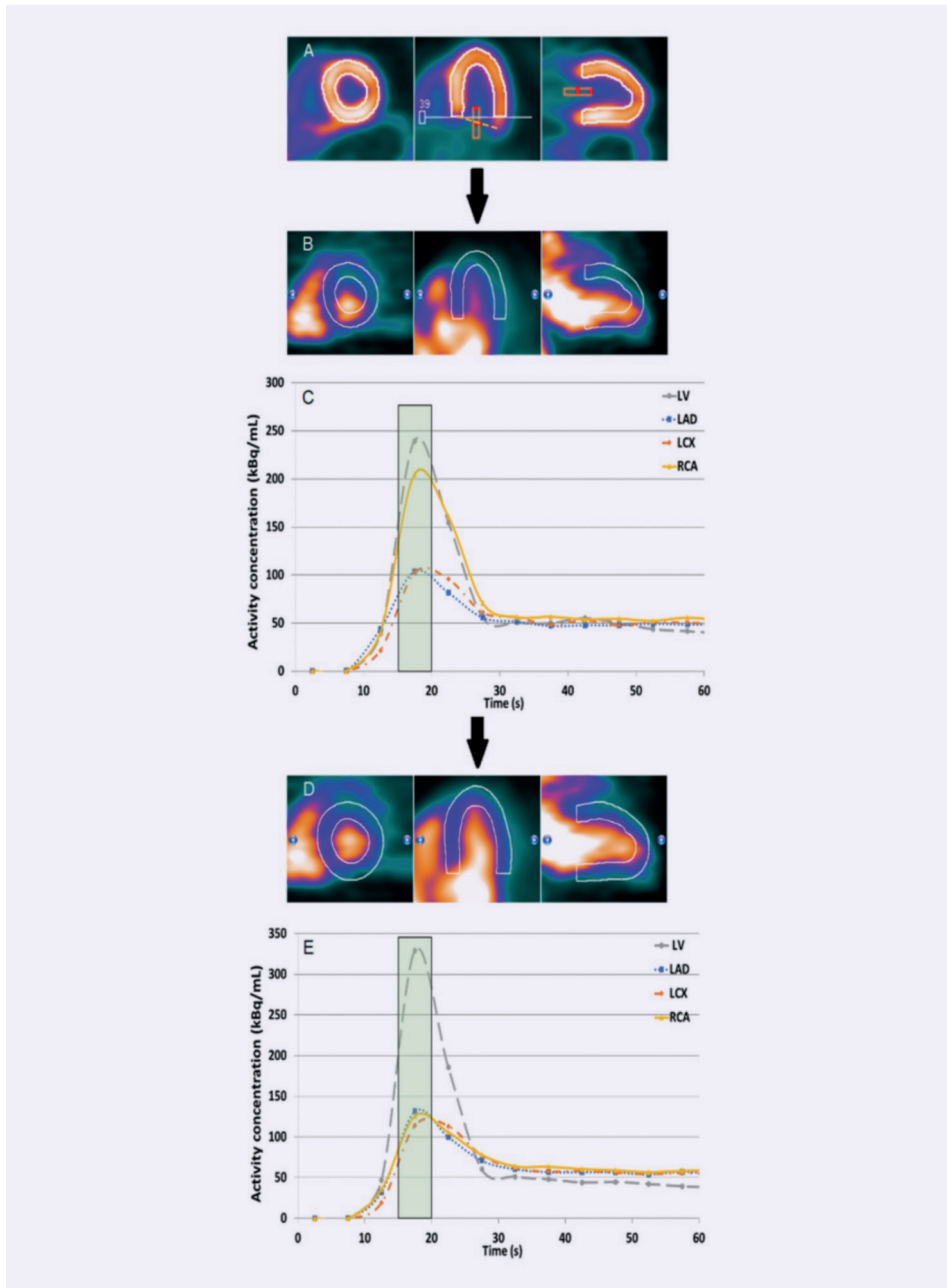


**Figure 1.** Overview of the three main steps to detect and correct for myocardial movement using Corridor4DM, adapted from Koenders et al.<sup>11</sup>. The activity concentration in the left ventricle (LV) was measured by the red rectangular region of interest (ROI) which was placed at the center of the imaginary line (yellow dashed line) between the septum and lateral wall, the mitral valve (A). The myocardium contour (white lines in A, B and D) was automatically drawn by assigning the most basal part of the septum which still contains activity. If needed, we corrected for myocardial movement (B, C) by manually realigning the myocardium contour with the activity in each individual time frame (D, E).

The protocol stated to be most optimal by Lee et al. uses 26 frames (24×5s, 2×120s) and was used as reference<sup>10</sup>. MBF values were excluded in case of an unreliable TAC when using the reference protocol. An unreliable TAC was defined as a TAC without a clear LV peak during the first-pass phase when activity reaches the LV, or a lack of steady state during the tissue phase when the activity is only present in the myocardium, as explained by Koenders et al.<sup>12</sup>. We post-processed the reference protocol (26A) a second time (26A\*) to ascertain the reproducibility of post-processing the data. Absolute relative differences in rest MBF, stress MBF, and MFR measurements as compared to the values obtained using the reference protocol were calculated and classified into two categories: ≤10% and >10%.

### Statistical analysis

Patient-specific parameters and characteristics were determined as percentage or mean ± standard deviation (SD). For each patient, we calculated rest MBF, stress MBF, and MFR for the reference protocol as well as for the 14 selected protocols. We compared these three measurements for each of the 14 protocols to the reference protocol using the Wilcoxon signed rank test using SPSS Statistics version 24.0 (IBM Corporation). Following a Bonferroni correction for the 14 different comparisons, the level of statistical significance was set to  $0.05/14 = 0.004$  for all statistical analyses.

## RESULTS

We screened 112 articles finding 62 potentially relevant articles containing temporal sampling protocols, as shown in Figure 2. Upon additional review, this resulted in 15 different temporal sampling protocols that were applied to patient data, including the reference protocol referred by 26A, as shown in Table 1 and Figure 3. The baseline characteristics of the included patients are summarized in Table 2.

We found a good reproducibility for the reference protocol as the mean absolute relative differences were ≤4.1% as shown in Figure 4. Neither the MBF nor the MFR measurements differed significantly after Bonferroni correction ( $p > 0.01$ ), as shown in Figure 5.

Six out of the 14 (43%) temporal sampling protocols resulted in different global rest and stress MBF ( $p \leq 0.003$ ) as compared to the reference protocol. The corresponding protocols were those with 22, 27 (A), 30, 31, 32, and 48 frames as shown in Table 3 and Figure 5. Significant differences in MBF were found for these six protocols which all use time frames <90 seconds in the tissue phase instead of 120 seconds as used in the reference protocol. Compared to the reference, none of the tested protocols showed a difference ( $p \geq 0.15$ ) in global MFR measurements. Median values with interquartile ranges of the MBF and MFR measurements for all 20 patients obtained using the different temporal sampling protocols and the mean absolute relative differences to the reference protocol with ranges are given in Table 3.

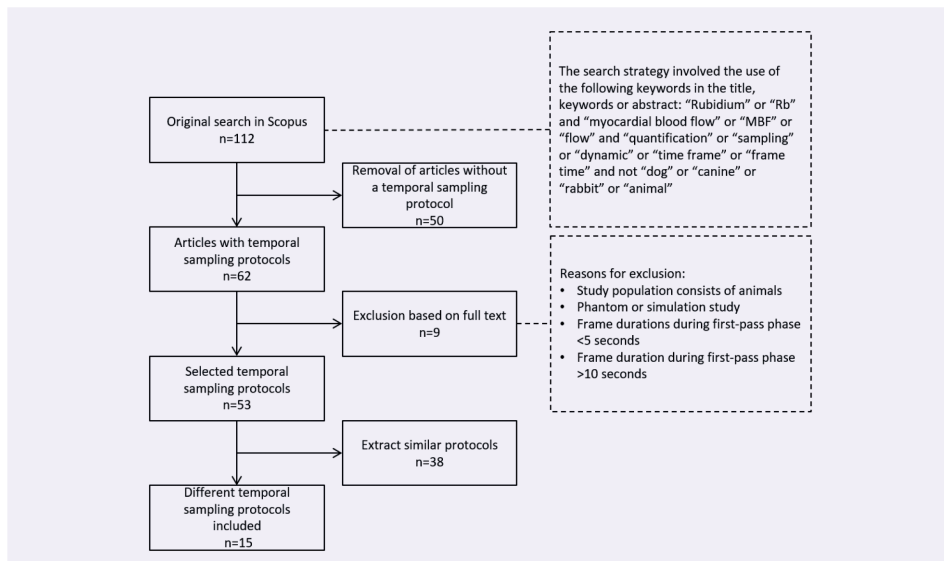


Figure 2. Flow chart of temporal sampling protocol selection. The full texts of all the articles that were found were screened for temporal sampling protocols used for Rb-82 PET MPI.

Table 1. Overview of the 14 tested temporal sampling protocols and the reference protocol (26A) that was post-processed twice (26A\*).

Number of frames	Frame lengths				
14	9 x 10 seconds	3 x 30 seconds	1 x 60 seconds	1 x 120 seconds	
16	12 x 10 seconds	2 x 30 seconds	1 x 60 seconds	1 x 120 seconds	
18	1 x 10 seconds	8 x 5 seconds	3 x 10 seconds	2 x 20 seconds	4 x 60 seconds
20	12 x 8 seconds	5 x 12 seconds	1 x 30 seconds	1 x 60 seconds	1 x 120 seconds
22	18 x 10 seconds	4 x 60 seconds			
23	15 x 6 seconds	5 x 12 seconds	1 x 30 seconds	1 x 60 seconds	1 x 120 seconds
26A & 26A*	24 x 5 seconds	2 x 120 seconds			
26B	12 x 5 seconds	6 x 10 seconds	4 x 20 seconds	4 x 40 seconds	
26C	18 x 5 seconds	6 x 15 seconds	1 x 120 seconds	1 x 60 seconds	
27A	20 x 6 seconds	4 x 30 seconds	3 x 60 seconds		
27B	14 x 5 seconds	6 x 10 seconds	3 x 20 seconds	3 x 30 seconds	1 x 90 seconds
30	16 x 5 seconds	6 x 10 seconds	3 x 20 seconds	4 x 30 seconds	1 x 80 seconds
31	20 x 6 seconds	5 x 12 seconds	4 x 30 seconds	2 x 60 seconds	
32	24 x 5 seconds	8 x 30 seconds			
48	36 x 5 seconds	8 x 15 seconds	4 x 30 seconds		



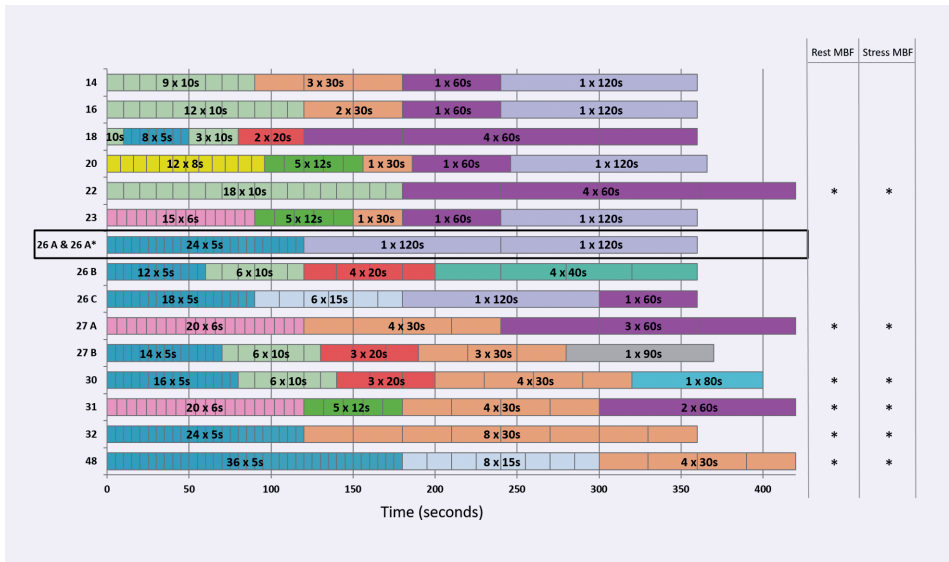


Figure 3. Temporal sampling protocols that were tested and compared to the reference protocol (26A) (in the black box) that was post-processed twice (26A\*). The number of frames of each protocol is shown on the y-axis and the time in seconds on the x-axis. Every frame has a color representing the duration of that frame, for example, yellow represents 8-second time frames and pink represents 60-second time frames. Significant differences in global rest or stress MBF (mL/ min/g) values compared to the reference protocol are indicated on the second y-axis (\* $p < 0.004$ ). No significant differences in global MFR were found.

Absolute relative differences in both rest and stress MBF were  $\leq 10\%$  in all patients for protocols using 26 (B) and 27 (B) frames with mean absolute relative differences up to 4% as shown in Table 3 and Figure 4. In addition, protocols using 20, 23, 26 (C), and 30 frames showed absolute relative differences of  $\leq 10\%$  for just rest or stress MBF.

On a regional level, both rest and stress MBF differed ( $p \leq 0.002$ ) in all regional territories (LAD, LCX, and RCA) for the protocols using 22, 27 (A), 31, 32, and 48 frames. Median values with interquartile ranges of regional MBF and MFR values obtained using the different temporal sampling protocols and the mean absolute relative differences to the reference protocol with ranges are given in the appendix which is available online. Results on a regional level were in agreement with the results found for global rest and stress MBF. Compared to the reference, none of the tested protocols showed a significant difference ( $p \geq 0.11$ ) in regional MFR measurements.

## DISCUSSION

In this study, we selected temporal sampling protocols used in Rb-82 PET MPI from the literature and assessed the effect on absolute blood flow measurements. We showed that the use of various temporal sampling protocols can result in different rest and stress MBF, both on a regional and global level. We found mean absolute relative differences up to 13% for global MBF and up to 16% for regional MBF in comparison to the reference protocol. No significant differences were found for global or regional MFR.

Several studies have reported the importance of accurate temporal sampling of the first-pass phase for MBF quantification<sup>3, 8-10</sup>. The temporal sampling protocol that we used as reference was stated by Lee et al. to optimally sample the blood pool TAC<sup>10</sup>. This protocol uses 24 5-second frames for the first-pass and intermediate (activity in both LV and myocardium) phase. Furthermore, the protocol uses 2 frames of 120 seconds for the tissue phase (activity mainly present in the myocardium) as it was shown that such long frame durations hardly affect MBF measurements<sup>10</sup>. In our study, differences in MBF were most frequently found for the protocols with time frames less than 90 seconds in the tissue phase instead of 120 seconds as used in the reference protocol. More specifically, it seems that small variations in the input function alter MBF measurements, presumably due to insufficient count statistics during the tissue phase. Yet the protocol with 18 frames was the only protocol that uses time frames less than 90 seconds for which we did not find a significant difference in MBF. As we found a good reproducibility for the reference protocol, it is unlikely that the manual relocation of the ROI or the myocardial contours caused the differences in MBF measurements. Possibly, deviating MBFs might partly be explained by time frames which are too small or too large in the intermediate phase in combination with shorter time frames in the tissue phase. The effect of time framing during the first-pass phase was expected to be limited as we only used frames of 5-10 seconds in this phase<sup>10</sup>.

Table 2. Baseline characteristics of all included patients.

Characteristic	All patients (N=20)
Age (years)	67 ± 9
Male gender (%)	80
Weight (kg)	87 ± 15
Height (cm)	177 ± 8
BMI (kg/m <sup>2</sup> )	27.7 ± 4.3
Current smoker (%)	5
Hypertension (%)	45
Diabetes (%)	30
Dyslipidemia (%)	40
Family history (%)	55

*Data are presented as mean ± SD or as percentage*

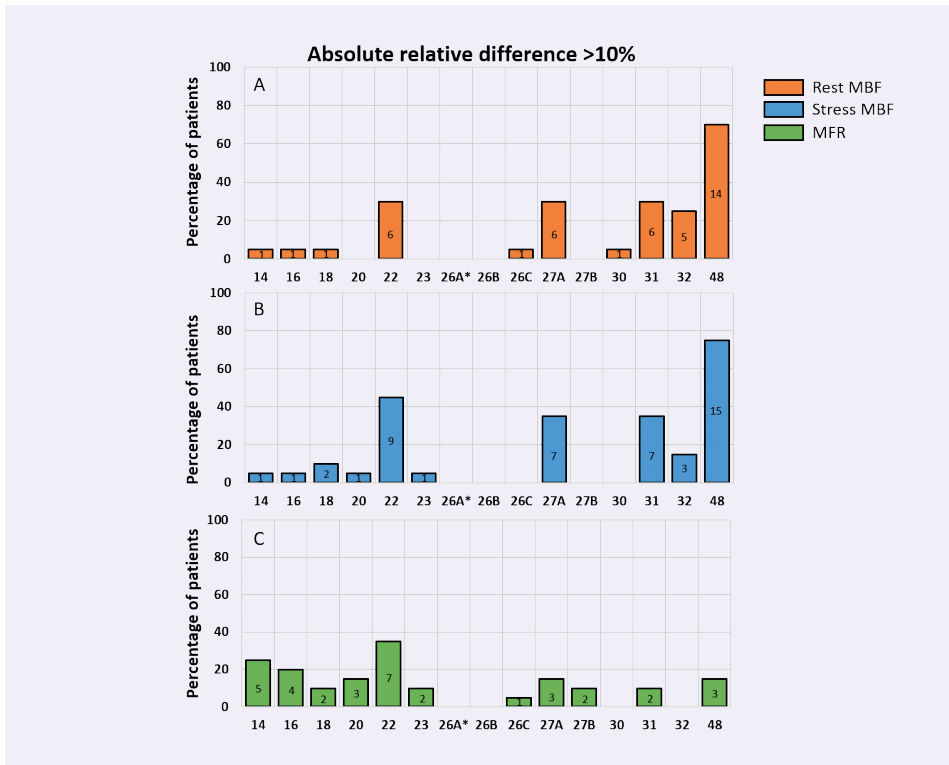


Figure 4. Barplot showing the percentage of patients with absolute relative differences >10% in A global rest MBF (mL/min/g), B global stress MBF (mL/min/g), and C global MFR for all tested protocols as compared to the reference protocol that was post-processed twice (26A\*). The absolute number of patients is shown within the bars.

Compared to the reference, none of the tested protocols showed a significant difference in global or regional MFR measurements. As the MFR is the ratio between stress and rest MBF, it seems to correct for systemic biases of rest and stress MBF introduced by several temporal sampling protocols (Figure 5). However, as MFR is defined as the ratio between stress and rest MBF, error propagation might cause the variance of MFR measurements to exceed the variance of MBF measurements<sup>14</sup>. This likely explains that for some protocols (14, 16, and 20), we observed more patients with an absolute relative difference >10% for MFR than for rest or stress MBF (Figure 4). Furthermore, conflicting studies exist regarding the preference for stress MBF or MFR for risk stratification of patients with suspected CAD. Several studies found that stress MBF is superior to MFR,<sup>15-17</sup> while others found that the MFR is superior to stress MBF for risk stratification<sup>1, 3-5, 18</sup>. Murthy et al.<sup>19</sup> and Tahari et al.<sup>20</sup> reported that MFR was more consistent when different software is used and when different methods are used to determine the input function. Moreover, MFR was shown to be more robust in case of different advanced reconstruction settings as compared to MBF values<sup>21</sup>. In our study, MFR measurements were clearly less dependent on the temporal sampling protocol as compared to MBF measurements, which supports MFR as the preferred parameter.

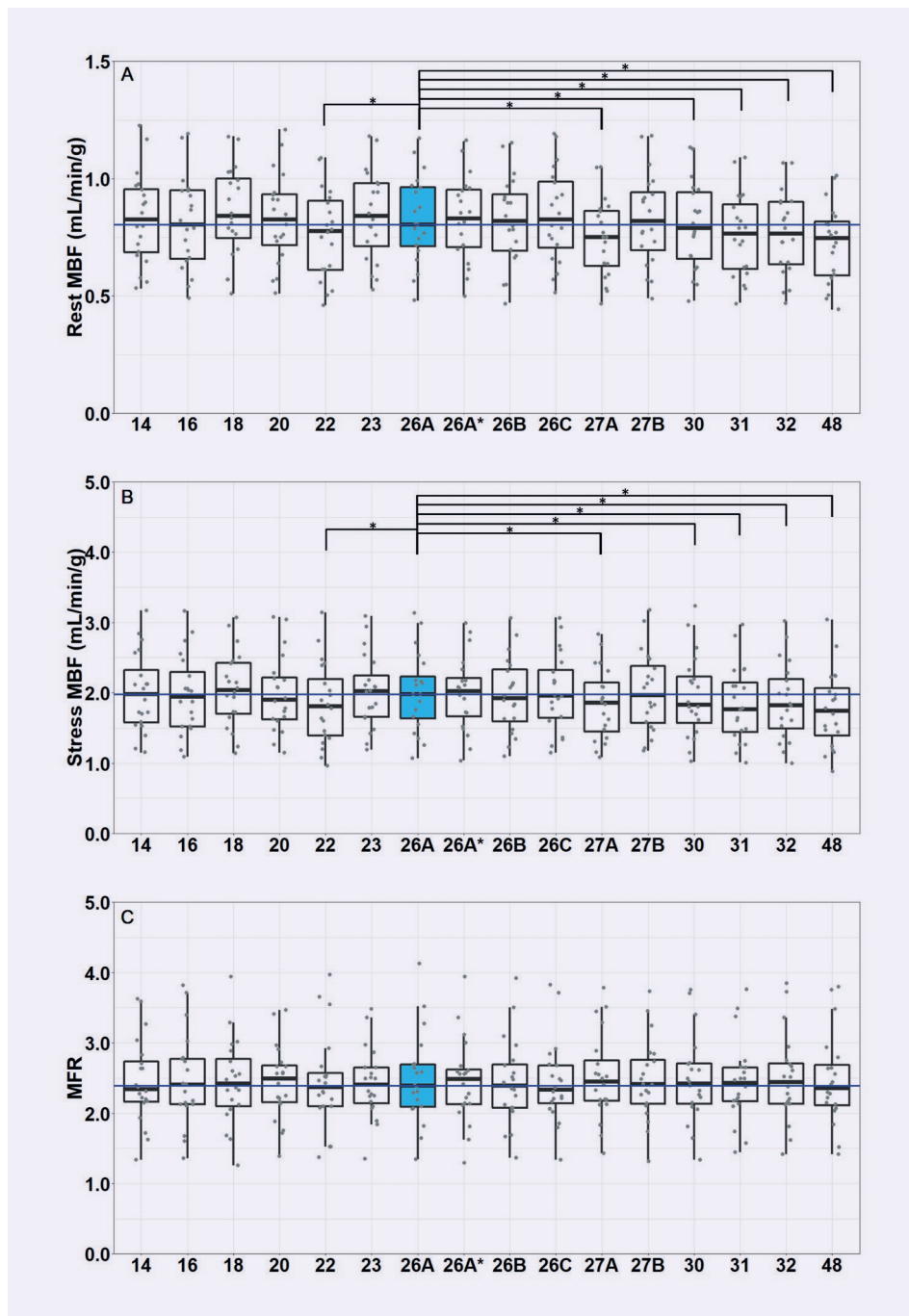


Figure 5. Boxplots of the 14 tested temporal sampling protocols and the boxplot showing the reproducibility (26A\*) with the MBF and MFR values of each patient (gray dots) and the median value (dark blue line) representing the reference protocol (26A, blue) for global rest (A) and stress (B) MBF and MFR (C). \* $p < 0.004$ .

**Table 3.** Global flow values and mean absolute relative differences for all 14 protocols in comparison to the reference protocol that was post-processed twice (26A and 26A\*).

Number of frames	Global					
	Flow values			Mean absolute relative difference		
	Stress MBF (mL/min/g)	Rest MBF (mL/min/g)	MFR	Stress MBF (%)	Rest MBF (%)	MFR (%)
14	1.98 [1.55–2.49]	0.83 [0.68–0.97]	2.34 [2.15–2.80]	4.9 (1–13)	3.7 (0–11)	6.8 (0–16)
16	1.95 [1.52–2.41]	0.81 [0.65–0.95]	2.40 [2.13–2.78]	4.2 (1–14)	4.1 (0–11)	6.5 (1–17)
18	2.04 [1.67–2.44]	0.84 [0.72–1.02]	2.42 [2.07–2.85]	4.0 (0–15)	5.1 (0–15)	6.2 (1–15)
20	1.90 [1.61–2.26]	0.83 [0.69–0.94]	2.49 [2.14–2.71]	3.9 (0–12)	3.6 (0–10)	4.8 (0–17)
22	1.81 [1.37–2.33]*	0.78 [0.61–0.92]*	2.37 [2.10–2.63]	9.7 (0–20)	8.0 (1–19)	7.2 (0–18)
23	2.03 [1.65–2.37]	0.84 [0.68–0.98]	2.40 [2.11–2.65]	3.3 (0–11)	3.6 (0–10)	5.5 (1–19)
26A	1.98 [1.58–2.36]	0.81 [0.70–0.97]	2.39 [2.07–2.70]	Ref	Ref	Ref
26A*	2.02 [1.57–2.29]	0.83 [0.70–0.96]	2.48 [2.11–2.65]	3.3 (1–5)	2.1 (0–5)	3.0 (0–9)
26B	1.93 [1.52–2.37]	0.82 [0.68–0.96]	2.39 [2.08–2.73]	3.2 (0–8)	2.8 (0–7)	3.3 (0–10)
26C	1.96 [1.62–2.40]	0.83 [0.68–1.00]	2.33 [2.09–2.69]	3.1 (0–7)	2.7 (0–13)	3.7 (0–13)
27A	1.86 [1.39–2.26]*	0.75 [0.60–0.87]*	2.45 [2.14–2.84]	8.2 (1–18)	9.3 (1–34)	7.0 (0–36)
27B	1.97 [1.54–2.45]	0.82 [0.67–0.97]	2.41 [2.11–2.81]	3.9 (0–10)	3.0 (0–6)	4.7 (0–14)
30	1.83 [1.48–2.29]*	0.79 [0.63–0.95]*	2.42 [2.11–2.71]	4.2 (0–9)	3.8 (0–12)	3.3 (0–9)
31	1.77 [1.42–2.26]*	0.77 [0.61–0.91]*	2.42 [2.14–2.65]	9.0 (2–17)	8.0 (2–16)	5.7 (0–15)
32	1.83 [1.43–2.25]*	0.77 [0.63–0.77]*	2.44 [2.13–2.73]	7.2 (1–14)	7.6 (1–14)	4.1 (0–10)
48	1.74 [1.29–2.17]*	0.75 [0.58–0.83]*	2.35 [2.08–2.76]	13.2 (3–23)	12.7 (5–20)	5.9 (0–16)

Data are presented as median [interquartile range] and mean absolute relative difference (minimum–maximum). Significant differences in MBF and MFR measurements as compared to the reference protocol are indicated with \* ( $p < 0.004$ ). MBF, myocardial blood flow; MFR, myocardial flow reserve.

There are several limitations to this study that should be recognized. First, it was not possible to evaluate the effect of different temporal sampling protocols on the diagnostic accuracy due to the lack of a reference standard and the relatively small sample size. However, we did use an optimized temporal sampling protocol suggested by Lee et al. as a reference<sup>10</sup> and performed a pair-wise comparison, limiting the need for a large sample size.

Secondly, we used a relatively low Rb-82 activity (740 MBq) as compared to the generally recommended activity of 1110 MBq<sup>3</sup>. This relatively low amount of activity is sufficient for MBF quantification using the Vereos PET scanner which contains sensitive silicon photomultipliers with digital readout<sup>22, 23</sup>. Higher activities than 740 MBq will presumably result in better count statistics during the tissue phase and could therefore result in a better image quality. However, higher activities may hamper blood flow quantification when using PET scanners with photomultiplier tubes that have a low count-rate performance<sup>22, 24</sup>. If the activities administered exceed the dynamic range of the PET scanner, it will

lead to an underestimation of the count-rate during the first-pass phase which will influence the TAC<sup>10, 22, 24</sup> and therefore alter flow measurements. Nevertheless, if we had used a higher activity in all our patients, the count statistics during the tissue phase would be better which would possibly result in less MBF variation when using protocols with shorter time frames in the tissue phase as compared to the reference protocol. However, as previous studies showed that there is no added value in using shorter time frames during the tissue phase, we do not recommend these protocols<sup>10</sup>.

Finally, we tested temporal sampling protocols only using the 1-TCM of Lortie et al.<sup>13</sup> as this model is most commonly used for Rb-82. Therefore, we did not include other 1-TCMs with different extraction functions<sup>25</sup> or other compartmental models such as the two-compartment model<sup>26</sup> and the retention model<sup>27, 28</sup>. The retention model is a simpler model as compared to the 1-TCM<sup>27, 29</sup> as it “does not use TACs, but instead integrates arterial input and myocardial uptake over the first 2 and the following 5 minutes, respectively, after tracer injection”<sup>30</sup>. It was already shown that the use of the retention model resulted in differences in stress MBF when compared to the 1-TCM in combination with the ROI methodology and therefore the two models cannot be used interchangeably<sup>19, 20</sup>.

## **NEW KNOWLEDGE GAINED**

This manuscript provides new insights and has several clinical consequences. First, one should be cautious in using different temporal sampling protocols in PET imaging as we found significant differences for rest and stress MBF measurements in the myocardium as a whole but also on a regional level. It seems that MFR is less dependent on temporal sampling (this study) and also on other technical variations<sup>19-21</sup>. Therefore, MFR seems to be a more suitable parameter to be used between centers and for multicentre trials. To use rest and stress MBF among multiple sites in the detection of CAD and in multicentre trials, harmonization of all technical aspects such as temporal sampling is necessary.

## **CONCLUSIONS**

Various temporal sampling protocols for MBF and MFR quantification using Rb-82 PET result in different MBF values. MFR measurements were more robust to different temporal sampling protocols. Hence, we recommend using MFR instead of MBF measurements, especially when employed at different centers and in multicenter trials.

## REFERENCES

1. Ziadi MC, deKemp RA, Williams KA, Guo A, Chow BJ, Renaud JM et al (2011) Impaired myocardial flow reserve on rubidium-82 positron emission tomography imaging predicts adverse outcomes in patients assessed for myocardial ischemia. *Cardiac Imaging* 58:740-48.
2. Sciagra R, Passeri A, Bucerius J, Verberne HJ, Slart OL, Riemer HJA, Lindner O et al (2016) Clinical use of quantitative cardiac perfusion PET: Rationale, modalities and possible indications. Position paper of the cardiovascular committee of the European association of nuclear medicine (EANM). *Eur J Nucl Med Mol Imaging* 43:1530-45.
3. Murthy V, Bateman T, Beanlands R, Berman D, Borges-Neto S, Chareonthaitawee P et al (2018) Clinical quantification of myocardial blood flow using PET: Joint position paper of the SNMMI cardiovascular council and the ASNC. *J Nucl Cardiol* 25:269-97.
4. Murthy VL, Naya M, Foster CR, Hainer J, Gaber M, Di Carli G et al (2011) Improved cardiac risk assessment with noninvasive measures of coronary flow reserve. *Circulation* 124:2215-24.
5. Patel KK, Spertus JA, Chan PS, Sperry BW, Al Badarin F, Kennedy KF et al (2020) Myocardial blood flow reserve assessed by positron emission tomography myocardial perfusion imaging identifies patients with a survival benefit from early revascularization. *Eur Heart J* 41:759-68.
6. Klein R, Ocneanu A, deKemp R (2017) Time-frame sampling for 82Rb PET flow quantification: Towards standardization of clinical protocols. *J Nucl Cardiol* 24:1530-34.
7. Sciagrà R, Lubberink M, Hyafil F, Saraste A, Slart OL, Riemer HJA, Agostini D et al (2020) EANM procedural guidelines for PET/CT quantitative myocardial perfusion imaging. *Eur J Nucl Med Mol Imaging*. <https://doi.org/10.1007/s00259-020-05046-9>.
8. Klein R, Beanlands R, deKemp R (2010) Quantification of myocardial blood flow and flow reserve: Technical aspects. *J Nucl Cardiol* 17:555-70.
9. Moody J, Lee B, Corbett J, Ficaro E, Murthy V (2015) Precision and accuracy of clinical quantification of myocardial blood flow by dynamic PET: A technical perspective. *J Nucl Cardiol* 22:935-51.
10. Lee B, Moody J, Weinberg R, Corbett J, Ficaro E, Murthy V (2017) Optimization of temporal sampling for 82rubidium PET myocardial blood flow quantification. *J Nucl Cardiol* 24:1517-29.
11. Koenders SS, van Dijk JD, Jager PL, Ottervanger JP, Slump CH, van Dalen JA (2019) How to detect and correct myocardial creep in myocardial perfusion imaging using rubidium-82 PET? *J Nucl Cardiol* 26:729-34.
12. Koenders SS, van Dijk JD, Jager PL, Ottervanger JP, Slump CH, van Dalen JA (2019) Impact of regadenoson-induced myocardial creep on dynamic rubidium-82 PET myocardial blood flow quantification. *J Nucl Cardiol* 26:719-28.
13. Lortie M, Beanlands R, Yoshinaga K, Klein R, DaSilva J, deKemp R (2007) Quantification of myocardial blood flow with 82Rb dynamic PET imaging. *Eur J Nucl Med Mol Imaging* 34:1765-74.
14. Moody JB, Murthy VL, Lee BC, Corbett JR, Ficaro EP (2015) Variance estimation for myocardial blood flow by dynamic PET. *IEEE Trans Med Imaging* 34:2343-53.

15. Farhad H, Dunet V, Bachelard K, Allenbach G, Kaufmann PA, Prior JO (2013) Added prognostic value of myocardial blood flow quantitation in rubidium-82 positron emission tomography imaging. *Eur Heart J Cardiovasc Imaging* 14:1203-10.
16. Danad I, Uusitalo V, Kero T, Saraste A, Rajmakers PG, Lammertsma AA et al (2014) Quantitative assessment of myocardial perfusion in the detection of significant coronary artery disease cutoff values and diagnostic accuracy of quantitative [O-15]H<sub>2</sub>O PET imaging. *J Am Coll Cardiol* 64:1464-75.
17. Hajjiri MM, Leavitt MB, Zheng H, Spooner AE, Fischman AJ, Gewirtz H (2009) Comparison of positron emission tomography measurement of adenosine-stimulated absolute myocardial blood flow versus relative myocardial tracer content for physiological assessment of coronary artery stenosis severity and location. *JACC Cardiovasc Imaging* 2:751-58.
18. Gupta A, Taqueti VR, van de Hoef TP, Tim P, Bajaj NS, Bravo PE, Murthy VL et al (2017) Integrated noninvasive physiological assessment of coronary circulatory function and impact on cardiovascular mortality in patients with stable coronary artery disease. *Circulation* 136:2325-36.
19. Murthy VL, Lee BC, Sitek A, Naya M, Moody J, Polavarapu V et al (2014) Comparison and prognostic validation of multiple methods of quantification of myocardial blood flow with 82Rb PET. *J Nucl Med* 55:1952-58.
20. Tahari AK, Lee A, Rajaram M, Fukushima K, Lodge MA, Lee BC et al (2014) Absolute myocardial flow quantification with (82)rb PET/CT: Comparison of different software packages and methods. *Eur J Nucl Med Mol Imaging* 41:126-35.
21. Armstrong I, Tonge C, Arumugam P (2014) Impact of point spread function modeling and time-of-flight on myocardial blood flow and myocardial flow reserve measurements for rubidium-82 cardiac PET. *J Nucl Cardiol* 21:467-74.
22. van Dijk J, Jager P, van Osch J, Khodaverdi M, van Dalen J (2019) Comparison of maximal rubidium-82 activities for myocardial blood flow quantification between digital and conventional PET systems. *J Nucl Cardiol* 26:1286-91.
23. Hoff CM, Sørensen J, Christensen NL, Bouchelouche K, Tolbod L (2020) Activity regimes for 82Rb cardiac PET: Effects on absolute MBF and MPI. *J Nucl Cardiol*. <https://doi.org/10.1007/s12350-020-02266-2>.
24. Renaud JM, Yip K, Guimond J, Trottier M, Pibarot P, Turcotte E et al (2017) Characterization of 3-dimensional PET systems for accurate quantification of myocardial blood flow. *J Nucl Med* 58:103-09.
25. Prior JO, Allenbach G, Valenta I, Kosinski M, Burger C, Verdun FR et al (2012) Quantification of myocardial blood flow with 82 rb positron emission tomography: Clinical validation with 15 O-water. *Eur J Nucl Med Mol Imaging* 39:1037-47.
26. Herrero P, Markham J, Shelton ME, Bergmann SR (1992) Implementation and evaluation of a two-compartment model for quantification of myocardial perfusion with rubidium-82 and positron emission tomography. *Circ Res* 70:496-07.
27. Yoshida K, Mullani N, Gould KL (1996) Coronary flow and flow reserve by PET simplified for clinical applications using rubidium-82 or nitrogen-13-ammonia. *J Nucl Med* 37:1701-12.



28. Herrero P, Markham J, Shelton ME, Weinheimer CJ, Bergmann SR (1990) Noninvasive quantification of regional myocardial perfusion with rubidium-82 and positron emission tomography. Exploration of a mathematical model. *Circulation* 82:1377-86.
29. Yoshinaga K, Klein R, Tamaki N (2010) Generator-produced rubidium-82 positron emission tomography myocardial perfusion imaging—From basic aspects to clinical applications. *J Cardiol* 55:163-73.
30. Johnson NP, Gould KL (2015) Regadenoson versus dipyridamole hyperemia for cardiac PET imaging. *JACC Cardiovasc Imaging* 8:438-47.



IMPACT OF

# REGADENOSON-INDUCED MYOCARDIAL CREEP ON DYNAMIC RUBIDIUM-82 PET MYOCARDIAL BLOOD FLOW QUANTIFICATION

## Authors

S. S. Koenders<sup>1,2</sup>

J. D. van Dijk<sup>1</sup>

P. L. Jager<sup>1</sup>

J. P. Ottervanger<sup>3</sup>

C. H. Slump<sup>2</sup>

J. A. van Dalen<sup>4</sup>

## Author Affiliations

1. Department of Nuclear Medicine, Isala Hospital, Zwolle, The Netherlands
2. Technical Medical Centre, University of Twente, Enschede, the Netherlands
3. Department of Cardiology, Isala Hospital, Zwolle, The Netherlands
4. Department of Medical Physics, Isala Hospital, Zwolle, The Netherlands

## Published in

Journal of Nuclear Cardiology 2019;26:719-28



## ABSTRACT

### Background

Repositioning of the heart during myocardial perfusion imaging (MPI) using Rubidium-82 (Rb-82) PET may occur when using regadenoson. Our aim was to determine the prevalence and the effect of correcting for this myocardial creep on myocardial blood flow (MBF) quantification.

### Methods

We retrospectively included 119 consecutive patients who underwent dynamic rest- and regadenoson-induced stress MPI using Rb-82 PET. The presence of myocardial creep was visually assessed in the dynamic stress PET series by identifying differences between the automatically drawn myocardium contour and the activity. Uncorrected and corrected stress MBFs were compared for the three vascular territories (LAD, LCX, and RCA) and for the whole myocardium.

### Results

Myocardial creep was observed in 52% of the patients during stress. Mean MBF values decreased after correction in the RCA from 4.0 to 2.7 mL/min/g ( $p < 0.001$ ), in the whole myocardium from 2.7 to 2.6 mL/min/g ( $p = 0.01$ ), and increased in the LAD from 2.5 to 2.6 mL/min/g ( $p = 0.03$ ) and remained comparable in the LCX ( $p = 0.3$ ).

### Conclusions

Myocardial creep is a frequent phenomenon when performing regadenoson-induced stress Rb-82 PET and has a significant impact on MBF values, especially in the RCA territory. As this may hamper diagnostic accuracy, myocardial creep correction seems necessary for reliable quantification.

### Keywords

Myocardial blood flow; PET myocardial perfusion imaging; Rb-82; Myocardial creep; Regadenoson.

## INTRODUCTION

The use of myocardial blood flow (MBF) quantification using Rubidium-82 (Rb-82) in myocardial perfusion imaging (MPI) with positron emission tomography (PET) is increasing rapidly<sup>1-3</sup>. MPI using Rb-82 PET is of added value in the diagnosis of coronary artery disease, and the MBF quantification provides valuable additional prognostic information about the extent and functional importance of possible stenosis<sup>4-6</sup>.

A dynamic PET acquisition including the capture of the first-pass bolus of the activity is required for MBF quantification. Pharmacological vasodilators are generally used to induce stress, while the patient is lying inside the PET scanner<sup>1,7</sup>. The three commonly used vasodilators are adenosine, dipyridamole, and regadenoson. Due to the stimulation of A1, A2B, and A3 receptors, adenosine and dipyridamole are associated with undesirable short-term side-effects as general discomfort, chest pain, and hypotension, and more severe side-effects such as atrioventricular block or bronchospasm<sup>8,9</sup>. An alternative is regadenoson which is a more selective vasodilator that only stimulates A2A receptors and is fast and better tolerated by patients<sup>10-15</sup>. Regadenoson has shown to result in accurate calculation of quantitative MBF values in MPI using Rb-82 PET with similar accuracy compared to adenosine or dipyridamole<sup>10,12,16-18</sup>. An additional advantage of regadenoson is the significantly lower degree of patient motion compared to adenosine, which can significantly affect the MBF quantification<sup>19-23</sup>.

Despite the reduced patient motion when using regadenoson, in clinical practice, we frequently observe repositioning of the heart after administration of regadenoson. This so-called myocardial creep is presumably caused by an increasing respiration and lung volume and thereby the repositioning of the diaphragm and heart after induction of pharmacological stress<sup>24</sup>. This motion may result in biased MBF measurements and may hamper diagnostic accuracy. Our aim was to determine the percentage of patients with this myocardial creep and to determine its effect on MBF values before and after correction in patients undergoing Rb-82 PET.

## METHODS

### Study design

We retrospectively included 119 consecutive patients referred for MPI using Rb-82 PET/CT (GE Discovery 690, GE Healthcare), who underwent dynamic rest- and pharmacological-induced stress using regadenoson. This study was retrospective and approval by the medical ethics committee was therefore not required according to Dutch law. Nevertheless, all patients provided written informed consent for the use of data for research purposes.

### Patient preparation and data acquisition

All subjects were asked to abstain from caffeine-containing substances for 24 hours and to discontinue dipyridamole-containing medication for 48 hours before imaging. Prior to MPI, a low-dose CT scan was

acquired during free-breathing to provide an attenuation map of the chest. This scan was made using a 5-mm slice thickness, 0.8 s rotation time, pitch of 0.97, collimation of 32x0.625 mm, tube voltage of 120 kV, and a tube current of 10 mA. Next, 740 MBq Rb-82 was administered intravenously with a flow rate of 50 mL/min using a Sr-82/Rb-82 generator (CardioGen-82, Bracco Diagnostics Inc.). After the first elution, we induced pharmacological stress by administering 400 µg (5 L) of regadenoson over 10 seconds. After a 5 mL saline flush (NaCl 0.9%), we administered a second dose of 740 MBq Rb-82. We acquired seven-minute PET list-mode acquisitions after both Rb-82 administrations. Attenuation correction was applied to all data on the PET system after semiautomatic registration of CT and PET data. We reconstructed the dynamic datasets using 26 time frames (12x5s, 6x10s, 4x20s and 4x40s) with default settings as recommended by the manufacturer using 3D iterative reconstruction using 2 iterations and 24 subsets, while correcting for decay, attenuation, scatter and random coincidences, and dead time effects. Neither time-of-flight information, nor a post-processing filter or resolution modeling was used. Static images were reconstructed from 2:30 to 7:00 minutes for both rest and stress scans.

### Data processing

The reconstructed dynamic images were processed using Corridor4DM software (v2015.02.64). Myocardium contours were automatically detected in both rest and stress scans based on the static images. Furthermore, a region of interest (ROI) was manually placed at the location of the mitral valve to estimate the activity in the blood pool. The activity concentrations in the myocardium contour and ROI were measured in the 26 reconstructed time frames to calculate the time activity curves (TACs) for the left ventricle (LV), for the three vascular territories: left anterior descending (LAD), left circumflex (LCX) and right coronary (RCA) artery, and for the whole myocardium. The one-tissue compartment model of Lortie et al. based on a ROI methodology was used to calculate the MBF from the TACs using Corridor4DM<sup>25</sup>.

The activity in the myocardium was visually compared with the drawn contours in all individual time frames to detect possible patient motion or myocardial creep. Myocardial creep was defined as gradual decreasing misalignment of the drawn myocardium contour with the activity present in the ventricle and/or myocardium, primarily in the inferior direction. This misalignment was at least one third of the width of the left ventricular myocardial wall and present in at least two time frames of which one had to include the first-pass phase: the filling of the LV. If myocardial creep was present, manual realignment of the contour to the activity in the myocardium was applied in each of the related time frames. Motion not fulfilling the requirements of myocardial creep, suggesting general patient motion, was manually corrected by realigning the myocardium contour to the activity. Patients were excluded when patient motion was present together with myocardial creep to prevent biased results due to overlapping motion. Furthermore, patients with an unreliable TAC were also excluded. Unreliable TACs were defined as TACs showing no clear LV peak<sup>26</sup>.

To evaluate the influence of myocardial creep correction, both rest and stress MBFs were calculated for the original data and for the corrected data regarding the three vascular territories (LAD, LCX, and RCA) and for the whole myocardium. Furthermore, the myocardial flow reserve (MFR), defined as the stress MBF divided by the rest MBF was calculated as well. A difference in MBF or MFR >10% between the corrected and uncorrected scans was considered to possibly influence diagnostic interpretation.

### Statistical analysis

Patient-specific parameters and characteristics were determined as percentage or mean  $\pm$  standard deviation (SD) and compared with Chi-square and t-tests as appropriate, using SPSS Statistics version 22.0 (IBM Corporation). The MBF and MFR of the uncorrected and corrected data were compared using the Wilcoxon signed rank test. The level of statistical significance was set to 0.05 for all statistical analyses.

## RESULTS

Of the 119 patients, 11 (9%) were excluded due to the presence of both patient motion and myocardial creep in the stress data. An additional four patients (3%) were excluded due to unreliable TACs. An example of an unreliable TAC is shown in Figure 1. Of the remaining 104 patients, four (3%) showed only general patient motion in stress.

The baseline characteristics of the remaining 104 patients are summarized in Table 1. 54 (52%) Patients showed a myocardial creep during the stress scan, as illustrated in Figure 2. Patients with and without myocardial creep did not differ regarding gender, weight, body mass index (BMI), cardiac risk factors and scan outcomes ( $p \geq 0.10$ ). Yet patients with myocardial creep were younger (64 years old) than patients without myocardial creep (70 years old,  $p=0.004$ ). Of the 54 patients with myocardial creep during stress, two patients also showed myocardial creep during the rest scan.

The uncorrected and corrected MBF and MFR measurements, in both rest and stress, for each of the three territorial segments and for the myocardium as a whole (global result) are shown in Table 2 and Figure 3. When comparing the uncorrected and corrected data, the largest differences were found for the RCA territory where the mean MBF decreased from 4.0 to 2.7 mL/min/g ( $p < 0.001$ ) and the mean MFR from 3.5 to 2.4 ( $p < 0.001$ ). Moreover, the MBF of the RCA decreased in 91% (49/54) of the patients, and the MFR of the RCA decreased in 89% (48/54) of the patients, as shown in Figure 3D. Furthermore, differences in MBF and MFR were found for the LAD territory and for the whole myocardium. The mean MBF increased for the LAD from 2.5 to 2.6 mL/min/g ( $p=0.03$ ) and for the MFR from 2.2 to 2.3 ( $p=0.006$ ), and for the whole myocardium, the mean MBF and MFR values decreased from 2.7 to 2.6 mL/min/g ( $p=0.01$ ) and from 2.4 to 2.3 ( $p=0.03$ ), respectively. No significant differences were found for the LCX territory in stress ( $p=0.3$ ) nor in the rest scans ( $p \geq 0.11$ ). In the 54 patients with myocardial creep, 45 (83%) had a change >10% in MBF and 45 (83%) had a change >10% in MFR in one of the territories or the whole myocardium.



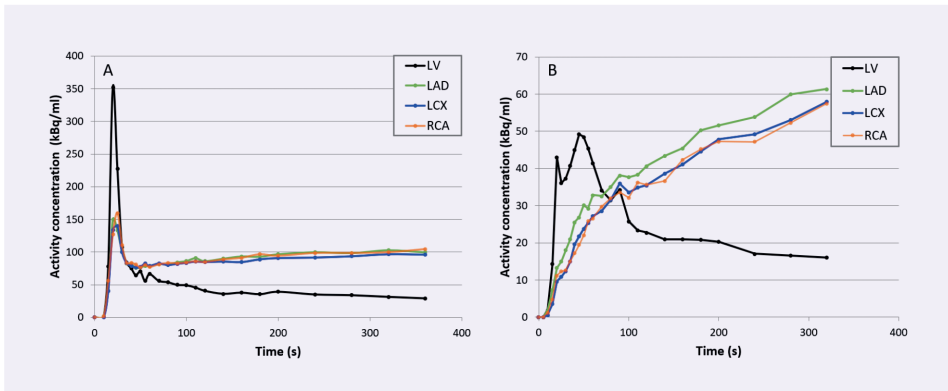
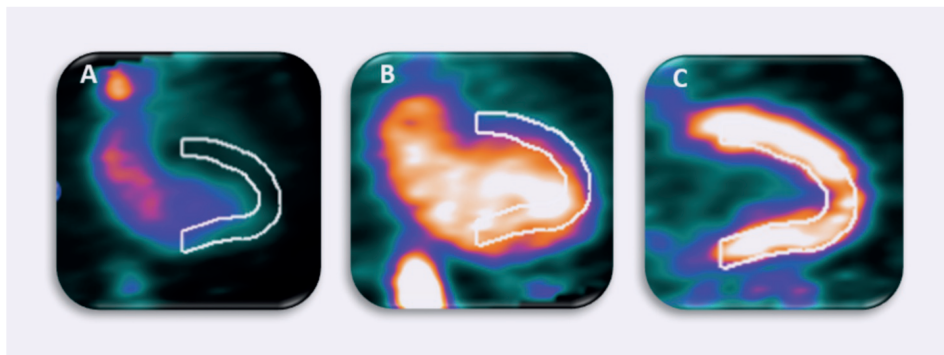


Figure 1. Linegraph showing (A) normal time activity curves (TACs) with a high peak value for the left ventricle (LV) during the first-pass phase and where the vascular territories (LAD, LCX and RCA) gradually reach a steady state and (B) unreliable TACs with no clear LV peak and lack of steady state for the three vascular territories.

Table 1. Baseline characteristics and scan outcomes of all included patients (N=104) who underwent clinically indicated Rb-82 PET MPI.

Characteristic	Patients with myocardial creep (N=54)	Patients without myocardial creep (N=50)	p values (t-test/ $\chi^2$ )
Age (years)	64 ± 11	70 ± 11	0.004
Male gender (%)	67	64	0.78
Weight (kg)	90 ± 15	85 ± 18	0.17
Height (cm)	175 ± 9	173 ± 10	0.32
BMI (kg/m <sup>2</sup> )	29.3 ± 4.1	28.5 ± 5.8	0.44
Current smoker (%)	30	16	0.10
Hypertension (%)	46	50	0.71
Diabetes (%)	17	20	0.66
Dyslipidemia (%)	56	50	0.57
Family history (%)	69	54	0.13
Normal MPI scan (%)	76	64	0.18
Ischemic defects on MPI (%)	17	28	0.29
Non-reversible defects on MPI (%)	9	16	0.61

Data are presented as mean ± SD or as percentage



**Figure 2.** Example of a dynamic Rb-82 PET scan showing myocardial creep. In A (15-19 s after injection), the activity reaches the left ventricle (LV) and a misalignment of the automatically drawn myocardium contour and the activity is observed. In B (25-29 s after injection), the activity has reached the LV and the myocardium but the misalignment of the drawn myocardium contour and the activity is still observed. In C (360-420 s after injection), activity is only present in the myocardium and the heart has returned to its original position resulting in alignment of the observed activity and myocardium contour.

**Table 2.** Uncorrected and corrected rest and stress MBF (mL/min/g) and MFR values for the three vascular territories (LAD, LCX, and RCA) and the whole myocardium (Global).

Vessel		Rest MBF	Stress MBF	MFR
LAD	Uncorr	1.2 ± 0.4 (0.5 to 2.7)	2.5 ± 0.9 (0.7 to 5.8)	2.2 ± 0.5 (1.2 to 3.4)
	Corr	1.2 ± 0.4 (0.5 to 2.7)	2.6 ± 0.9* (0.8 to 5.6)	2.3 ± 0.6** (1.4 to 3.8)
LCX	Uncorr	1.1 ± 0.4 (0.6 to 2.6)	2.5 ± 0.9 (0.8 to 4.8)	2.3 ± 0.7 (0.7 to 5.1)
	Corr	1.1 ± 0.4 (0.6 to 2.6)	2.5 ± 0.8 (0.7 to 5.4)	2.3 ± 0.6 (0.7 to 3.7)
RCA	Uncorr	1.2 ± 0.5 (0.6 to 2.7)	4.0 ± 2.3 (1.0 to 9.0)	3.5 ± 1.9 (0.8 to 11)
	Corre	1.2 ± 0.4 (0.6 to 2.7)	2.7 ± 1.1*** (0.8 to 7.4)	2.4 ± 0.8*** (0.9 to 5.2)
Global	Uncorr	1.2 ± 0.4 (0.6 to 2.7)	2.7 ± 1.0 (1.0 to 5.7)	2.4 ± 0.7 (1.1 to 5.6)
	Corr	1.1 ± 0.4 (0.6 to 2.7)	2.6 ± 0.9* (0.9 to 5.7)	2.3 ± 0.6* (1.1 to 4.1)

Data are presented as mean ± SD

LAD, left anterior descending; LCX, left circumflex; MBF, myocardial blood flow; MFR, myocardial flow reserve; RCA, right coronary artery

\* $p < 0.05$ ; \*\* $p < 0.01$ ; \*\*\* $p < 0.001$

## DISCUSSION

In this study, we have demonstrated that a myocardial creep occurs in more than half of the patients during regadenoson-induced stress MPI using Rb-82 PET. Moreover, correction of this myocardial creep resulted in significantly lower MBF and MFR values for the RCA territory and may improve diagnostic accuracy. Besides the large impact on MBF and MFR values in the RCA territory, myocardial creep also resulted in significant differences in stress MBF and MFR values for the LAD and the whole myocardium. These differences can be explained by the anatomic position and direction of myocardial creep, as illustrated in Figure 4. During the first-pass phase when the Rb-82 activity is in the LV, there is a strong overlap between the activity and the part of the myocardium contour that is perfused by the RCA and to a lesser extent by the LAD when myocardial creep is present. After correction, the overlap diminishes, which directly affects the MBF and MFR measurements.

Multiple studies have reported the occurrence of myocardial creep, also known as non-returning motion of the heart, primarily occurring in the post-stress period during MPI using different pharmacological vasodilators<sup>19, 23, 24, 27, 28</sup>. A recent study by Memmot et al. reported a non-returning motion or myocardial creep in 36% (11/30) of their patients during MPI using Rb-82 PET and regadenoson as vasodilator independent of age<sup>19</sup>. This percentage is in fair agreement with the 52% found in this study, although we used a different methodology to assess the presence of myocardial creep and a slightly different time-framing combination. Furthermore, they showed that 69% (11/16) of the patients stressed with regadenoson with visible motion were categorized as myocardial creep which is in fair agreement to the 78% (54/69) found in our study. Moreover, they reported that only 10% (3/30) of their patients showed significant motion, which was defined as motion greater than half the width of the myocardial wall. Although we did not assess severity or amount of myocardial creep, we did observe that correcting for myocardial creep majorly affected the MBF quantification in most patients and presumably also in patients with only a limited amount of myocardial creep. Lee et al. recently reported that greater motion was observed during stress, especially in the inferior direction which reflects myocardial creep which is in high agreement with our study<sup>28</sup>. They also reported that motion resulted in the largest changes in the MBF and MFR in the RCA territory, consistent with our results.

Multiple mechanisms are hypothesized in the literature to explain the occurrence of myocardial creep. Karacalioglu et al. hypothesized that myocardial creep is caused by gravity on the organs when patients switch from a standing to a lying position in the scanner<sup>29</sup>. They reported that a five-minute bed rest on the scanner table significantly decreased the vertical motion of the heart<sup>29</sup>. A CT-scan followed by the rest scan was performed before the stress scan in our protocol. Therefore, the mechanism described above does not explain the myocardial creep we found during stress imaging. Although this gravity theory might explain myocardial creep during rest acquisitions, we observed myocardial creep in only 2% of the rest scans and therefore think this is most likely caused by anxiety at the start of a MPI scan<sup>30</sup>.

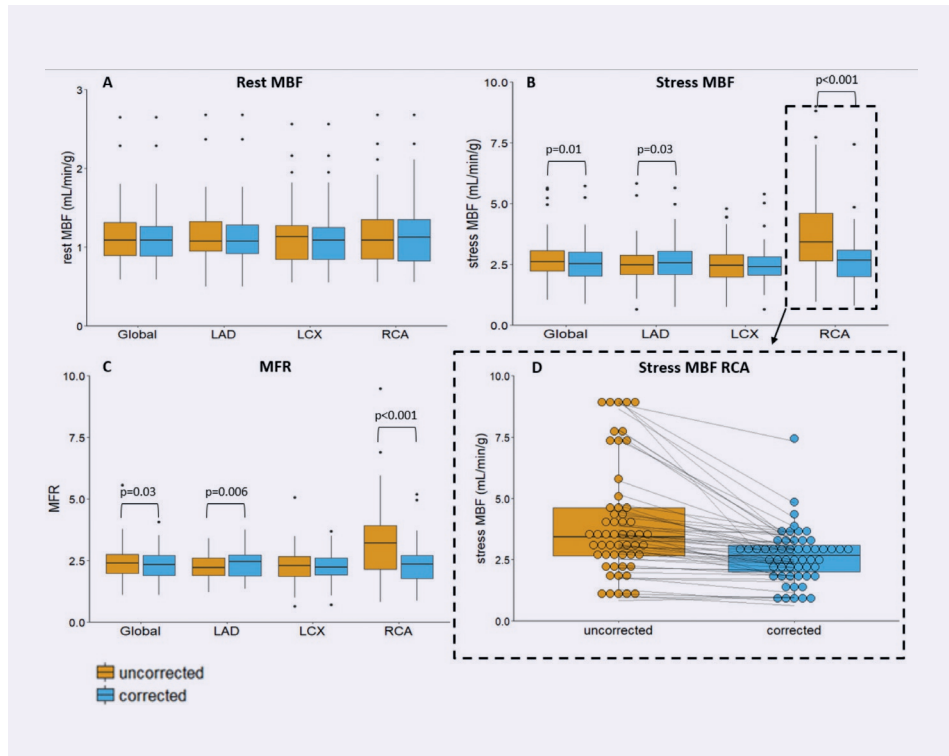


Figure 3. Boxplots showing (A) the rest and (B) stress myocardial blood flows (MBFs) and (C) myocardial flow reserves (MFRs) for the three vascular territories and for the whole myocardium (Global) for the 54 uncorrected and myocardial creep corrected-scans. (D) The stress MBF of the RCA with each point representing one patient scan before and after correction showing MBF decreases in 91% (49/54) of the patients after correction.

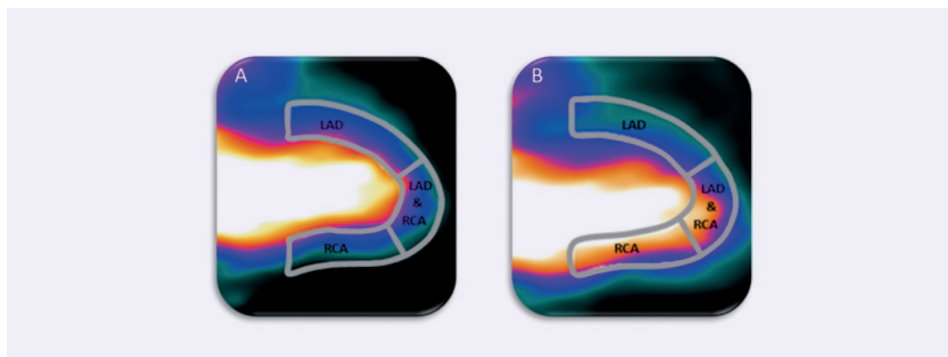


Figure 4. Proper alignment of the automatically drawn myocardium contour and the activity in the heart is shown in A. In case of myocardial creep, there is a misalignment of the drawn myocardium contour with the activity in the heart, as shown in B. This results increased measured activity in the RCA and partly in the LAD territory.

Another mechanism previously described by Friedman et al. which is more likely to cause myocardial creep is that after administration of a pharmacological vasodilator, in our case regadenoson, lung volume increases which causes a repositioning of the diaphragm and heart<sup>24</sup>. Hence, we are unable to prevent this repositioning of the heart and thus the occurrence of myocardial creep.

Several limitations of this study should be recognized. First, we were unable to determine the effect of myocardial creep correction on the diagnostic accuracy due to the lack of a reference standard. However, in some patients myocardial creep resulted in unrealistic high MBF values (>5 mL/min/g) which decreased after correction to realistic values. Hence, we assume that correcting for myocardial creep increases diagnostic reliability.

Second, manual actions are required in the quantification process and for the myocardial creep correction which could have introduced additional operator variability. Although this operator variability might have introduced additional variance, the changes in stress MBF quantification were higher than the previously reported  $\pm 10\%$  test-retest reproducibility errors when calculating the MBF using Rb-82 PET in MPI<sup>31</sup>. Thus, the operator variability is expected to be of limited influence.

Third, a high fraction of the patients had a normal MBF, possibly limiting generalization. However, in case of the poorly perfused tissue with myocardial creep, the influence of spillover from the LV is expected to be larger than that for the normal perfused tissue resulting in a relatively larger overestimation of the modeling parameter  $K_1$  and, hence, MBF<sup>28</sup>. This could result in larger differences between MBF values in the RCA territory before and after myocardial creep correction than those reported in this study.

Finally, we only corrected the myocardial creep in the attenuation-corrected PET images. However, only the PET data acquired between 2:30 and 7:00 minutes were co-registered to the CT to create an attenuation map. As myocardial creep only occurs in the earlier time frames, misregistration and, hence, attenuation-correction artifacts may occur. This misregistration could result in altered MBF measurements<sup>32-35</sup>. Adding a second low-dose CT-scan immediately before the stress PET acquisition is unlikely to improve PET/CT registration as the myocardial creep misregistration occurs after induction of stress and is only temporary. However, we believe that frame-based co-registration of the stress- PET and CT data can improve PET/CT registration and thereby the reliability of Rb-82 PET quantification in patients with myocardial creep<sup>28</sup>.

## NEW KNOWLEDGE GAINED

If myocardial creep is present but remains uncorrected in clinical practice, the stress MBF and MFR of the RCA territory will be overestimated, as shown in Figure 3D, which can lead to incorrect diagnosis. The MFR of the RCA may fall within the normal range of the MFR values (>1.7), while after correcting for myocardial creep, the MFR drops below this threshold, affecting the diagnosis<sup>3</sup>. Moreover, Memmot et al. showed that myocardial creep occurs more frequently when adenosine is used as pharmacological

vasodilator (96%) in comparison with regadenoson (69%)<sup>19</sup>. Therefore, we strongly recommend to check the presence of myocardial creep in all patients regardless of the used pharmacological vasodilator and correct for it to achieve reliable MBF and MFR measurements.

There are two practical ways to recognize myocardial creep in clinical practice. The first sign is an elevated time activity concentration of the RCA during the first-pass phase in the TAC in comparison with the LCX and LAD. As no activity is yet present in the myocardium, the whole activity measured in this phase is due to spillover and should therefore be constant across the three vascular territories, as shown in Figure 1. The second sign is the misalignment between the automatically drawn myocardium contour and the observed activity during the first-pass phase. As in 83% of our patients with myocardial creep an MBF change >10% occurred after correction, this implies that even a small myocardial creep should be corrected in clinical practice.

## CONCLUSIONS

Myocardial creep was seen in 52% of the patients who underwent regadenoson-induced stress Rb-82 PET. Correcting for myocardial creep significantly changed MBF measurements during stress and MFR quantification, especially in the RCA territory. As this may hamper diagnostic accuracy, detection and correction of myocardial creep seem necessary for reliable quantification when using regadenoson.

## REFERENCES

1. Saraste A, Kajander S, Han C, Nesterov SV, Knuuti J. PET: Is myocardial flow quantification a clinical reality? *J Nucl Cardiol*. 2012;19:1044-59.
2. deKemp RA, Yoshinaga K, Beanlands RSB. Will 3-dimensional PET-CT enable the routine quantification of myocardial blood flow? *J Nucl Cardiol* 2007;14:380-397.
3. Sciagra R, Passeri A, Bucierius J, Verberne HJ, Slart RHJA, Lindner O, et al. Clinical use of quantitative cardiac perfusion PET: rationale, modalities and possible indications. Position paper of the Cardiovascular Committee of the European Association of Nuclear Medicine (EANM). *Eur J Nucl Med Mol Imaging* 2016;43:1530-1545.
4. Ziadi MC, DeKemp RA, Williams K, Guo A, Renaud JM, Chow BJW, et al. Does quantification of myocardial flow reserve using rubidium-82 positron emission tomography facilitate detection of multivessel coronary artery disease? *J Nucl Cardiol* 2012;19:670- 80.
5. Parkash R, deKemp RA, Ruddy TD, Kitsikis A, Hart R, Beauschene L, et al. Potential utility of rubidium 82 PET quantification in patients with 3-vessel coronary artery disease. *J Nucl Cardiol* 2004;11:440-9.
6. Santana CA, Folks RD, Garcia EV, Verdes L, Sanyal R, Hainer J, et al. Quantitative (82)Rb PET/CT: development and validation of myocardial perfusion database. *J Nucl Med* 2007;48:1122-8.
7. Machac J. Radiopharmaceuticals for clinical cardiac PET imaging. *Card. PET PET/CT imaging*. New York: Springer; 2007. p. 73-82.
8. Cerqueira MD, Verani MS, Schwaiger M, Heo J, Iskandrian AS. Safety profile of adenosine stress perfusion imaging: Results from the adenoscan multicenter trial registry. *J Am Coll Cardiol* 1994;23:384-9.
9. Ranhosky A, Kempthorne-Rawson J. The safety of intravenous dipyridamole thallium myocardial perfusion imaging. Intravenous Dipyridamole Thallium Imaging Study Group. *Circulation* 1990;81:1205-9.
10. Iskandrian AE, Bateman TM, Belardinelli L, Blackburn B, Cerqueira MD, Hendel RC, et al. Adenosine versus regadenoson comparative evaluation in myocardial perfusion imaging: Results of the ADVANCE phase 3 multicenter international trial. *J Nucl Cardiol* 2007;14:645-58.
11. Jager PL, Buiting M, Mouden M, Oostdijk AHJ, Timmer J, Knollemans S. Regadenoson as a new stress agent in myocardial perfusion imaging. Initial experience in The Netherlands. *Rev Esp Med Nucl Imagen Mol* 2014;33:346-351.
12. Cerqueira MD, Nguyen P, Staehr P, Underwood SR, Iskandrian AE. Effects of age, gender, obesity, and diabetes on the efficacy and safety of the selective A2A agonist regadenoson versus Adenosine in myocardial perfusion imaging. Integrated ADVANCE-MPI Trial Results. *JACC Cardiovasc Imaging* 2008;1:307-316.
13. Johnson SG, Peters S. Advances in pharmacologic stress agents: Focus on regadenoson. *J Nucl Med Technol* 2010;38:163-71.
14. Belardinelli L, Shryock JC, Snowdy S, Zhang Y, Monopoli A, Lozza G, et al. The A2A adenosine receptor mediates coronary vasodilation. *J Pharmacol Exp Ther* 1998;284:1066-73.

15. Hendel RC, Bateman TM, Cerqueira MD, Iskandrian AE, Leppo JA, Blackburn B, et al. Initial clinical experience with regadenoson, a novel selective A<sub>2A</sub> agonist for pharmacologic stress single-photon emission computed tomography myocardial perfusion imaging. *J Am Coll Cardiol* 2005;46:2069-75.
16. Cullom SJ, Case JA, Courter SA, McGhie AI, Bateman TM. Regadenoson pharmacologic rubidium-82 PET: A comparison of quantitative perfusion and function to dipyridamole. *J Nucl Cardiol* 2013;20:76-83.
17. Hsiao E, Ali B, Blankstein R, Skali H, Ali T, Bruyere J Jr, et al. Detection of obstructive coronary artery disease using regadenoson stress and Rb-82 PET/CT myocardial perfusion imaging. *J Nucl Med* 2013;54:1748-54.
18. Goudarzi B, Fukushima K, Bravo P, Merrill J, Bengel FM. Comparison of the myocardial blood flow response to regadenoson and dipyridamole: A quantitative analysis in patients referred for clinical <sup>82</sup>Rb myocardial perfusion PET. *Eur J Nucl Med Mol Imaging* 2011;38:1908-16.
19. Memmott MJ, Tonge CM, Saint KJ, Arumugam P. Impact of pharmacological stress agent on patient motion during rubidium-82 myocardial perfusion PET/CT. *J Nucl Cardiol* 2017;1-10.
20. Hunter CRRN, Klein R, Beanlands RS, deKemp RA. Patient motion effects on the quantification of regional myocardial blood flow with dynamic PET imaging. *Med Phys* 2016;43:1829-40.
21. Koshino K, Watabe H, Enmi J, Hirano Y, Zeniya T, Hasegawa S, et al. Effects of patient movement on measurements of myocardial blood flow and viability in resting <sup>15</sup>O-water PET studies. *J Nucl Cardiol* 2012;19:524-33.
22. Murthy VL, Bateman TM, Beanlands RS, Berman DS, Borges-Neto S, Chareonthitawee P, et al. Clinical quantification of myocardial blood flow using PET: Joint position paper of the SNMMI cardiovascular council and the ASNC. *J Nucl Cardiol* 2018;25:269-97.
23. Piccinelli M, Votaw JR, Garcia EV. Motion correction and its impact on absolute myocardial blood flow measures with PET. *Curr Cardiol Rep* 2018;20:34.
24. Friedman J, Van Train K, Maddahi J, Rozanski A, Prigent F, Bietendorf J, et al. Upward creep of the heart: a frequent source of false-positive reversible defects during thallium-201 stress-redistribution SPECT. *J Nucl Med* 1989;30:1718-22.
25. Lortie M, Beanlands RSB, Yoshinaga K, Klein R, DaSilva JN, DeKemp RA. Quantification of myocardial blood flow with <sup>82</sup>Rb dynamic PET imaging. *Eur J Nucl Med Mol Imaging* 2007;34:1765-74.
26. van Dijk JD, Jager PL, van Dalen JA. Pitfalls in myocardial blood flow quantification with rubidium-82 PET. *Tijdschr voor Nucl Geneesk* 2017;39:1822-1829.
27. Votaw JR, Packard RRS. Technical aspects of acquiring and measuring myocardial blood flow: Method, technique, and QA. *J Nucl Cardiol* 2017;1-6.
28. Lee BC, Moody JB, Poitrasson-Rivière A, Melvin AC, Weinberg RL, Corbett JR, et al. Blood pool and tissue phase patient motion effects on <sup>82</sup>rubidium PET myocardial blood flow quantification. *J Nucl Cardiol* 2018;1-12.
29. Karacalioglu AO, Jata B, Kilic S, Arslan N, Ilgan S, Ozguven MA. A physiologic approach to decreasing upward creep of the heart during myocardial perfusion imaging. *J Nucl Med Technol* 2006;34:215-9.



30. van Dijk JD, van Dalen JA, Mouden M, Ottervanger JP, Knollema S, Slump CH, et al. Value of automatic patient motion detection and correction in myocardial perfusion imaging using a CZT-based SPECT camera. *J Nucl Cardiol* 2016;1-10.
31. Kitkungvan D, Johnson NP, Roby AE, Patel MB, Kirkeeide R, Gould KL. Routine clinical quantitative rest stress myocardial perfusion for managing coronary artery disease: Clinical relevance of test-retest variability. *JACC Cardiovasc Imaging* 2017;10:565-77.
32. Rajaram M, Tahari AK, Lee AH, Lodge MA, Tsui B, Nekolla S, et al. Cardiac PET/CT misregistration causes significant changes in estimated myocardial blood flow. *J Nucl Med* 2013;54:50-4.
33. Martinez-Moñller A, Souvatzoglou M, Navab N, Schwaiger M, Nekolla SG. Artifacts from misaligned CT in cardiac perfusion PET/CT studies: frequency, effects, and potential solutions. *J Nucl Med* 2007;48:188-93.
34. Loghin C, Sdringola S, Gould KL. Common artifacts in PET myocardial perfusion images due to attenuation-emission misregistration: clinical significance, causes, and solutions. *J Nucl Med* 2004;45:1029-39.
35. Gould KL, Pan T, Loghin C, Johnson NP, Guha A, Sdringola S. Frequent diagnostic errors in cardiac PET/CT due to misregistration of CT attenuation and emission PET images: A definitive analysis of causes, consequences, and corrections. *J Nucl Med* 2007;48:1112-21.



# HOW TO DETECT AND CORRECT MYOCARDIAL CREEP IN MYOCARDIAL PERFUSION IMAGING

## USING RUBIDIUM-82 PET

### Authors

S. S. Koenders<sup>1,2</sup>

J. D. van Dijk<sup>1</sup>

P. L. Jager<sup>1</sup>

J. P. Ottervanger<sup>3</sup>

C. H. Slump<sup>2</sup>

J. A. van Dalen<sup>4</sup>

### Author Affiliations

1. Department of Nuclear Medicine, Isala Hospital, Zwolle, The Netherlands
2. Technical Medical Centre, University of Twente, Enschede, the Netherlands
3. Department of Cardiology, Isala Hospital, Zwolle, The Netherlands
4. Department of Medical Physics, Isala Hospital, Zwolle, The Netherlands

### Published in

Journal of Nuclear Cardiology 2019;26:729-74



## ABSTRACT

Reliability of myocardial blood flow (MBF) quantification in myocardial perfusion imaging (MPI) using PET can majorly be affected by the occurrence of myocardial creep when using pharmacologically induced stress. In this paper, we provide instructions on how to detect and correct for myocardial creep. For example, in each time frame of the PET images the myocardium contour and the observed activity have to be compared to check for misalignments. In addition, we provide an overview of the functionality of commonly used software packages to perform this quality control step as not all software packages currently provide this functionality. Furthermore, important clinical considerations to obtain accurate MBF measurements are given.

### Keywords

Myocardial blood flow; PET myocardial perfusion imaging; Rb-82; Myocardial creep; pharmacological vasodilators.

## INTRODUCTION

Myocardial blood flow (MBF) quantification in myocardial perfusion imaging (MPI) using Rubidium-82 (Rb-82) PET provides valuable information about the extent and functional importance of possible stenosis<sup>1-3</sup>. However, the reliability of MBF quantification can be affected by the occurrence of myocardial creep, in particular during stress imaging<sup>4</sup>. This myocardial creep is presumably caused by the increasing respiration and lung volume and thereby repositioning of the diaphragm and heart after administration of a pharmacological vasodilator<sup>5, 6</sup>. It mainly affects activity concentration measurements in the right coronary artery (RCA) territory as illustrated in Figure 1<sup>4</sup>. As activity concentration measurements are used in compartmental analyses to derive MBFs, it is essential that these measurements are reliable to prevent biased MBF measurements and thereby false diagnostic interpretation<sup>4</sup>.

In our recent study, we observed a myocardial creep during regadenoson-induced stress in 52% of the 104 consecutively included patients<sup>4</sup>. In 83% of these 54 patients, myocardial creep resulted in a MBF change >10%, which may influence diagnostic interpretation. Although our study only comprised regadenoson-induced stress, the presence of myocardial creep is also reported with adenosine as pharmacological vasodilator<sup>6</sup>. In a limited amount of patients (2%), myocardial creep can also affect MBF quantification using rest imaging<sup>4</sup>. As MBF quantification can become biased when myocardial creep remains uncorrected, detection and correction are necessary for all pharmacological vasodilators and for both rest and stress scans. In this paper, we show how myocardial creep can be detected and corrected. Furthermore, we provide an overview of the possibilities of commercially available software packages to detect and correct myocardial creep and highlight important clinical considerations.

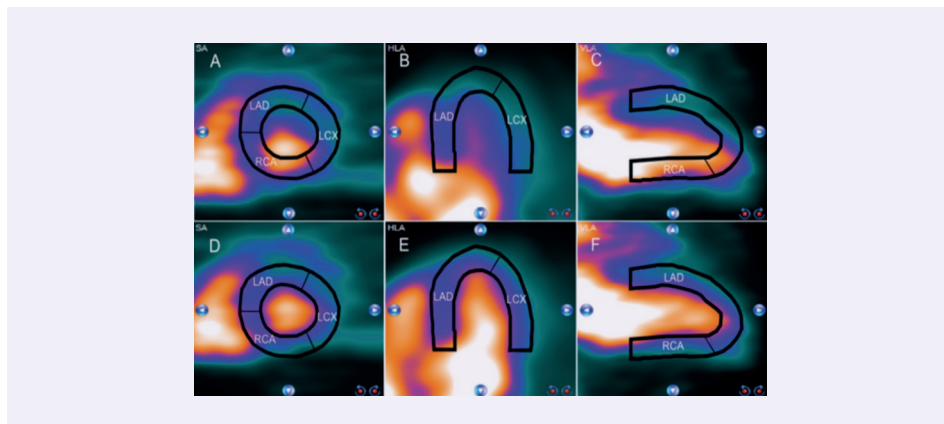


**Figure 1.** Example of a stress Rb-82 PET scan of a patient with myocardial creep, before (A to C) and after myocardial creep correction (D to F). The myocardium contour is shown in black and the vascular trajectories that primarily supply certain areas of the myocardium with blood are indicated. The appearance of myocardial creep is indicated by the misalignment between the observed Rb-82 activity and the myocardium contour (A to C). Especially the activity concentration in the right coronary artery (RCA) territory is affected when comparing the uncorrected (A to C) with the corrected images (D to F). From left to right: the short axis, horizontal axis, and vertical long axis. LAD, left anterior descending; LCX, left circumflex artery.

## METHODOLOGY

### Background: MBF quantification

Several steps have to be performed prior to quantification of MBF: (1) dynamic PET acquisition; (2) image reconstruction of the PET data; (3) segmentation of the myocardium contour; (4) derivation of time-activity curves (TACs) of the myocardium and the left ventricle (LV); (5) quality control; and (6) compartmental analyses<sup>7</sup>.

The first step starts with a PET acquisition of typically 7 minutes for both the rest and stress scans directly after Rb-82 administration. Typically, a low-dose CT scan is added to provide an attenuation map of the chest to allow attenuation correction. Next, the PET images are reconstructed in several time frames (step 2) where the first-pass phase or blood-pool phase is generally sampled with small frame durations of five to ten seconds to assure sufficient temporal resolution and prevent under-sampling of the LV TAC<sup>8-10</sup>.

Subsequently, a myocardium contour is drawn, based on all data acquired during the tissue phase where a steady state is reached, i.e., data acquired >2:15 minutes after Rb-82 administration (step 3),<sup>11</sup> as the activity is then primarily present in the myocardium. This contour is used to derive the activity concentrations over time for the whole myocardium or a specific myocardial region. The most common regions are those supplied by blood by one of the three main coronary arteries: left anterior descending (LAD), left circumflex (LCX), and RCA. In addition, the activity concentration in the LV is estimated by using, for example, a region of interest (ROI) positioned in the cavity of the LV. Both the myocardium contour and the LV ROI are used to automatically derive TACs (step 4). To calculate the MBF for the whole myocardium or a specific region, the TACs from the corresponding myocardial area and the LV are used as input for compartmental analyses. The one-tissue compartment model is most commonly used for this analysis when using Rb-82 (step 6)<sup>8</sup>.

To obtain reliable MBF measurements, a quality control (step 5) has to be performed which covers the detection and correction of myocardial creep. We previously defined myocardial creep as a gradual decreasing misalignment of the myocardium contour with the activity present in the ventricle and/or myocardium primarily in the inferior direction<sup>4</sup>. Myocardial creep should be corrected if the misalignment is more than one-third of the width of the left ventricular myocardial wall and is present in at least 2 time frames during the first-pass phase<sup>4</sup>.

## MYOCARDIAL CREEP DETECTION AND CORRECTION

As it is essential to check and correct for myocardial creep,<sup>4</sup> we first provide instructions for detection and correction in general, followed by an example based on commercial processing software (Corridor4DM, Invia).

### General procedure

The detection and correction procedure consists of seven steps, as shown in Figure 2A to G. After the PET data are acquired (A), the geometric position of the myocardium contour has to be determined (B) to detect myocardial creep. This is generally done by reconstructing the PET data collected after 2:15 minutes into one image, as the activity is then primarily present in the myocardium. It is important

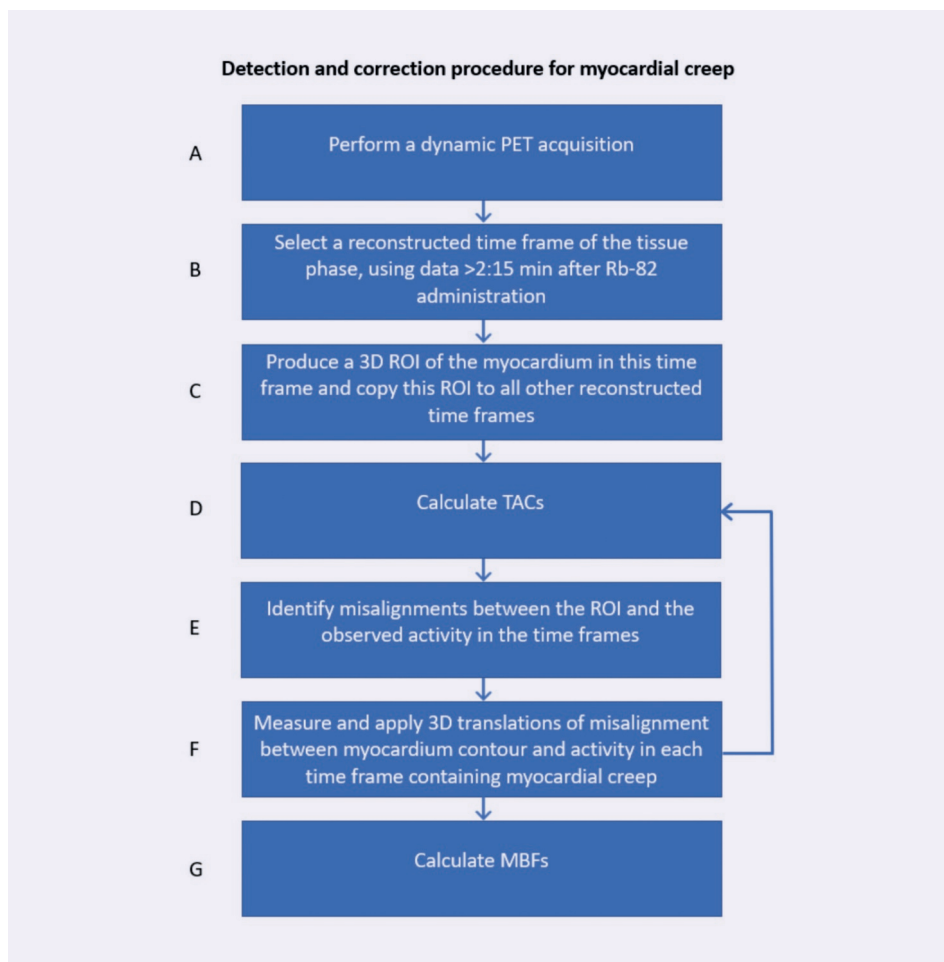


Figure 2. General procedure for the detection and correction of myocardial creep.



that this image reconstruction is based on a sufficient number of photon counts to provide a clear image of the myocardium. Next, the geometric position of the myocardium can be obtained by drawing a 3D ROI with a fixed threshold of typically 70% of the maximum pixel value in the myocardium (C). The myocardium contour then needs to be copied to all the other time frames of the dynamic acquisition. After the TACs are calculated (D), the position of the 3D ROI and the observed activity distribution in each frame have to be compared (E) as misalignment may indicate myocardial creep. If myocardial creep is present, it can be corrected for by estimating the misalignment in the x-, y- and z-direction for each time frame in which myocardial creep is visible (F). This geometrical translation can be used to realign the observed activity to the myocardium contour by, for example, changing the initial coordinates in the DICOM header of the PET data for each of the time frames containing myocardial creep. The calculation of the TACs then has to be repeated to calculate reliable MBFs (G).

### **Illustration using commercial software**

It is possible to perform the detection and correction steps in some commercially available software, for example in Corridor4DM v2016. This software automatically derives an image reconstruction of the acquired PET data between 2:30 and 6:00 minutes after Rb-82 administration. After assigning the three cardiac axes, a myocardium contour is automatically drawn in the PET image which can manually be optimized if needed. Next, the user has to manually position a ROI at the center of the mitral valve. This ROI is used to estimate the activity concentration in the LV, as illustrated in Figure 3A. The myocardium contour is then automatically projected to all time frames of the dynamic PET series.

Corridor4DM has the option to scroll through the time frames which makes it possible to detect myocardial creep, as shown in Figure 3B. Myocardial creep can also be identified by observing the TACs. The TAC of the RCA territory then typically shows a higher peak during the first-pass phase compared to those of the other territories (Figure 3C). This higher peak is due to motion of the heart in the inferior direction, which is related to myocardial creep.

Besides detecting myocardial creep, Corridor4DM also provides the possibility to correct for this movement by manually realigning the myocardium contour with the activity for each individual time frame, as shown in Figure 3D. After applying this manual realignment in each time frame with myocardial creep, the peaks of the TACs of the three vascular territories (LAD, LCX, and RCA) become comparable (Figure 3E). This ensures the user that a reliable correction for myocardial creep is performed, allowing reliable MBF measurements.

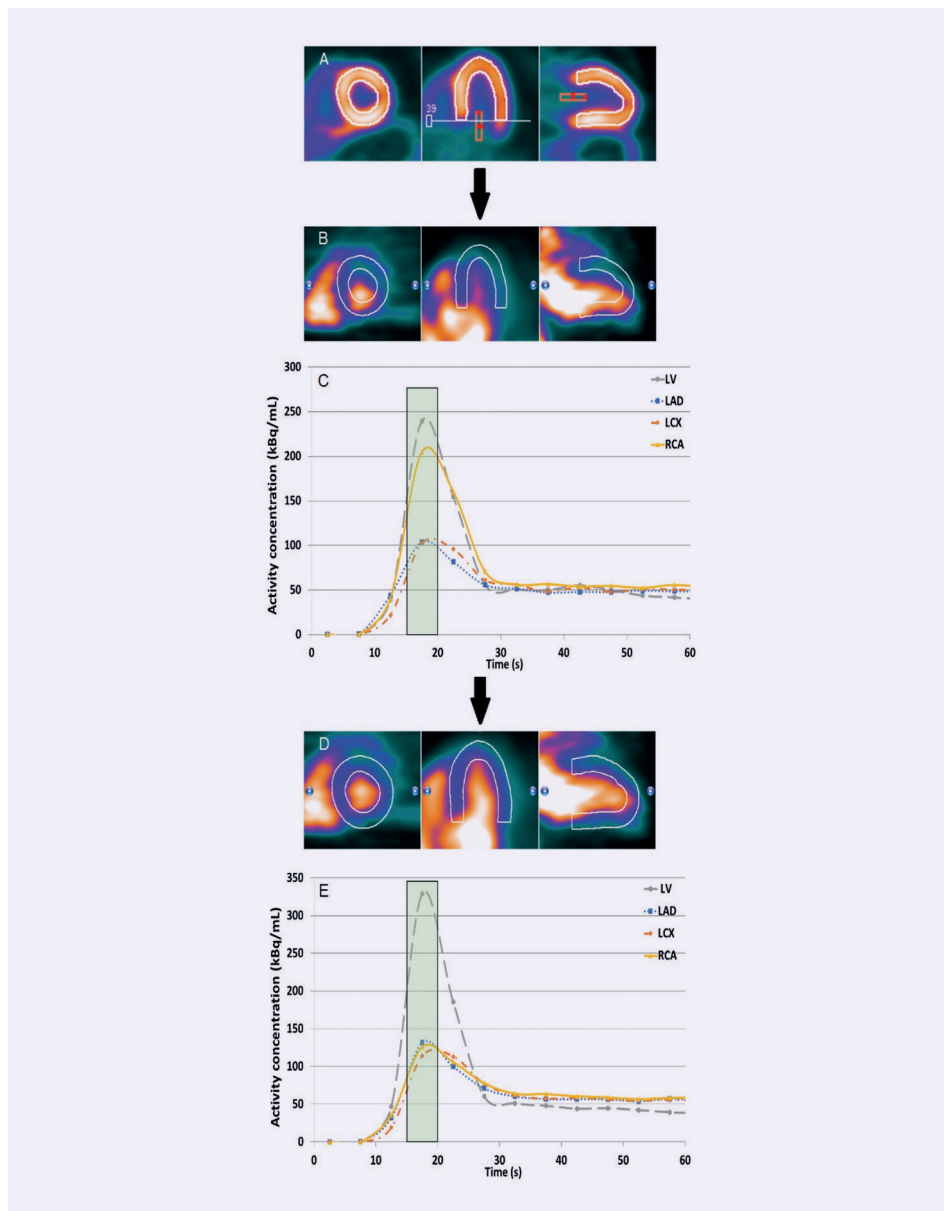


**Figure 3.** Overview of the three main steps to detect and correct for myocardial creep using Corridor4DM. The myocardium contour is drawn by assigning the most basal part of the septum which still contains activity, and the activity concentration in the left ventricle (LV) is measured by placing a region of interest (ROI) manually at the center of the mitral valve (A). To detect myocardial creep, the observed activity in the myocardium has to be compared visually with the myocardium contour in each time frame. The misalignment in the time frame from 15 to 20 seconds shown in B indicates myocardial creep. The first 60 seconds of the TAC of this time frame (C) shows a higher peak in the right coronary artery (RCA) territory compared to those of the other two vascular territories, indicating myocardial creep. In D, the observed activity in the myocardium is realigned to the myocardium contour. This results in comparable peaks of the TACs of the three vascular territories (E). From left to right (A, B, D): the short axis, horizontal axis, and vertical long axis. LAD, left anterior descending; LCX, left circumflex artery.

## AVAILABILITY IN COMMERCIAL SOFTWARE PACKAGES

As myocardial creep may hamper diagnostic interpretation, accurate detection and correction of myocardial creep are necessary for reliable MBF quantification. Although the detection is most of the time straightforward, correction can be complicated and is not always feasible in the clinical routine due to missing functionality of the used software. From the latest versions of four commonly known and used commercially software packages to quantify MBF using Rb-82 PET, Corridor4DM and QPET (Cedars-Sinai) have the ability to visually evaluate the detection and correction of myocardial creep. SyngoMBF (Siemens Healthcare) provides the functionality to automatically detect and correct for motion, such as myocardial creep, but does not provide insight in the accuracy of the correction. Moreover, it is not possible to manually adjust this correction. Lastly, FlowQuant (University of Ottawa Heart Institute) currently does not have a feature for detection and correction of myocardial creep.

## CONSIDERATIONS

Measurements of MBF using Rb-82 PET are affected by many methodological factors such as differences in equipment, acquisition and reconstruction settings, processing software, tracer infusion, temporal sampling, and compartmental analyses<sup>12</sup>. Awareness of all potential pitfalls and underlying assumptions in methodology are essential for using MBF measurements in clinical practice. For example, it is important that a constant activity injection profile is used together with an adequate number and length of time frames, to prevent under-sampling and that myocardial creep is adequately corrected.

Although we focused on Rb-82 PET, it is likely that myocardial creep occurs in a similar way using other PET tracers such as Oxygen-15 water and Nitrogen-13 ammonia. Therefore, detection and correction should always be performed in quantitative PET MPI studies, independent of the tracer.

Physicians should always check for accurate myocardial creep correction before clinical interpretation. This can be performed by inspecting the TAC for an elevated peak of the RCA during the first-pass phase in comparison to the LAD and LCX as shown in Figure 3C<sup>4</sup>. Physicians can also visually assess the individual time frames for misalignments between the myocardium contour and the activity in the myocardium as shown in Figure 3B.

In conclusion, adequate detection and correction of myocardial creep are crucial for reliable MBF quantification. To adequately perform the required quality control, it is not only important that software packages provide the possibility to detect and correct myocardial creep, but also that users can visually inspect and evaluate these steps. Hence, vendors should provide this functionality or adapt their software accordingly.

## REFERENCES

1. Ziadi MC, DeKemp RA, Williams K, Guo A, Renaud JM, Chow BJW, et al. Does quantification of myocardial flow reserve using rubidium-82 positron emission tomography facilitate detection of multivessel coronary artery disease? *J Nucl Cardiol* 2012;19:670-80.
2. Parkash R, deKemp RA, Ruddy TD, Kitsikis A, Hart R, Beauschene L, et al. Potential utility of rubidium 82 PET quantification in patients with 3-vessel coronary artery disease. *J Nucl Cardiol* 2004;11:440-9.
3. Santana CA, Folks RD, Garcia EV, Verdes L, Sanyal R, Hainer J, et al. Quantitative (82)Rb PET/CT: development and validation of myocardial perfusion database. *J Nucl Med* 2007;48:1122-8.
4. Koenders SS, van Dijk JD, Jager PL, Ottervanger JP, Slump CH, van Dalen JA. Impact of regadenoson induced myocardial creep on dynamic Rubidium-82 PET myocardial blood flow quantification. *J Nucl Cardiol*. <https://doi.org/10.1007/s12350-019-01649-4>.
5. Friedman J, Van Train K, Maddahi J, Rozanski A, Prigent F, Bietendorf J, et al. Upward creep of the heart: a frequent source of false-positive reversible defects during thallium-201 stress-redistribution SPECT. *J Nucl Med* 1989;30:1718-22.
6. Memmott MJ, Tonge CM, Saint KJ, Arumugam P. Impact of pharmacological stress agent on patient motion during rubidium-82 myocardial perfusion PET/CT. *J Nucl Cardiol* 2017;24:1-10.
7. Nesterov SV, Lee BC, Moody JB, Slomka P, Han C, Knuuti JM. The status and future of PET myocardial blood flow quantification software. *Ann Nucl Cardiol* 2016;2:106-10.
8. Klein R, Ocneanu A, deKemp RA. Time-frame sampling for 82Rb PET flow quantification: Towards standardization of clinical protocols. *J Nucl Cardiol* 2017;24:1530-4.
9. Lee BC, Moody JB, Weinberg RL, Corbett JR, Ficaro EP, Murthy VL. Optimization of temporal sampling for 82rubidium PET myocardial blood flow quantification. *J Nucl Cardiol* 2017;24:1517-29.
10. Murthy VL, Bateman TM, Beanlands RS, Berman DS, Borges-Neto S, Chareonthaitawee P, et al. Clinical quantification of myocardial blood flow using PET: Joint position paper of the SNMMI cardiovascular council and the ASNC. *J Nucl Cardiol* 2018;25:269-97.
11. van Dijk JD, Huizing ED, van Dalen JA, Timmer JR, Jager PL. Minimal starting time of data reconstruction for qualitative myocardial perfusion rubidium-82 positron emission tomography imaging. *Nucl Med Commun* 2018;39:533-8.
12. Moody JB, Lee BC, Corbett JR, Ficaro EP, Murthy VL. Precision and accuracy of clinical quantification of myocardial blood flow by dynamic PET: A technical perspective. *J Nucl Cardiol* 2015;22:935-51.





The background of the slide is a solid orange color with a white wireframe grid pattern. A white rectangular box is positioned in the upper left quadrant, containing the text 'PART II' and the main title. The main title is in a large, bold, purple font, while 'PART II' is in a smaller, bold, orange font. The wireframe pattern consists of interconnected lines forming a grid that follows the contours of a human figure, though the figure itself is not clearly defined.

**PART II**

**CLINICAL VALUE OF  
MBF QUANTIFICATION**

1.4

2.7

2.9

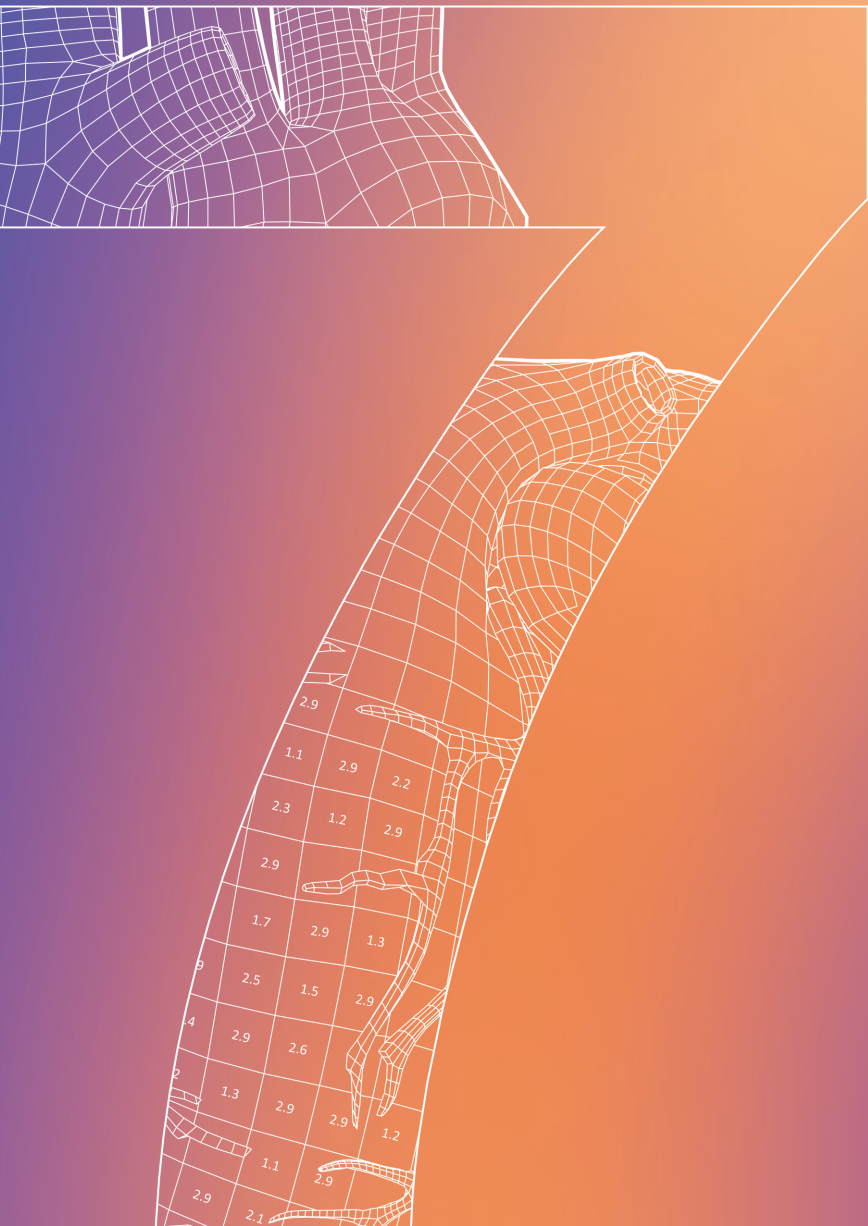
2

2.9

2.9

1

2.9



2.9		
1.1	2.9	2.2
2.3	1.2	2.9
2.9		
1.7	2.9	1.3
2.5	1.5	2.9
2.9	2.6	
1.3	2.9	2.9
1.1		1.2
2.9	2.9	
2.1		



# DIAGNOSTIC VALUE OF REGIONAL MYOCARDIAL FLOW RESERVE MEASUREMENTS

## USING RUBIDIUM-82 PET

### Authors

S. S. Koenders<sup>1,4</sup>

J. A. van Dalen<sup>2</sup>

P. L. Jager<sup>1</sup>

M. Mouden<sup>3</sup>

C. H. Slump<sup>4</sup>

J. D. van Dijk<sup>1</sup>

### Author Affiliations

1. Department of Nuclear Medicine, Isala Hospital, Zwolle, The Netherlands
2. Department of Medical Physics, Isala Hospital, Zwolle, The Netherlands
3. Department of Cardiology, Isala Hospital, Zwolle, The Netherlands
4. Technical Medical Centre, University of Twente, Enschede, the Netherlands

### Published in

The International Journal of Cardiovascular Imaging 2022;  
Epub ahead of print



## ABSTRACT

### Purpose

Visual assessment of Rubidium (Rb-82) PET myocardial perfusion images is usually combined with global myocardial flow reserve (MFR) measurements. However, small regional blood flow deficits may go unnoticed. Our aim was to compare the diagnostic value of regional with global MFR in the detection of obstructive coronary artery disease (oCAD).

### Methods

We retrospectively included 1519 patients referred for rest and regadenoson-induced stress Rb-82 PET/CT without prior history of oCAD. MFR was determined globally, per vessel territory and per myocardial segment and compared using receiver-operating characteristic analysis. Vessel MFR was defined as the lowest MFR of the coronary territories and segmental MFR as the lowest MFR of the 17-segments. The primary endpoint was oCAD on invasive coronary angiography.

### Results

The 148 patients classified as having oCAD had a lower global MFR (median 1.9, interquartile range [1.5 – 2.4] vs. 2.4 [2.0 – 2.9]), lower vessel MFR (1.6 [1.2 – 2.1] vs. 2.2 [1.9 – 2.6]) and lower segmental MFR (1.3 [0.9 – 1.6] vs. 1.8 [1.5 – 2.2]) as compared to the non-oCAD patients ( $p < 0.001$ ). The area under the curve for segmental MFR (0.81) was larger ( $p \leq 0.005$ ) than of global MFR (0.74) and vessel MFR (0.78).

### Conclusions

The use of regional MFR instead of global MFR is recommended as it improves the diagnostic value of Rb-82 PET in the detection of obstructive CAD.

### Keywords

Myocardial blood flow; PET myocardial perfusion imaging; Rubidium-82.

## INTRODUCTION

Myocardial perfusion imaging (MPI) using positron emission tomography (PET) has a high diagnostic value in the detection of myocardial ischemia and is growing in its use<sup>1</sup>. The addition of absolute myocardial flow reserve (MFR) measurements to the visual assessment of PET images has become part of the clinical routine and provides additional information about the extent and functional importance of possible stenoses<sup>2-7</sup>. For the visual assessment physicians usually assess the relative uptake in the different regions of the myocardium by using the 17 segment model to detect possible ischemia or infarctions. With oxygen-15-labelled water (O-15 H<sub>2</sub>O) PET it is already common practice to assess regional flow values in the evaluation of obstructive coronary artery disease (oCAD)<sup>8</sup>. However, with Rubidium-82 (Rb-82) PET flow values are often only assessed for the myocardium as a whole (global) and assessing regional flows are not specifically recommended by European guidelines<sup>2-9</sup>. Small regional blood flow deficits may therefore go unnoticed when only looking at global flow values, potentially limiting the diagnostic value of Rb-82 PET. Hence, our aim was to compare the diagnostic value of regional MFR with global MFR measurements using Rb-82 PET in the detection of oCAD.

## MATERIALS AND METHODS

### Study population

We retrospectively included 1519 consecutive patients without prior history of oCAD referred for rest and regadenoson-induced stress Rb-82 PET/CT (GE Discovery 690, GE Healthcare) between May 2017 and February 2019. We routinely use this PET technique for all patients. Information about the patients history, demographics and risk factors were obtained by review of medical records and a questionnaire. As this study was retrospective approval by the medical ethics committee was not required according to Dutch law. Nevertheless, all patients provided written informed consent for the use of their data for research purposes.

### Patient preparation and data acquisition

All subjects were asked to refrain from caffeine containing substances for 24 hours and to discontinue dipyridamole containing medication for 48 hours before imaging. All patients underwent a MPI rest scan followed by a regadenoson-induced stress scan. Prior to the PET acquisition, a low-dose CT scan was acquired during free-breathing to provide an attenuation map of the chest. This scan was made using a 0.8 s rotation time, pitch of 0.97, collimation of 32x0.625 mm, tube voltage of 120 kV, and a tube current of 10 mA. Next, a fixed activity of 740 MBq Rb-82 was administered intravenously with a flow rate of 50 mL/min using a Strontium-82/Rb-82 generator (CardioGen-82, Bracco Diagnostics Inc.) immediately followed by a seven-minute PET list-mode acquisition. Ten minutes after the first activity bolus, we induced pharmacological stress by administering 400 µg (5 mL) of regadenoson over 10 seconds. After a 5 mL saline flush (NaCl 0.9%), we administered a second dose of 740 MBq Rb-82 followed by a 7 minute stress PET acquisition.

### Image reconstruction

The low-dose CT scans were reconstructed using an iterative reconstruction method (70% adaptive statistical iterative reconstruction algorithm, ASIR) and a slice thickness of 5 mm. Attenuation correction was applied to all PET data. Next, we reconstructed dynamic PET data using 26 time frames (12x5 s, 6x10 s, 4x20 s and 4x40 s) with default settings as recommended by the manufacturer using 3D-ordered subset expectation maximization (OSEM) technique using 2 iterations and 24 subsets and a Gaussian post-smoothing filter of 12 mm while correcting for decay, attenuation, scatter and random coincidences and dead time effects. The voxel size was 3.3 x 3.3 x 3.3 mm<sup>3</sup>. Neither time-of-flight correction, nor a post-processing filter or resolution modelling was applied for the dynamic image reconstructions.

### Data analysis

We used Corridor4DM (Invia Medical Imaging Solutions, v2016.02.64) software to post-process the reconstructions. Myocardium contours were automatically detected in both rest and stress scans and manually realigned when necessary. Furthermore, a region of interest (ROI) was manually placed at the location of the mitral valve to estimate the activity in the blood pool. Next, the activity concentrations in the myocardium contour and ROI were measured in the 26 reconstructed time frames to calculate the time activity curves (TACs) for the left ventricle (LV), whole myocardium (global), left anterior descending (LAD), left circumflex (LCX) and right coronary (RCA) artery and for each of the 17-segments. The one-tissue compartment model of Lortie et al.<sup>10</sup> was used to calculate the myocardial blood flow (MBF) from the TACs using Corridor4DM. Rest MBF was calculated without rate-pressure product correction. Furthermore, myocardial flow reserve (MFR) was calculated as the ratio of stress MBF divided by rest MBF for the myocardium as a whole (further referred by global MFR), the three vascular territories and for all 17 segments. Vessel MFR was defined as the lowest flow reserve of LAD, LCX and RCA territories and segmental MFR as the lowest flow reserve of the 17 segments. All relative Rb-82 PET images were also visually assessed by two expert readers and classified as normal or as abnormal, where abnormal was defined as having a reversible and/or irreversible defect.

### Follow-up

Our primary endpoint was a diagnosis of oCAD, as the purpose of Rb-82 PET in clinical practice is to assess the extent and functional importance of stenosis in order to tailor treatment and hopefully prevent the occurrence of hard events in the future. Patients were classified as having oCAD if follow-up included either a conclusive invasive coronary angiography (ICA) for CAD as defined by a significant fractional flow reserve measurement (<0.8) or >70% stenosis in the LAD, LCX or RCA, or >50% stenosis in the left main on ICA during follow-up<sup>11</sup>. Patients who did not undergo ICA during follow-up or patients who underwent ICA but were diagnosed as not having oCAD were classified as non-obstructive CAD (non-oCAD). In addition, a composition of oCAD and occurrence of all-cause mortality was used as a secondary outcome.

### Statistical analysis

Patient characteristics and continuous variables were expressed as mean  $\pm$  standard deviation (SD) or median [interquartile range]. Statistical analysis was performed using IBM SPSS (IBM SPSS Statistics for Windows, Version 26.0. Armonk, NY: IBM Corp). To assess differences between patient characteristics the Student's t-test, Mann–Whitney U test or  $\chi^2$ -test were performed. Receiver-operating characteristic (ROC) analyses were conducted to evaluate and compare the diagnostic value of global, vessel and segmental MFR by paired-analyses of the difference of the area under the curve (AUC). A sub-analyses was performed to assess the difference of the AUC on scans visually classified as normal or abnormal. The level of statistical significance was set to  $p < 0.05$ .

## RESULTS

The median follow-up was 23 months [interquartile range: 18 - 27] with a minimal follow-up of 12 months. Of the 1519 included patients 148 were classified as having oCAD according to ICA. Most cases (72%) of oCAD occurred within 90 days after the PET scan. Of the remaining 1371 patients, 17 (1%) underwent ICA but were classified as non-oCAD. An additional 49 patients died during follow-up. Patients in the oCAD group (N=148) and non-oCAD group (N=1371) did not differ regarding weight, height, body mass index (BMI) and the risk factors smoking, hypertension, dyslipidaemia and family history ( $p \geq 0.06$ ) as shown in Table 1. Yet, patients in the oCAD group were older, suffered more often from diabetes, and were more often male ( $p \leq 0.02$ ).

The 148 patients classified as having oCAD had a lower global MFR (median 1.9 interquartile range [1.5 – 2.4] vs. 2.4 [2.0 – 2.9]), vessel MFR (1.6 [1.2 – 2.1] vs. 2.2 [1.9 – 2.6]) and segmental MFR (1.3 [0.9 – 1.6] vs. 1.8 [1.5 – 2.2]) in comparison to the non-oCAD patients, respectively ( $p < 0.001$ ), as shown in Figure 1. ROC analysis for oCAD showed that the AUC of segmental MFR (0.81) was significantly larger ( $p \leq 0.005$ ) than the AUC of global MFR (0.74) and vessel MFR (0.78), as shown in Figure 2A. To achieve the same sensitivity and specificity as for global MFR, the cut-off value for vessel and segmental MFR is lower as compared to global MFR, as shown in Figure 2C. Moreover, the trade-off between the sensitivity and specificity is dependent of the chosen cut-off value. After classification of all relative Rb-82 PET scans into normal (N=1259) or abnormal (N=260), the AUC of segmental MFR (0.75 and 0.73) was larger ( $p \leq 0.047$ ) than the AUC of global MFR (0.70 and 0.67), respectively, as shown in Figure 3.

When looking at the second endpoint, a composite of oCAD and all-cause mortality, segmental MFR also showed a higher AUC (0.79) as compared to global (0.74) and vessel MFR (0.77) ( $p \leq 0.04$ ) (Figure 2B). After classification of all relative Rb-82 PET scans into normal or abnormal the AUC of segmental MFR (0.74) was larger in the abnormal Rb-82 PET scans as compared to global (0.69) MFR ( $p = 0.03$ ), as shown in Figure 4B. However, for the visually normal scans, the AUC of global, vessel and segmental MFR did not differ ( $p > 0.3$ ). A case example demonstrating the higher diagnostic value of segmental MFR as compared to global MFR is shown in Figure 5.

Table 1. Baseline characteristics and outcomes of the patient population (n=1519).

Characteristic	Obstructive CAD (N=148)	Non-obstructive CAD (N=1371)	p values
Age (years)	69 ± 9	66 ± 11	0.002
Male gender (%)	71	49	<0.001
Weight (kg)	88 ± 17	89 ± 20	0.89
Height (cm)	175 ± 9	174 ± 10	0.25
BMI (kg/m <sup>2</sup> )	29 ± 5	29 ± 6	0.53
Current smoker (%)	12	13	0.83
Hypertension (%)	68	62	0.19
Diabetes (%)	28	20	0.02
Dyslipidaemia (%)	50	42	0.06
Family history (%)	45	52	0.11
Global rest MBF	1.0 [0.8-1.3]	1.0 [0.8-1.3]	0.44
Vessel rest MBF	0.9 [0.8-1.2]	1.0 [0.8-1.2]	0.41
Segmental rest MBF	0.7 [0.6-1.0]	0.8 [0.6-1.0]	0.21
Global stress MBF	1.9 [1.5-2.4]	2.5 [2.1-3.0]	<0.001
Vessel stress MBF	1.6 [1.2-2.2]	2.3 [1.9-2.8]	<0.001
Segmental stress MBF	1.3 [0.8-1.7]	1.9 [1.6-2.4]	<0.001
Global MFR	1.9 [1.5-2.4]	2.4 [2.0-2.9]	<0.001
Vessel MFR	1.6 [1.2-2.1]	2.2 [1.9-2.6]	<0.001
Segmental MFR	1.3 [0.9-1.6]	1.8 [1.5-2.2]	<0.001
Time to follow-up (months)	22 [19-27]	23 [18-27]	0.79
PCI during follow-up (%)	53%	NA	NA
CABG during follow-up (%)	41%	NA	NA
Time to confirmation obstructive CAD (weeks)	5.4 [3.7-17.6]	NA	NA

Data presented as mean ± SD, median [interquartile range] or percentage; PCI percutaneous coronary intervention; CABG coronary artery bypass graft

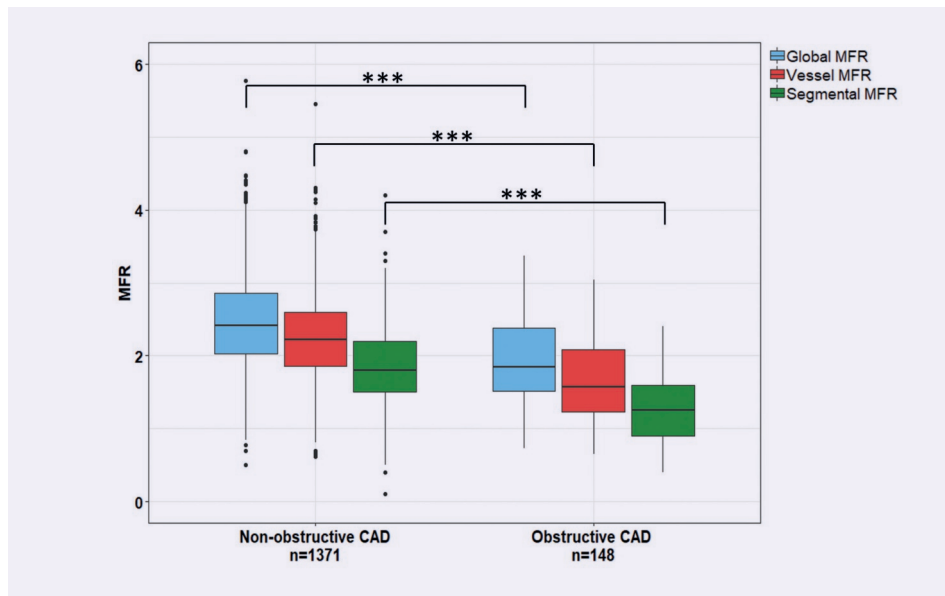


Figure 1. Boxplots showing the global, vessel and segmental MFR for all patients categorized as having non-obstructive CAD or obstructive CAD. Global, vessel and segmental flow values were significantly lower in the obstructive CAD group as compared to the non-obstructive CAD group. \* $p < 0.05$ ; \*\* $p < 0.01$ ; \*\*\* $p < 0.001$ .

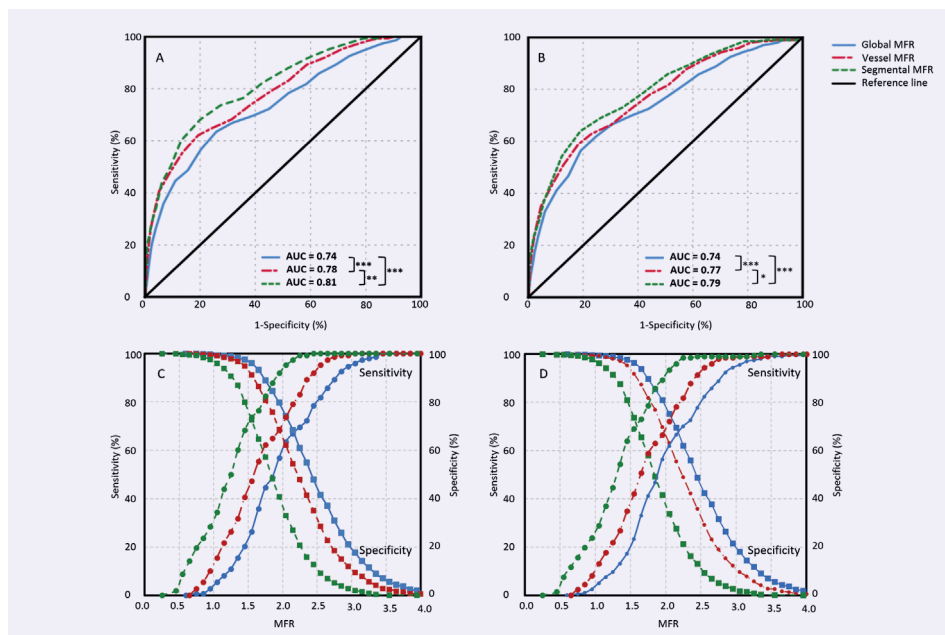


Figure 2. Receiver operating characteristic curves and sensitivity (round markers) and specificity (squared markers) pairs for detecting obstructive CAD (A & C) and obstructive CAD + all-cause mortality (B & D) for global, vessel and segmental MFR. The largest area under the curve was found for segmental MFR. \* $p < 0.05$ ; \*\* $p < 0.01$ ; \*\*\* $p < 0.001$ .



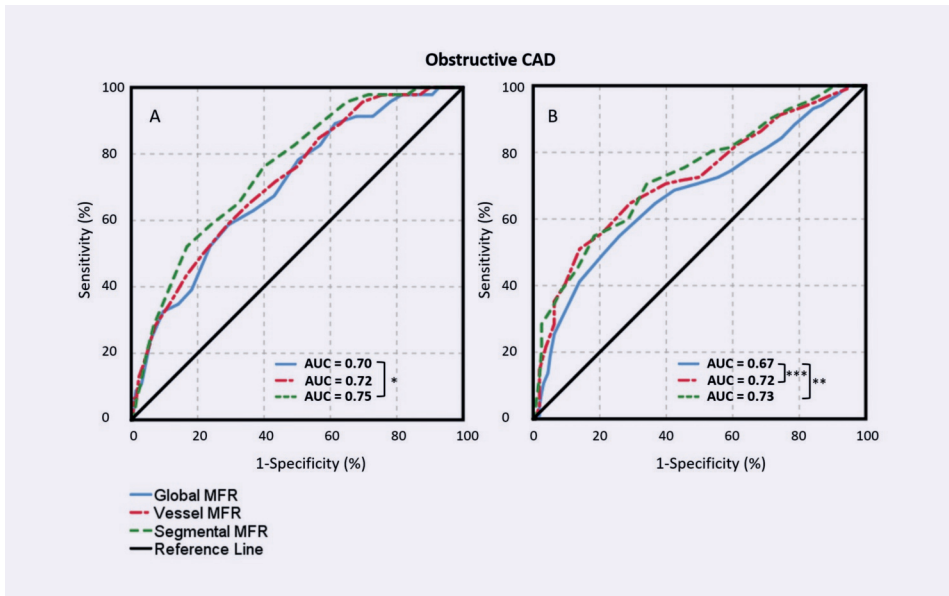


Figure 3. Receiver operating characteristic curves for detecting obstructive CAD, in scans classified as normal (A, N=1259) and abnormal (B, N=260) by visual assessment of expert readers, for global, vessel and segmental MFR. The largest area under the curve was found for segmental MFR. \* $p < 0.05$ ; \*\* $p < 0.01$ ; \*\*\* $p < 0.001$ .

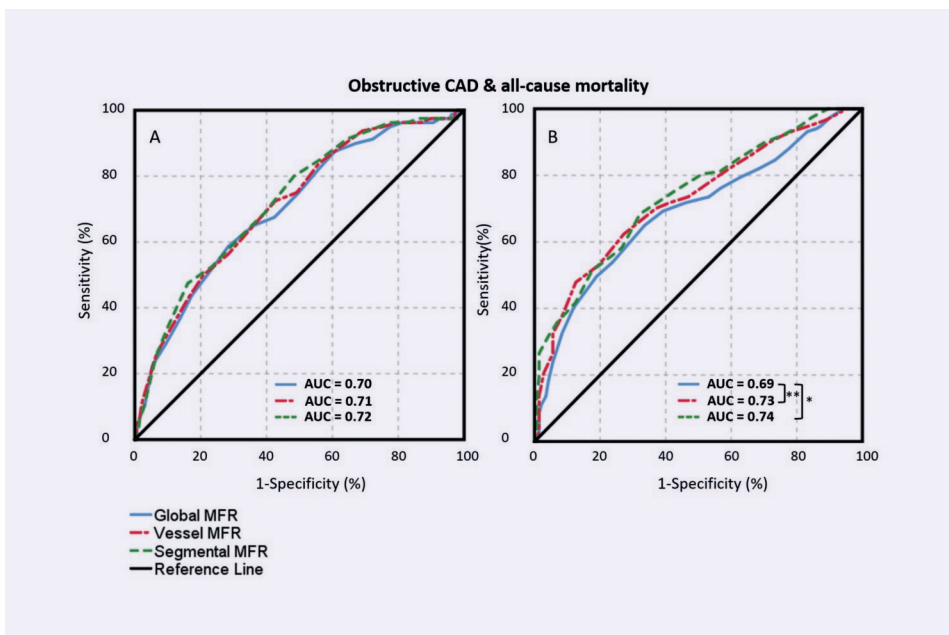


Figure 4. Receiver operating characteristic curves for detecting obstructive CAD + all-cause mortality, in scans classified as normal (A N=1259) and abnormal (B, N=260) by visual assessment of expert readers, for global, vessel and segmental MFR. The largest area under the curve was found for segmental MFR. \* $p < 0.05$ ; \*\* $p < 0.01$ ; \*\*\* $p < 0.001$ .

## DISCUSSION

In this study we compared the diagnostic value of regional with global MFR measurements in Rb-82 PET using oCAD as primary endpoint. The patients classified as having oCAD had a lower global MFR, lower vessel MFR and lower segmental MFR as compared to the non-oCAD patients ( $p < 0.001$ ). We showed that segmental MFR resulted in an improved detection of oCAD as compared to global MFR independent of the visual assessment.

Several study groups investigated the value of blood flow measurements with PET in the detection of oCAD, but none compared regional to global MFR measurement using Rb-82 PET. Mc Ardle et al. performed a meta-analysis of the diagnostic accuracy of relative Rb-82 PET perfusion imaging in the diagnosis and prognosis of patients with known or suspected oCAD<sup>1</sup>. They pooled the data from 15 studies resulting in a ROC curve with an AUC of 0.95. Our AUC of segmental MFR and global MFR of respectively 0.81 and 0.74 are relatively low as compared to their reported AUC of 0.95. However, we only used quantitative flow measurements in computing the ROC curves, whereas Mc Ardle et al. assessed relative Rb-82 PET MPI. Ziadi et al. reported the added value of regional MFR in patients with known or suspected oCAD as a sub-analysis<sup>3</sup>. They found an increased major adverse cardiac event rate for patients with a normal global MFR but abnormal regional MFR in one of the vascular territories as compared to patients with normal MFR in all vascular territories. As it is well known that MFR provides valuable additional information to relative perfusion imaging in Rb-82 PET<sup>2-7</sup>, the combination of visual assessment and quantitative flow measurements using Rb-82 PET would likely improve our AUCs. In addition, the study of Fiechter et al. determined the added value of MFR to relative MPI using nitrogen-13 ammonia PET for patients with suspected oCAD<sup>12</sup>. For the combined interpretation of relative images and MFR, patients with abnormal relative perfusion MPI were classified as abnormal regardless of MFR. Patients with normal relative MPI findings but abnormal MFR were reclassified from normal to abnormal. They found that the accuracy in the detection of oCAD improved from 79% to 89% after adding MFR to the visual assessment. However, they did not account for the added value of high MFR values in patients with visual abnormal scans as shown by Murthy et al.<sup>2</sup>. Moreover, with O-15 H<sub>2</sub>O PET the use of regional MFR is already part of the clinical routine and assessed in voxels presented in the 17-segments model of the myocardium<sup>8</sup>.

This study had several limitations that should be recognized. First, our primary endpoint, oCAD, was based on epicardial stenosis visible using ICA. In our study, patients without oCAD but with a decreased MFR due to microvascular disease (MVD) were categorized as non-oCAD which reduces the accuracy of MFR in detecting oCAD<sup>13</sup>. If we used CAD instead of oCAD on ICA as endpoint, these patients would probably be correctly diagnosed using MFR, possibly resulting in improved ROC curves but our conclusion would likely not change. Despite our findings that regional MFR improves the diagnostic value of Rb-82 PET as compared to global MFR, there still might be a role for global MFR: it may be used to identify MVD<sup>14, 15</sup>. Yet low global MFR values are generally due to low regional MFR values. Hence regional MFR might be suitable to identify coronary microvascular dysfunction as well.

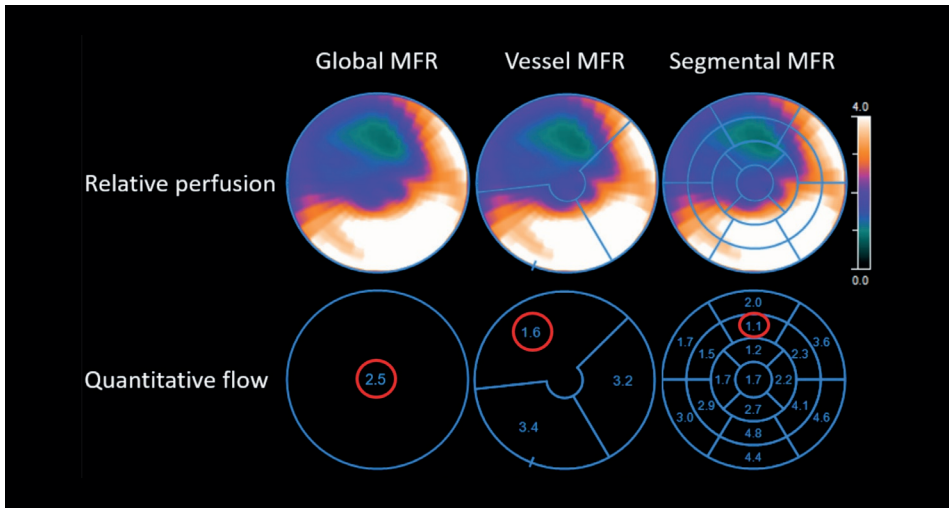


**Figure 5.** Example of a 65-year old male patient with a BMI of 33 kg/m<sup>2</sup> who suffered from chest pain without prior history of CAD. According to the commonly used myocardial flow reserve (MFR) cut-off values<sup>5</sup> this patient would be classified as low risk (MFR >2.0) for CAD according to the global MFR which is 2.5. However, this patient would be reclassified to intermediate risk (MFR 1.5-2.0) according to the vessel MFR of 1.6 for the LAD territory and reclassified as high risk (MFR <1.5) according to the segmental MFR of 1.1. During invasive coronary angiography, single vessel disease of the proximal LAD with a subtotal stenosis was observed which was followed by PCI.

Second, we did not assess the correlation between regional MFR and the affected coronary territories identified by ICA. Although this could be of interest, there is a wide variability in coronary anatomy making the comparison of the affected coronaries based on ICA with the commonly used 17 myocardial segments frequently inaccurate<sup>16</sup>.

Third, as our study was retrospective, a referral bias may have been introduced as referral for ICA could have been influenced by clinical information and a visual positive Rb-82 PET scan for ischemia or a myocardial infarction, or by a low global MFR. To limit this influence, we choose oCAD as primary endpoint including a median follow-up of 23 months to limit this effect. Furthermore, we expect that correction for this bias would result in regional MFR to be of even greater value as compared to global MFR in the detection of oCAD as the segmental MFR can already be reduced while the global MFR is within a normal range. Therefore, a perfusion deficit can be detected in an earlier stage using the segmental MFR as compared to the global MFR.

Next, we only assessed the diagnostic value of MFR using standardized acquisition and reconstruction parameters and not of stress MBF. There are several studies that report stress MBF being superior to MFR in risk stratification<sup>17-19</sup>, while others report MFR being superior to stress MBF<sup>2, 3, 5, 20, 21</sup>. Although these studies are conflicting, MFR is less affected by technical variations such as reconstruction settings including temporal sampling, kinetic modelling and the software being used as compared to MBF<sup>22-25</sup>.

Therefore, we only focused on MFR. Nevertheless, different technical settings might still influence the ROC curves using MFR. However, we expect that regional MFR still outperforms global MFR as long as acquisition, reconstruction parameters and processing software are standardized.

Finally, we did not assess the performance of qualitative perfusion images combined with quantitative flow values as this was outside the scope of this study. Yet, it would be interesting to study the value of MFR in addition to visual assessment, as this would be in line with current practice. However, such a study is not straight forward as different assumptions and thereby choices need to be made. First, the chosen cut-off value is dependent on the desired sensitivity and specificity. Second, in clinical practice two cut-off values are commonly used; a global MFR  $<1.5$  associated with a high risk on oCAD and a global MFR  $>2.0$  associated with a low risk oCAD<sup>5</sup>, making the interpretation of sensitivity and specificity misleading.

## **NEW KNOWLEDGE GAINED**

In this study, we showed that the use of regional MFR improves the diagnostic value of Rb-82 PET as compared to global MFR. It may lead to a change in risk classification. Hence, routine integration of segmental MFR rather than global MFR in combination with visual assessment of relative MPI scans seems promising when reporting Rb-82 PET images. In addition, the use of regional MFR could improve risk stratification in the detection of oCAD. A reason for the worse performance of global MFR in comparison to regional MFR likely is the compensation of poorly perfused parts by well perfused parts, possibly leading to under diagnosis of significant oCAD. Consequently, altered segmental cut-off values need to be applied to distinguish patients with oCAD from non-oCAD patients, as compared to global MFR cut-off values. Future studies will have to indicate which segmental MFR cut-off values are most suitable for this purpose.

## **CONCLUSIONS**

The diagnostic value of quantitative Rb-82 PET improved when using regional instead of global myocardial flow reserve in the detection of obstructive CAD. We therefore recommend to use the segmental flow reserve values in combination with visual assessment of Rb-82 PET scans.

## REFERENCES

1. Mc Ardle BA, Dowsley TF, deKemp RA, Wells GA, Beanlands RS. Does rubidium-82 PET have superior accuracy to SPECT perfusion imaging for the diagnosis of obstructive coronary disease?: A systematic review and meta-analysis. *J Am Coll Cardiol.* 2012;60:1828-37.
2. Murthy VL, Naya M, Foster CR, Hainer J, Gaber M, Di Carli G, et al. Improved cardiac risk assessment with noninvasive measures of coronary flow reserve. *Circulation.* 2011;124:2215-24.
3. Ziadi MC, deKemp RA, Williams KA, Guo A, Chow BJ, Renaud JM, et al. Impaired myocardial flow reserve on rubidium-82 positron emission tomography imaging predicts adverse outcomes in patients assessed for myocardial ischemia: Cardiac imaging. 2011;58:740-8.
4. Zigray H, Elman S, Cheng RK, Li S, Lee J, Soine L, et al. Patient factors and outcomes associated with discordance between quantitative and qualitative cardiac PET ischemia information. 2021;16:Epub ahead of print doi:10.1371/journal.pone.0246149.
5. Murthy V, Bateman T, Beanlands R, Berman D, Borges-Neto S, Chareonthaitawee P, et al. Clinical quantification of myocardial blood flow using PET: Joint position paper of the SNMMI cardiovascular council and the ASNC. *J Nucl Cardiol.* 2018;25:269-97.
6. Sciagra R, Passeri A, Bucerus J, Verberne HJ, Slart, Riemer H. J. A., Lindner O, et al. Clinical use of quantitative cardiac perfusion PET: Rationale, modalities and possible indications. position paper of the cardiovascular committee of the european association of nuclear medicine (EANM). *Eur J Nucl Med Mol Imaging.* 2016;43:1530-45.
7. Ziadi MC. Myocardial flow reserve (MFR) with positron emission tomography (PET)/computed tomography (CT): Clinical impact in diagnosis and prognosis. *Cardiovasc Diagn Ther.* 2017;7:206-18.
8. Maaniitty T, Knuuti J, Saraste A. 15O-water PET MPI: Current status and future perspectives. *Semin Nucl Med.* 2020;50:238-47.
9. Sciagrà R, Lubberink M, Hyafil F, Saraste A, Slart, Riemer H. J. A, Agostini D, et al. EANM procedural guidelines for PET/CT quantitative myocardial perfusion imaging. *Eur J Nucl Med Mol Imaging.* 2020;Epub ahead of print doi: 10.1007/s00259-020-05046-9.
10. Lortie M, Beanlands R, Yoshinaga K, Klein R, DaSilva J, deKemp R. Quantification of myocardial blood flow with 82Rb dynamic PET imaging. *Eur J Nucl Med Mol Imaging.* 2007;34:1765-74.
11. Yokota S, Mouden M, Ottervanger JP, Engbers E, Jager PL, Timmer JR, et al. Coronary calcium score influences referral for invasive coronary angiography after normal myocardial perfusion SPECT. *J Nucl Cardiol.* 2019;26:602-12.
12. Fiechter M, Ghadri JR, Gebhard C, Fuchs TA, Pazhenkottil AP, Nkoulou RN, et al. Diagnostic value of 13N-ammonia myocardial perfusion PET: Added value of myocardial flow reserve. 2012;53:1230-4.
13. Pelletier-Galarneau M, Dilsizian V. Microvascular angina diagnosed by absolute PET myocardial blood flow quantification. *Curr Cardiol Rep.* 2020;22:1-9.
14. Ziadi MC. Myocardial flow reserve (MFR) with positron emission tomography (PET)/computed tomography (CT): Clinical impact in diagnosis and prognosis. *Cardiovasc Diagn Ther.* 2017;7:206.
15. Camici PG, Rimoldi OE. The clinical value of myocardial blood flow measurement. *J Nucl Med.* 2009;50:1076-87.

16. Javadi MS, Lautamäki R, Merrill J, Voicu C, Epley W, McBride G, et al. Definition of vascular territories on myocardial perfusion images by integration with true coronary anatomy: A hybrid PET/CT analysis. *J Nucl Med.* 2010;51:198-203.
17. Farhad H, Dunet V, Bachelard K, Allenbach G, Kaufmann PA, Prior JO. Added prognostic value of myocardial blood flow quantitation in rubidium-82 positron emission tomography imaging. *Eur Heart J Cardiovasc Imaging.* 2013;14:1203-10.
18. Danad I, Uusitalo V, Kero T, Saraste A, Rajmakers PG, Lammertsma AA, et al. Quantitative assessment of myocardial perfusion in the detection of significant coronary artery disease cutoff values and diagnostic accuracy of quantitative [O-15]H<sub>2</sub>O PET imaging. *J Am Coll Cardiol.* 2014;64:1464-75.
19. Hajjiri MM, Leavitt MB, Zheng H, Spooner AE, Fischman AJ, Gewirtz H. Comparison of positron emission tomography measurement of adenosine-stimulated absolute myocardial blood flow versus relative myocardial tracer content for physiological assessment of coronary artery stenosis severity and location. *JACC Cardiovasc Imaging.* 2009;2:751-8.
20. Patel KK, Spertus JA, Chan PS, Sperry BW, Al Badarin F, Kennedy KF, et al. Myocardial blood flow reserve assessed by positron emission tomography myocardial perfusion imaging identifies patients with a survival benefit from early revascularization. *Eur Heart J.* 2020;41:759-68.
21. Gupta A, Taqueti VR, van de Hoef, Tim P, Bajaj NS, Bravo PE, Murthy VL, et al. Integrated noninvasive physiological assessment of coronary circulatory function and impact on cardiovascular mortality in patients with stable coronary artery disease. *Circulation.* 2017;136:2325-36.
22. Koenders SS, van Dijk JD, Jager PL, Mouden M, Tegelaar AG, Slump CH, et al. Effect of temporal sampling protocols on myocardial blood flow measurements using rubidium-82 PET. *J Nucl Cardiol.* 2022;29:1729-41.
23. Murthy VL, Lee BC, Sitek A, Naya M, Moody J, Polavarapu V, et al. Comparison and prognostic validation of multiple methods of quantification of myocardial blood flow with 82Rb PET. *J Nucl Med.* 2014;55:1952-8.
24. Tahari AK, Lee A, Rajaram M, Fukushima K, Lodge MA, Lee BC, et al. Absolute myocardial flow quantification with (82)rb PET/CT: Comparison of different software packages and methods. *Eur J Nucl Med Mol Imaging.* 2014;41:126-35.
25. Armstrong I, Tonge C, Arumugam P. Impact of point spread function modeling and time-of-flight on myocardial blood flow and myocardial flow reserve measurements for rubidium-82 cardiac PET. *J Nucl Cardiol.* 2014;21:467-74.







# PATIENT-TAILORED RISK ASSESSMENT OF OBSTRUCTIVE CORONARY ARTERY DISEASE

USING RUBIDIUM-82 PET-BASED  
MYOCARDIAL FLOW QUANTIFICATION WITH  
VISUAL INTERPRETATION

## Authors

S.S. Koenders<sup>1,4</sup>

J.A. van Dalen<sup>2</sup>

P.L. Jager<sup>1</sup>

M. Mouden<sup>3</sup>

C.H. Slump<sup>4</sup>

J.D. van Dijk<sup>1</sup>

## Author Affiliations

1. Department of Nuclear Medicine, Isala Hospital, Zwolle, The Netherlands
2. Department of Medical Physics, Isala Hospital, Zwolle, The Netherlands
3. Department of Cardiology, Isala Hospital, Zwolle, The Netherlands
4. Technical Medical Centre, University of Twente, Enschede, the Netherlands

## Submitted to

Journal of Nuclear Cardiology



## ABSTRACT

### Introduction

Our aim was to estimate the probability of obstructive CAD (oCAD) for an individual patient as a function of the myocardial flow reserve (MFR) measured with Rubidium-82 (Rb-82) PET in patients with a visually normal scan or abnormal scan.

### Materials and Methods

We included 1519 patients without a prior history of CAD referred for rest-stress Rb-82 PET/CT. All images were visually assessed by two experts and classified as normal or abnormal. We estimated the probability of oCAD for visually normal and abnormal scans as function of MFR. The primary endpoint was oCAD on invasive coronary angiography.

### Results

1259 scans were classified as normal and 260 as abnormal. For the normal scans, the probability of oCAD increased exponentially from <1% to 10% when segmental MFR decreased from 2.1 to 1.3. For abnormal scans, the probability increased from 10% to >70% when segmental MFR decreased from 2.7 to 0.7.

### Conclusion

Patients with >10% risk of oCAD can be distinguished from patients with <10% risk based on visual PET interpretation only. However, there is a strong dependence of MFR on patient's individual risk of oCAD. Our results provide a patient-tailored risk assessment based on both visual interpretation and MFR which may affect treatment strategy.

### Keywords

Myocardial blood flow; PET myocardial perfusion imaging; 82Rb; MBF; segmental MFR.

## INTRODUCTION

The use of myocardial blood flow (MBF) quantification using Rubidium-82 (Rb-82) in myocardial perfusion imaging (MPI) with positron emission tomography (PET) is rapidly increasing<sup>1-3</sup>. This is mainly caused by the availability of Strontium-82/Rb-82 generators and the better accuracy of PET in comparison to SPECT imaging<sup>4, 5</sup>. Global myocardial flow reserve (MFR) values provide incremental prognostic value over visual interpretation of the PET scans and help to better identify patients at risk of cardiac events<sup>6, 7</sup>. To prevent the development of cardiac events, a patient-tailored risk assessment of obstructive CAD (oCAD) is essential for choosing an appropriate treatment strategy. PET-based MFR in combination with visual assessment can be used for this purpose as in clinical practice PET is used to assess the presence, extent and functional importance of oCAD<sup>7, 8</sup>. However, in assessing patient's risk of oCAD it is unclear how MFR should be combined with visual assessment, especially when they are discordant. How should the readers interpret patients with a normal scan and low MFR, or patients with an abnormal scan but high MFR? Hence, our aim was to estimate the probability of oCAD for an individual patient as a function of the MFR in patients with a visually normal scan as well as in patients with a visually abnormal scan.

## MATERIALS AND METHODS

### Study population

We retrospectively included 1519 patients referred for rest and regadenoson-induced stress Rb-82 PET/CT (GE Discovery 690, GE Healthcare) without a prior history of CAD and of whom at least one-year follow-up was available. As this study was retrospective, approval by the medical ethics committee was therefore not required according to Dutch law. Nevertheless, all patients provided written informed consent for the use of their data for research purposes.

### Patient preparation, data acquisition and reconstruction

All subjects were asked to refrain from caffeine containing substances for 24 hours and to discontinue dipyridamole containing medication for 48 hours prior to imaging. All patients underwent a rest scan followed by a regadenoson-induced stress scan. The PET/CT acquisition and reconstruction protocol have been described previously<sup>9</sup>. In short, we acquired a low-dose CT scan prior to MPI during free-breathing to provide an attenuation map of the chest. PET list-mode data were acquired in rest during 7 minutes directly after administration of 740 MBq Rb-82. Ten minutes after the first activity bolus, we induced pharmacological stress by administering 400 µg (5 mL) of regadenoson over 10 seconds. Subsequently, a second dose of 740 MBq Rb-82 was administered, followed by another PET acquisition. Attenuation correction was applied to all data on the PET system after semi-automatic registration of CT and PET data. We reconstructed the dynamic PET datasets using 26 time frames (12x5s, 6x10s, 4x20s and 4x40s). Static rest and stress images were reconstructed from PET data acquired between 2:30 and 7:00 minutes after Rb-82 administration.

### Data analysis

We used Corridor4DM (v2016.02.64) software to post-process the dynamic images<sup>10</sup>. All static Rb-82 PET images were visually assessed by two expert readers and classified as normal or as abnormal, where abnormal was defined as images showing a reversible and/or irreversible perfusion defect. The one-tissue compartment model of Lortie et al.<sup>11</sup> was used to calculate the MBF from the time activity curves (TACs) of the image-derived left ventricle blood pool and the myocardium. The dynamic images were visually inspected for the presence of myocardial creep and manually corrected if necessary<sup>9</sup>. MFR was calculated as the ratio of stress MBF to rest MBF. In our previous study, we showed the added diagnostic value for regional MFR over global MFR<sup>12</sup>. In addition to the global MFR (globMFR), we therefore also determined MFR in each of the 17 left ventricular myocardial segments<sup>12</sup>. We defined regional MFR as the lowest flow reserve in all 17 segments (segMFR).

Next, we estimated the patient's probability of having oCAD for visually normal and abnormal scans as a function of both globMFR and segmMFR. To obtain proper statistics for calculating the probability of oCAD we divided patients into quintiles based on globMFR and segmMFR for both the patient group with visually normal scans and for the patient group with visually abnormal scans. For each quintile we calculated the mean globMFR and mean segmMFR, and corresponding standard error. Next, we fitted the mean MFR of the quintiles to the probability of oCAD ( $P_{\text{oCAD}}$ ) using the exponential function:

$$P_{\text{oCAD}} = a \cdot e^{-b \cdot x}$$

where  $x$  is either globMFR or segMFR, and  $a$  and  $b$  are fit parameters.

### Follow-up

Patient follow-up was obtained by use of medical records. Our endpoint was the presence or absence of oCAD, as the purpose of Rb-82 PET is to assess the presence, extent and functional importance of oCAD in order to tailor treatment. Patients were classified as having oCAD if follow-up included either a positive invasive coronary angiography (ICA) during follow-up. A positive ICA was defined by an intermediate or severe stenosis with a fractional flow reserve  $<0.8$  or  $>70\%$  stenosis in the left anterior descending (LAD), left circumflex (LCX) or right coronary artery (RCA), or  $>50\%$  stenosis in the left main coronary artery.

### Statistical analysis

Patient characteristics and continuous variables were expressed as mean  $\pm$  standard deviation (SD) or median [interquartile range] as appropriate. Statistical analysis was performed using IBM SPSS (IBM SPSS Statistics for Windows, Version 26.0. Armonk, NY: IBM Corp). To assess differences between patient characteristics with visually normal and abnormal scans, the t-test, Mann–Whitney U test or  $\chi^2$ -test were performed. To determine goodness of fit between the probability function and our MFR data we used  $\chi^2$ . The level of statistical significance was set to 0.05 for all statistical analyses.

Table 1. Baseline characteristics of the patient population (N=1519).

Characteristic	Visual normal (N=1259)	Visual abnormal (N=260)	p values
Age (years)	66 ± 11	69 ± 10	<0.001
Male gender (%)	48	65	<0.001
Weight (kg)	88 ± 20	90 ± 19	0.07
Height (cm)	173 ± 10	175 ± 10	0.01
BMI (kg/m <sup>2</sup> )	29 ± 6	30 ± 6	0.47
Current smoking (%)	13	13	0.99
Hypertension (%)	63	63	0.98
Dyslipidaemia (%)	42	45	0.42
Diabetes (%)	20	23	0.34
Family history (%)	52	48	0.22
Segmental MFR	1.8 [1.5-2.2]	1.4 [1.0-1.8]	<0.001
Global MFR	2.4 [2.1-2.9]	2.0 [1.7-2.6]	<0.001
Time to follow-up (months)	23 [18-28]	23 [18-26]	0.18
Obstructive CAD (%)	3.7 (46)	39 (102)	<0.001
PCI during follow-up (%)	2.2 (28)	20 (52)	<0.001
CABG during follow-up (%)	1.6 (20)	16 (41)	<0.001
All-cause mortality (%)	2.7 (34)	5.8 (15)	0.01

Data are presented as mean ± SD, median [interquartile range] or percentage; PCI percutaneous coronary intervention; CABG coronary artery bypass graft

## RESULTS

Of all 1519 patients, 83% (1259) had a scan which was classified as normal and the remaining patients had a scan which was classified as abnormal. These two groups did not differ in weight, body mass index (BMI) and the risk factors smoking, hypertension, dyslipidaemia, diabetes and family history ( $p \geq 0.07$ ), as shown in Table 1. Yet patients with abnormal scans were older, taller and more often male ( $p \leq 0.01$ ). The median follow-up was 23 months [interquartile range: 18 - 27].

Of the 1259 patients with normal scans, 3.7% (46) had oCAD during follow-up. Of the 260 patients with visually abnormal scans, 39% (102) had oCAD during follow-up. We found lower segMFR (1.4 vs. 1.8) and globMFR (2.0 vs. 2.4) in patients with visually abnormal scans than in patients with visually normal scans ( $p < 0.001$ ).

Combining *segmental* MFR with visual scan results, the patient's probability of having oCAD increased with decreasing segMFR for both visually normal and abnormal scans, as shown in Figure 1. For the

normal scans, the probability of oCAD increased from <1% in patients with a segMFR  $\geq 2.1$  to 10% in patients with a segMFR of 1.3. For visually abnormal scans, the probability of oCAD increased from 10% in patients with a segMFR of 2.7 to >70% for the patient group with a segMFR of 0.7. The probability of oCAD can be described for visually normal scans by  $P_{\text{oCAD}} = 2.02 \cdot e^{-2.42 \cdot \text{segMFR}}$  ( $R^2=0.94$ ,  $p=0.37$ ) and for visually abnormal scans by  $P_{\text{oCAD}} = 1.22 \cdot e^{-0.89 \cdot \text{segMFR}}$  ( $R^2=0.94$ ,  $p=0.25$ ).

When combining *global* MFR with visual assessment, we also observed an increase in the probability of oCAD with decreasing globMFR for both visually normal and abnormal Rb-82 PET scans, as shown in Figure 2. The probability of oCAD increased from 0.8% in patients with a global MFR of 3.4 to 8% in patients with a global MFR of 1.7. For visually abnormal scans, the probability of oCAD increased from 27% in patients with a global MFR of 3.1 to 67% in patients with a global MFR of 1.3. The probability of oCAD can be described for visually normal scans by  $P_{\text{oCAD}} = 0.68 \cdot e^{-1.27 \cdot \text{globMFR}}$  ( $R^2=0.98$ ,  $p=0.95$ ) and for visually abnormal scans by  $P_{\text{oCAD}} = 1.03 \cdot e^{-0.49 \cdot \text{globMFR}}$  ( $R^2=0.70$ ,  $p=0.04$ ).

## DISCUSSION

In this study we estimated the patient's probability of having oCAD based on the combination of visual assessment of Rb-82 PET scans and MFR values. Although a visual interpretation seems to be sufficient to discriminate patients with a probability >10% from patients with a probability <10% patients, our study showed that MFR can be used for a more patient-tailored risk assessment, as the probability of an individual patient having oCAD strongly depends on MFR (as shown in Figures 1 and 2). Combining MFR measurements with visual interpretation of Rb-82 PET to estimate patient's risk of having oCAD may therefore impact the treatment strategy.

Our results are in line with a previous study performed by Murthy et al. who reported that the global MFR provides prognostic information in addition to only visual assessment<sup>6</sup>. Murthy et al. used cardiac mortality as primary endpoint, instead of oCAD as chosen in this study, and included a large number of patients with a prior history of CAD. They found that patients with a visually normal Rb-82 PET scan and low global MFR (<1.5) had a higher annualized mortality rate (3.6%) as compared to patients with visually abnormal scans and high global MFR (1%). These results are in line with the ones presented in this study as the probability on oCAD for a normal interpreted scan with low globMFR or segMFR exceeded that of an abnormal scan with high globMFR or segMFR.

This study has several limitations. First, we only included patients without prior history of CAD. Therefore, the derived probability of a patient having oCAD might not be generalizable to patients with a prior history of CAD. However, as mentioned above, Murthy et al. showed results that are in line with ours while including a large number of patients with a prior history of oCAD<sup>6</sup>. We expect that the probability of oCAD also increases with decreasing (global or segmental) MFR and decreases with increasing (global or segmental MFR) for both visually normal and abnormal Rb-82 PET scans in patients with a prior history.

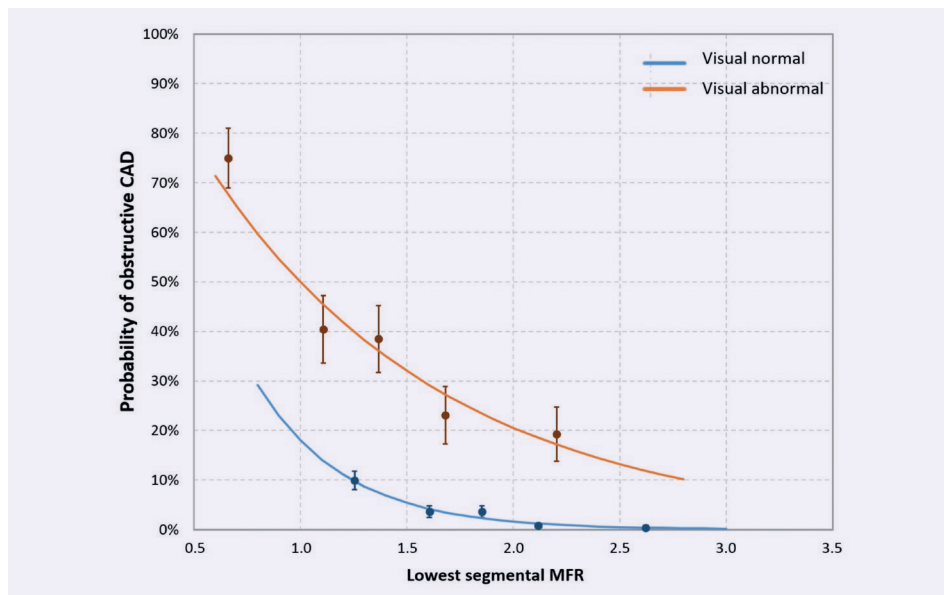


Figure 1. Plot of the mean of each quintile (dot with error bars) and the lines showing the patient's probability (solid line) of having obstructive CAD for visually normal (blue) and abnormal (orange) scans combined with the lowest measured segmental MFR. The probability of obstructive CAD can be described for normal scans by  $P_{\text{ocAD}} = 2.02 \cdot e^{-2.42 \cdot \text{segMFR}}$  ( $R^2=0.94$ ) and for abnormal scans by  $P_{\text{ocAD}} = 1.22 \cdot e^{-0.89 \cdot \text{segMFR}}$  ( $R^2=0.94$ ).

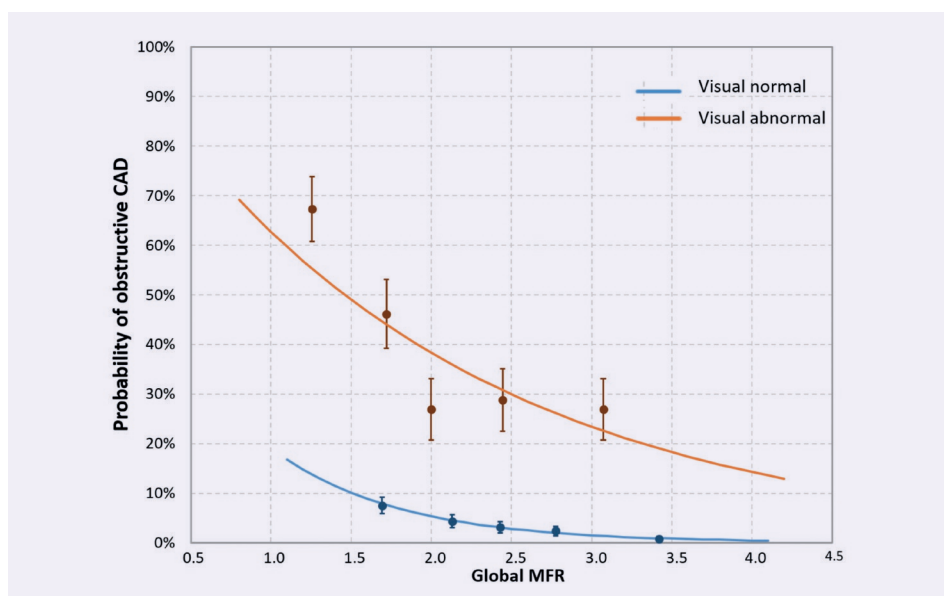


Figure 2. Plot of the mean of each quintile (dot with standard error bars) and the lines showing the patient's probability (solid line) of having obstructive CAD for visually normal (blue) and abnormal (orange) scans combined with the global MFR. The probability of obstructive CAD can be described for normal scans by  $P_{\text{ocAD}} = 0.68 \cdot e^{-1.27 \cdot \text{globMFR}}$  ( $R^2=0.98$ ) and for abnormal scans by  $P_{\text{ocAD}} = 1.03 \cdot e^{-0.49 \cdot \text{globMFR}}$  ( $R^2=0.70$ ).



Secondly, the probability of oCAD as a function of (global or segmental) MFR as derived in our study may not be similar for other centers. Both patient population and acquisition, reconstruction and post-processing protocols may differ which can result in different MFR values<sup>13-16</sup> and hence in a different probability function. However, we do not expect its shape to be different: patient's probability to have oCAD is likely to depend strongly on MFR, for both visually normal and abnormal scans. Ideally, each center should derive its own relation between MFR and probability of oCAD.

Finally, the retrospective study design may have led to some bias in our study population, as only patients who were clinically indicated underwent ICA. We classified patients as having oCAD if follow-up included either a conclusive ICA for oCAD or a revascularization during follow-up. Inherently, we might have missed patients with oCAD as not all were referred for ICA and some of the deceased patients (49) may have died from oCAD. This bias may have led to an underestimation of patients with oCAD and, consequently, to an underestimation of the probability of oCAD. However, we do not expect that the shape of the derived probability functions will change strongly due to this bias.

## CLINICAL IMPLICATIONS

In clinical practice, Rb-82 PET-based MFR in combination with visual assessment is used to diagnose oCAD as recently recommended by guidelines<sup>7,8</sup>. However, in diagnosing oCAD it is unclear how visual assessment can be combined best with MFR, especially when MFR is discrepant from the qualitative interpretation. We provided a probability function that can be used in clinical practice and is of particular value for patients with a normal PET scan and low MFR and vice versa. In these cases, the probability of a patient having oCAD is altered when compared to the probability when solely using visual or MFR assessment, possibly affecting treatment strategy. Hence, estimating patient's risk on oCAD should be based on both MFR and visual interpretation of Rb-82 PET.

In clinical practice both global and regional MFR values can be calculated and be used in diagnosing oCAD. In agreement with our previous study where we showed an improved diagnostic value using regional instead of global MFR in the detection of oCAD<sup>12</sup>, we observed a stronger dependency when using regional MFR in the prediction of oCAD as indicated by the higher b values of the fits (2.42 versus 1.27 for visually normal scans, and 0.89 versus 0.49 for visually abnormal scans), illustrated in Figures 1 and 2. Therefore, we recommend to combine segmental over global flow values with visual assessment of Rb-82 PET scans.

Ideally, other centers should recreate the probability function for their own settings as absolute values may differ from ours due to difference in patient population, PET scanner, acquisition, reconstruction and post-processing techniques<sup>13-16</sup>. However, we do expect to see a similar shape of this function with a strong dependence on MFR, for both visually normal and abnormal scans.

## CONCLUSION

In estimating the probability of a patient having oCAD using Rb-82 PET, both visual interpretation and MFR measurements are essential. Patients with a probability >10% can be distinguished from patients with a probability <10% based on visual interpretation only. However, there is a strong dependence of MFR on patient's individual probability of having oCAD: these probabilities may range from <1% to >70%. Our results provide a patient-tailored risk assessment based on both visual interpretation and MFR which may affect treatment strategy.

## REFERENCES

1. Saraste A, Kajander S, Han C, Nesterov SV, Knuuti J. PET: Is myocardial flow quantification a clinical reality? *J Nucl Cardiol.* 2012;19:1044-59.
2. deKemp RA, Yoshinaga K, Beanlands RSB. Will 3-dimensional PET-CT enable the routine quantification of myocardial blood flow? *J Nucl Cardiol.* 2007;14:380-97.
3. Sciagra R, Passeri A, Bucierius J, Verberne HJ, Slart RHJA, Lindner O, et al. Clinical use of quantitative cardiac perfusion PET: Rationale, modalities and possible indications. position paper of the cardiovascular committee of the european association of nuclear medicine (EANM). *Eur J Nucl Med Mol Imaging.* 2016;43:1530-45.
4. Jaarsma C, Leiner T, Bekkers SC, Crijns HJ, Wildberger JE, Nagel E, et al. Diagnostic performance of noninvasive myocardial perfusion imaging using single-photon emission computed tomography, cardiac magnetic resonance, and positron emission tomography imaging for the detection of obstructive coronary artery disease A meta-analysis. *JACC.* 2012;59:1719-28.
5. Knuuti J, Ballo H, Juarez-Orozco LE, Saraste A, Kolh P, Rutjes AWS, et al. The performance of non-invasive tests to rule-in and rule-out significant coronary artery stenosis in patients with stable angina: A meta-analysis focused on post-test disease probability. *Eur Heart J.* 2018;39:3322-30.
6. Murthy VL, Naya M, Foster CR, Hainer J, Gaber M, Di Carli G, et al. Improved cardiac risk assessment with noninvasive measures of coronary flow reserve. *Circulation.* 2011;124:2215-24.
7. Blankstein R, Shaw LJ, Gulati M, Atalay MK, Bax J, Calnon DA, et al. Implications of the 2021 AHA/ACC/ASE/CHEST/SAEM/SCCT/SCMR chest pain guideline for cardiovascular imaging: A multisociety viewpoint. *JACC.* 2022;15:912-26.
8. Murthy V, Bateman T, Beanlands R, Berman D, Borges-Neto S, Chareonthaitawee P, et al. Clinical quantification of myocardial blood flow using PET: Joint position paper of the SNMMI cardiovascular council and the ASNC. *J Nucl Cardiol.* 2018;25:269-97.
9. Koenders SS, van Dijk JD, Jager PL, Ottervanger JP, Slump CH, van Dalen JA. Impact of regadenoson-induced myocardial creep on dynamic rubidium-82 PET myocardial blood flow quantification. *J Nucl Cardiol.* 2019;26:719-28.
10. Koenders SS, van Dijk JD, Jager PL, Ottervanger JP, Slump CH, van Dalen JA. How to detect and correct myocardial creep in myocardial perfusion imaging using rubidium-82 PET? *J Nucl Cardiol.* 2019;26:729-34.
11. Lortie M, Beanlands R, Yoshinaga K, Klein R, DaSilva J, deKemp R. Quantification of myocardial blood flow with 82Rb dynamic PET imaging. *Eur J Nucl Med Mol Imaging.* 2007;34:1765-74.
12. Koenders SS, van Dalen JA, Jager PL, Mouden M, Slump CH, van Dijk JD. Diagnostic value of regional myocardial flow reserve measurements using rubidium-82 PET. *Int J Cardiovasc Imaging.* 2022;Epub ahead of print doi:10.1007/s10554-022-02644-6.
13. Koenders SS, van Dijk JD, Jager PL, Mouden M, Tegelaar AG, Slump CH, et al. Effect of temporal sampling protocols on myocardial blood flow measurements using rubidium-82 PET. *J Nucl Cardiol.* 2022;29:1729-41.

14. Murthy VL, Lee BC, Sitek A, Naya M, Moody J, Polavarapu V, et al. Comparison and prognostic validation of multiple methods of quantification of myocardial blood flow with  $^{82}\text{Rb}$  PET. *J Nucl Med.* 2014;55:1952-8.
15. Tahari AK, Lee A, Rajaram M, Fukushima K, Lodge MA, Lee BC, et al. Absolute myocardial flow quantification with  $(^{82}\text{Rb})$  PET/CT: Comparison of different software packages and methods. *Eur J Nucl Med Mol Imaging.* 2014;41:126-35.
16. Armstrong I, Tonge C, Arumugam P. Impact of point spread function modeling and time-of-flight on myocardial blood flow and myocardial flow reserve measurements for rubidium-82 cardiac PET. *J Nucl Cardiol.* 2014;21:467-74.





# MACHINE LEARNING BASED MODEL TO DIAGNOSE OBSTRUCTIVE CORONARY ARTERY DISEASE

USING CALCIUM SCORING, PET IMAGING  
AND CLINICAL DATA

## Authors

J.A. van Dalen<sup>1</sup>

S.S. Koenders<sup>2,5</sup>

R.J. Metselaar<sup>2,5</sup>

B.N. Vendel<sup>2</sup>

D.J. Slotman<sup>3</sup>

M. Mouden<sup>4</sup>

C.H. Slump<sup>5</sup>

J.D. van Dijk<sup>2</sup>

## Author Affiliations

1. Department of Medical Physics, Isala Hospital, Zwolle, The Netherlands
2. Department of Nuclear Medicine, Isala Hospital, Zwolle, The Netherlands
3. Department of Radiology, Isala Hospital, Zwolle, The Netherlands
4. Department of Cardiology, Isala Hospital, Zwolle, The Netherlands
5. Technical Medical Centre, University of Twente, Enschede, the Netherlands

## Submitted to

Journal of Nuclear Cardiology





## ABSTRACT

### Introduction

Accurate risk stratification in patients with suspected stable coronary artery disease is essential for choosing an appropriate treatment strategy. Our aim was to develop and validate a machine learning (ML) based model to diagnose obstructive CAD (oCAD).

### Method

We retrospectively have included 1007 patients without a prior history of oCAD who underwent CT-based calcium scoring (CACS) and a Rubidium-82 PET scan. The entire dataset was split 4:1 into a training and test dataset. An ML model was developed on the training set using 5-fold stratified cross-validation. The test dataset was used to compare the performance of expert readers to the model. The primary endpoint was oCAD on invasive coronary angiography (ICA).

### Results

ROC curve analysis showed an AUC of 0.92 for the training dataset and 0.89 for the test dataset. The ML model showed no significant differences as compared to the expert readers ( $p \geq 0.03$ ) in accuracy (89% vs. 88%), sensitivity (68% vs. 69%) and specificity (92% vs. 90%).

### Conclusion

The ML model resulted in a similar diagnostic performance as compared to expert readers, and may be deployed as a risk stratification tool. This study showed that utilization of ML is promising in the diagnosis of obstructive CAD.

### Keywords

Machine learning; PET myocardial perfusion imaging; coronary artery disease.

## INTRODUCTION

Invasive coronary angiography (ICA) in combination with functional flow measurements is an important procedure in diagnosing obstructive coronary artery disease (oCAD). However, it is associated with inherent risks of serious complications and accompanied by considerable costs, relatively high radiation exposure and patient discomfort<sup>1,2</sup>. In patients with low to intermediate pre-test likelihood for oCAD, non-invasive imaging, such as computed tomography (CT) based calcium scoring (CACS), CT coronary angiography (CCTA) and cardiac positron emission tomography (PET) is recommended as gatekeeper for ICA<sup>1,3,4</sup>.

After non-invasive imaging, cardiologists combine the imaging data, clinical data and type of complaints to estimate a post-test likelihood and, if needed, determine a specific treatment strategy. Typically, they include classical risk factors for oCAD such as age, body mass index, smoking, hypertension, cholesterol, diabetes, medical history and family history, and medication usage. In the end, this may include tens of different features which makes the cardiologist's ability to interpret and integrate all these data into one post-test likelihood not straight forward. Artificial intelligence (AI) applications can help to improve diagnosis of patients with oCAD by combining all available information<sup>5,6</sup>. These applications may reduce costs, save time, can help training or starting physicians and increase diagnostic performance. In particular, machine learning (ML) models have been shown suitable to assess many features and are capable of modelling complex non-linear relations between these features, to finally result in an accurate diagnosis and to guide physicians in the treatment strategy to choose<sup>7,8</sup>.

In order to integrate AI applications into clinical practice it is appropriate that these applications result in a diagnostic performance at least equal to that of an experienced physician. Previous studies have shown the potential of integrating imaging derived features with clinical data in ML-based risk prediction models<sup>7,8</sup>. To our knowledge, a study applying ML to predict oCAD based on clinical data, CACS and PET imaging, has not been performed yet.

Our aim was to develop and validate a ML-based model to diagnose oCAD in patients without prior history of CAD, based on clinical data, medication and imaging data, including CT-based CACS and Rubidium-82 (Rb-82) PET. In addition, we compared the performance of this ML model to that of expert imaging physicians.

## MATERIALS AND METHODS

### Study population

We retrospectively have included a consecutive cohort of 1007 patients who underwent CT-based CACS and rest and regadenoson-induced stress Rb-82 PET (Discovery 690, GE Healthcare) between 1 May 2017 and 1 February 2019. All included patients had no prior history of CAD which was defined as

prior myocardial infarction, percutaneous coronary intervention (PCI) or coronary artery bypass grafting (CABG). Information about the patients' history, patients' characteristics and clinical data were obtained by review of medical records. As this study was retrospective, approval by the medical ethics committee was therefore not required according to Dutch law. Nevertheless, all patients provided written informed consent for the use of their data for research purposes.

### **Image acquisition and reconstruction**

Prior to myocardial perfusion imaging (MPI), a low-dose CT scan was acquired during free-breathing to provide an attenuation map of the chest. This scan was made using 0.8 s rotation time, pitch of 0.97, collimation of 32x0.625 mm, tube voltage of 120 kV, and a tube current of 10 mA. Images were reconstructed using a matrix of 512 x 512 and a 5 mm slice thickness. Next, 740 MBq Rb-82 was administered intravenously with a flow rate of 50 mL/min using a Sr-82/Rb-82 generator (CardioGen-82, Bracco Diagnostics Inc.). Ten minutes after the first elution, we induced pharmacological stress by administering 400 µg (5 mL) of Regadenoson over 10 seconds. After a 5 mL saline flush (NaCl 0.9%), we administered a second dose of 740 MBq Rb-82. Seven-minute PET list-mode acquisitions were acquired after both Rb-82 administrations. Attenuation correction was applied to all data on the PET system after manual rigid registration of CT and PET data.

CT-based CACS scans were performed using a 64-slice CT scanner (Light-Speed VCT XT, GE Healthcare). An unenhanced ECG-gated scan was obtained prospectively, triggered at 75% of the R–R interval by using the following scanning parameters: 2.5 mm slice thickness; 330 ms gantry rotation time; tube voltage of 120 kV; and a tube current of 125–250mA, depending on patient's size.

Static and ECG-gated rest and stress PET images (Discovery 690, GE Healthcare) were obtained from data acquired from 2:30 to 7:00 minutes after Rb-82 administration. The voxel size was 3.3 x 3.3 x 3.3 mm<sup>3</sup>. The dynamic PET datasets were reconstructed using 26 time-frames (12x5 s, 6x10 s, 4x20 s and 4x40 s) with default settings as recommended by the manufacturer using 3D iterative reconstruction using 2 iterations and 24 subsets, while correcting for decay, attenuation, scatter and random coincidences, and dead time effects. Neither time-of-flight information or resolution modeling was used for reconstruction of the dynamic PET datasets.

### **Data processing**

CACS was obtained per vessel (left anterior descending (LAD), left circumflex (LCX) and right coronary artery (RCA)) according to the standard Agatston criteria<sup>9</sup>. The reconstructed dynamic PET scans were post-processed using Corridor4DM software (Invia medical imaging solutions, v2015.02.64) in combination with the one-tissue compartment model of Lortie et al. to calculate the myocardial blood flow (MBF)<sup>10</sup>, as also described previously<sup>11</sup>. The MBF was calculated for the myocardium as a whole and for the LAD, LCX and RCA territories, for both stress and rest. The MFR was calculated by dividing the stress MBF by the rest MBF.

To possibly further improve the diagnostic accuracy of the MBF measurements, we also calculated the myocardial perfusion entropy (MPE). MPE can be interpreted as the amount of disorder between the 17-segmental MBF values and can possibly better discriminate ischemic from non-ischemic areas as compared to global or regional MBF values<sup>12</sup>. MPE was calculated using Shannon's equation for entropy<sup>13</sup> with the 17-segmental MFR values as input<sup>12</sup>.

### Follow-up

A reference standard was used to determine the diagnostic value of a ML-based model in the diagnosis of oCAD. As reference standard, we classified patients as having oCAD if follow-up included either a conclusive invasive coronary angiography (ICA) for CAD defined by an intermediate or severe stenosis with a fractional flow reserve <0.8 or >70% stenosis in the LAD, LCX or RCA, or >50% stenosis in the left main coronary artery on ICA or a revascularization during follow-up<sup>14</sup>. In addition, a composite of oCAD and occurrence of all-cause mortality was used as a reference.

### Machine learning

We developed a machine learning model using the extreme gradient boosting (XGBoost) library (v1.4.2) to diagnose oCAD in patients without prior history of CAD, based on clinical data, medication and imaging data, including CAC-score and Rb-82 PET<sup>15</sup>. The XGBoost model implements the gradient boosting decision tree model and was carried out in Python from the Scikit-Learn library (v0.24.2) for binary classification of the presence of oCAD<sup>16</sup>. The dataset was randomly split into a training and test set with a 4:1 ratio as illustrated in Figure 1, stratified by occurrence of obstructive events, so that both the training and test set had a comparable prevalence of oCAD. Each patient was characterized by an array of features, including (semi-)quantitative PET MPI including summed difference score (SDS),

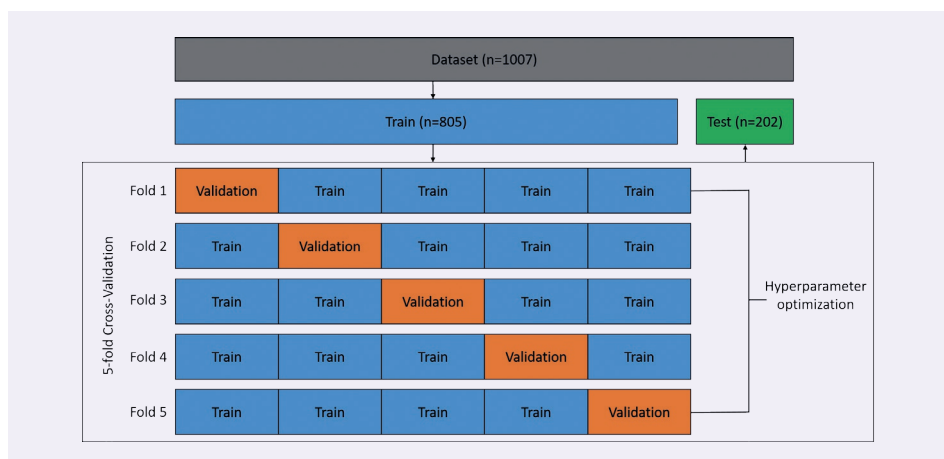


**Figure 1.** Visualization of the cross-validation procedure of the development of the XGBoost model. The entire dataset is initially split 4:1 into a training and test dataset. The training set is used to optimize hyperparameters via cross-validation. The test dataset is used to evaluate the performance in an independent patient population.

summed stress score (SSS), MBF and MFR measurements and CACS, and various other clinical features which are shown in Table 1. All features except MBF, MFR, CACS, age, resting heart rate and body mass index (BMI), were transformed to dichotomous variables. The remaining continuous variables of the training dataset were normalized such that the mean value was 0 and standard deviation was 1. Next, the mean and standard deviation of the training dataset were used to normalize the test dataset.

### Model development and feature importance

The XGBoost model was optimized with the training dataset, using hyperparameter optimization via grid search in combination with 5-fold stratified cross-validation as shown in Figure 1. Additionally, the feature importance was extracted from the model. The feature ranking is based on the number of times a feature appeared (F-score) in decision trees within the model. The model with the highest F1-score was evaluated on the test dataset.

### Model and readers' performance

Two expert readers (cardiologist and nuclear medicine physician) assessed the clinical data, CACS and the Rb-82 PET data for each patient. If the expert readers reached consensus of possible or definite defect, based on all these data, patients were categorized as having oCAD. To assess the value of the XGBoost model in the detection of oCAD, the predictive performance of the model was compared to that of the expert readers. The reference for both the expert readers and the XGBoost model was oCAD on ICA.

### Statistical analysis

Statistical analysis was performed using IBM SPSS (IBM SPSS Statistics for Windows, Version 26.0. Armonk, NY: IBM Corp). Differences in patient characteristics between the training and test dataset were evaluated using Student's t-test, or Mann-Whitney U test, when appropriate. Following a Bonferroni correction for the comparisons of the basic characteristics between the training and test dataset, the level of statistical significance was set to  $0.05/48 = 0.001$  for all statistical analyses.

Furthermore, we computed the accuracy, sensitivity and specificity, achieved by the expert readers, for detecting oCAD and the composite of oCAD and all-cause mortality. Next, the area under the receiver operating curve (AUC) was computed for the XGBoost model for both the training and test dataset. From the receiver operating curve (ROC) of the training dataset we determined two different model thresholds to discriminate between non-oCAD and oCAD. The first being the model threshold that resulted in a similar sensitivity as compared to the sensitivity obtained by the expert readers ( $\text{threshold}_{\text{sens}}$ ). The second being the model threshold that resulted in a similar specificity as compared to the specificity obtained by the expert readers ( $\text{threshold}_{\text{spec}}$ ). Next, the performance metrics (accuracy, sensitivity and specificity) were calculated on both the training and test dataset. The performance metrics of the XGBoost model was compared to those of the readers using McNemar's test. Following a Bonferroni correction for the comparisons of the expert readers to the two model thresholds applied to both datasets, the level of statistical significance was set to  $0.05/4=0.0125$ .

## RESULTS

Data that were used as input features for the ML model and follow-up data for the training and test set are summarized in Table 1. Of the included 1007 patients, 111 (11%) patients were classified as having oCAD during follow-up. An additional 26 (3%) patients died during follow-up. The median follow-up time was 1.8 years. The minimum follow-up time was 1 year whilst the longest follow-up time was 2.7 years. Most cases of oCAD occurred within 90 days after the PET scan (early revascularization), 67% in the training dataset and 73% in the test dataset, respectively. No significant differences were found in patient characteristics between the training and test datasets ( $p > 0.02$ ).

**Table 1.** Summary of data that were used as input features for the XGBoost model and follow-up data of both the training and test dataset.

	Training set (N=805)	Test set (N=202)	p values
<b>Input features</b>			
Age (years)	66 ± 11	66 ± 11	0.54
Male (%)	50	52	0.77
Height (cm)	174 ± 10	174 ± 11	0.54
Weight (kg)	89 ± 20	89 ± 20	0.80
BMI (kg/m <sup>2</sup> )	25.6 ± 5.2	25.6 ± 5.1	0.93
Pulse (beats/min)	70 ± 14	70 ± 11	0.56
Creatinine serum (µmol/L)	97 ± 76	90 ± 41	0.19
Smoking never (%)	40	39	0.70
Smoking ever (%)	47	47	0.84
Smoking present (%)	13	15	0.38
Diabetes mellitus (%)	20	18	0.49
Hypercholesterolemia (%)	41	41	0.89
Hypertension (%)	62	61	0.80
Family history (%)	51	47	0.25
Medical history (%)	20	27	0.02
COPD (%)	12	16	0.09
CVA (%)	9	13	0.12
Medication usage (%)	94	97	0.12
Aspirin (%)	28	27	0.78
Clopidogrel (%)	4	5	0.82
Acenocoumerol (%)	9	11	0.40
Beta blockage (%)	54	62	0.03
Ace/All inhibitor (%)	41	45	0.34
Ca-channel blocker (%)	24	18	0.08
Statin (%)	43	47	0.33
Diuretic (%)	29	36	0.06

	Training set (N=805)	Test set (N=202)	p values
Total CAC-score	449 ± 771	505 ± 845	0.36
LM CAC-score	21 ± 55	24 ± 67	0.49
LAD CAC-score	187 ± 298	194 ± 258	0.77
LCX CAC-score	88 ± 210	77 ± 186	0.48
RCA CAC-score	153 ± 360	200 ± 442	0.16
PET SSS	6 ± 7	6 ± 6	0.87
PET SDS	2 ± 4	3 ± 4	0.24
EF stress	64 ± 12	63 ± 13	0.06
EF rest	59 ± 12	58 ± 12	0.23
Global stress MBF (mL/min/g)	2.5 ± 0.7	2.5 ± 0.8	0.30
Global rest MBF (mL/min/g)	1.1 ± 0.3	1.1 ± 0.3	0.75
Global MFR	2.5 ± 0.6	2.4 ± 0.6	0.36
LAD stress MBF (mL/min/g)	2.5 ± 0.7	2.5 ± 0.7	0.27
LAD rest MBF (mL/min/g)	1.1 ± 0.3	1.1 ± 0.3	0.61
LAD MFR	2.4 ± 0.6	2.4 ± 0.6	0.45
LCX stress MBF (mL/min/g)	2.5 ± 0.7	2.4 ± 0.8	0.32
LCX rest MBF (mL/min/g)	1.1 ± 0.3	1.1 ± 0.3	0.80
LCX MFR	2.4 ± 0.7	2.4 ± 0.7	0.38
RCA stress MBF (mL/min/g)	2.7 ± 0.8	2.6 ± 0.9	0.46
RCA rest MBF (mL/min/g)	1.1 ± 0.4	1.1 ± 0.4	0.99
RCA MFR	2.6 ± 0.7	2.5 ± 0.8	0.36
MPE	1.3 ± 0.7	1.2 ± 0.7	0.16
Follow-up data			
Obstructive CAD (%)	11	11	0.95
All Cause Mortality (%)	2.6	2.5	0.92
Time to obstructive CAD (months)	1 [0-5.5]	1 [0-3]	0.23
Event <90 days after scan (%)	8	8	0.82

Data are presented as mean ± SD, median [interquartile range] or percentage;  
The p values are given for either the  $\chi^2$  test, t-test or Mann-Whitney U test

**Machine learning**

Features were ranked in order of importance for the XGBoost model for oCAD and the composite of oCAD & all-cause mortality. The top 10 predictors for the XGBoost model consisted of CACS and PET-derived features, as shown in Figure 2. The summed difference score (SDS) was the most important feature with an F-score of 44. Features with a feature importance of less than one and therefore with little to non-predictive value for oCAD were length, family history, medical history, COPD, past CVA, hypertension and present smoking. In addition, all prescribed medication categories were found to hold little to non-predictive value (F-score  $\leq 1$ ). Feature importance for the XGBoost model for oCAD & all-cause death is shown in Figure 2B. We observed similar results for the most and least important predictors as when only considering oCAD as an endpoint.

Using oCAD on ICA as reference ROC curve analysis showed an AUC of 0.92 for the training dataset and 0.89 for the test dataset, respectively, as shown in Figure 3. The expert readers achieved an accuracy of 88% (sensitivity 69% and specificity 90%) for the detection of oCAD as shown in Table 2 and Figure 5. No significant ( $p \geq 0.03$ ) differences in accuracies (89% and 82%), sensitivities (68% and 73%) and specificities (92% and 83%) were found for the XGBoost model on the test data as compared to the expert readers, using either  $\text{threshold}_{\text{sens}}$  or  $\text{threshold}_{\text{spec}}$ , respectively.

For the composite of oCAD and all-cause mortality ROC curve analysis showed an AUC of 0.90 for the training dataset and 0.89 for the test dataset respectively, as shown in Figure 4. The readers achieved an accuracy, sensitivity and specificity of 86%, 61% and 90%, respectively, as shown in Table 3 and Figure 5. No significant differences ( $p > 0.07$ ) in accuracies (89% and 84%), sensitivities (67% and 78%) and specificities (92% and 85%) were obtained for the XGBoost model on the test data as compared to the expert readers, when using either  $\text{threshold}_{\text{sens}}$  or  $\text{threshold}_{\text{spec}}$ , respectively.



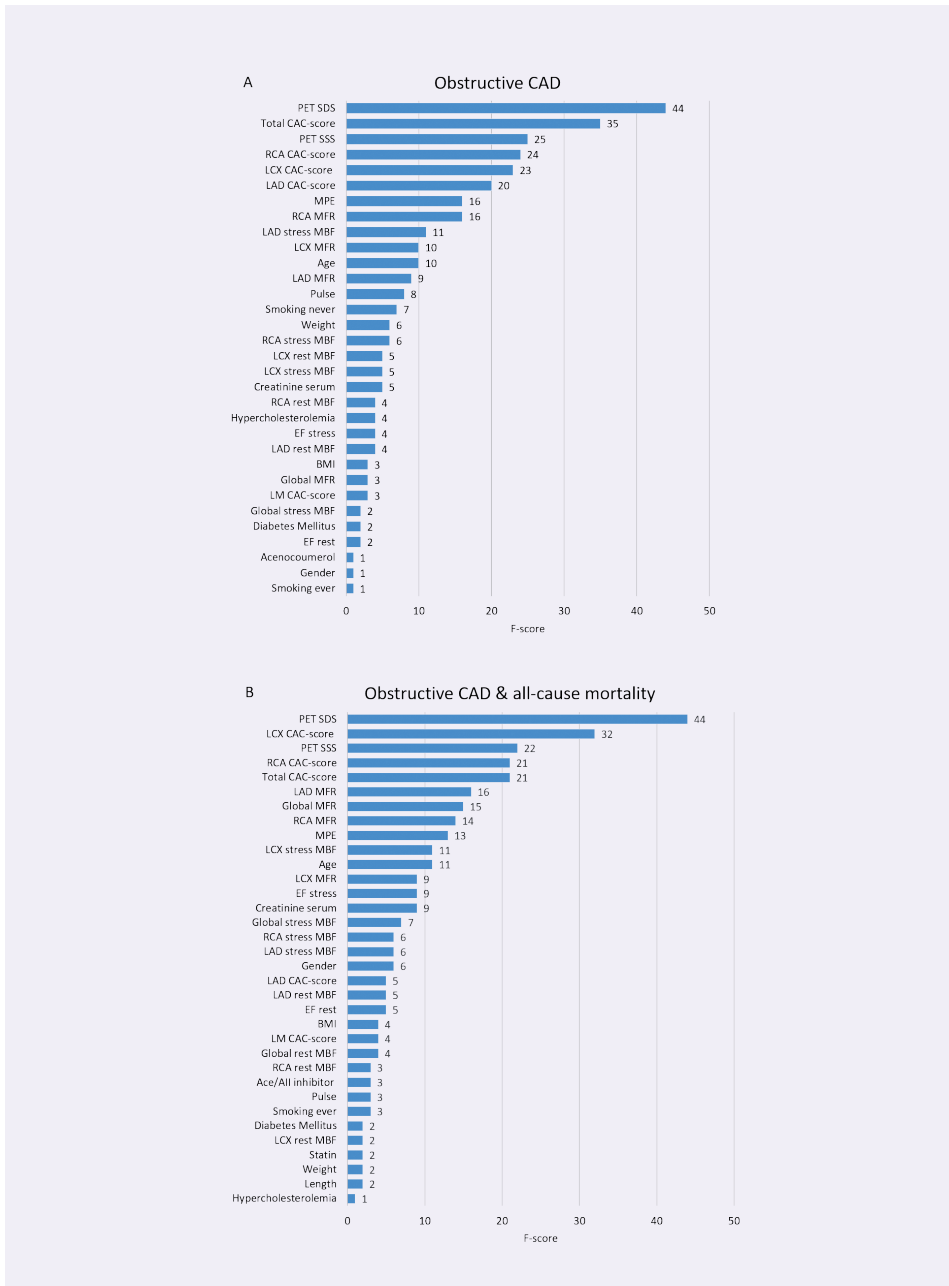


**Figure 2.** Feature importance ranking of features with F-scores >0 of the XGBoost model to detect obstructive CAD (A) and the composite of obstructive CAD & all-cause mortality (B). The F-score was calculated by the improvement in accuracy brought by a feature to the branches it is on. Features with low importance can be interpreted as weak predictors for obstructive CAD. BMI body mass index; CAC-score coronary artery calcium score; EF ejection fraction; LAD left anterior descending artery; LCX left circumflex; LM left main artery; MBF myocardial blood flow; MFR myocardial flow reserve; MPE myocardial perfusion entropy; RCA right coronary artery; SDS summed difference score; SSS summed stress score.

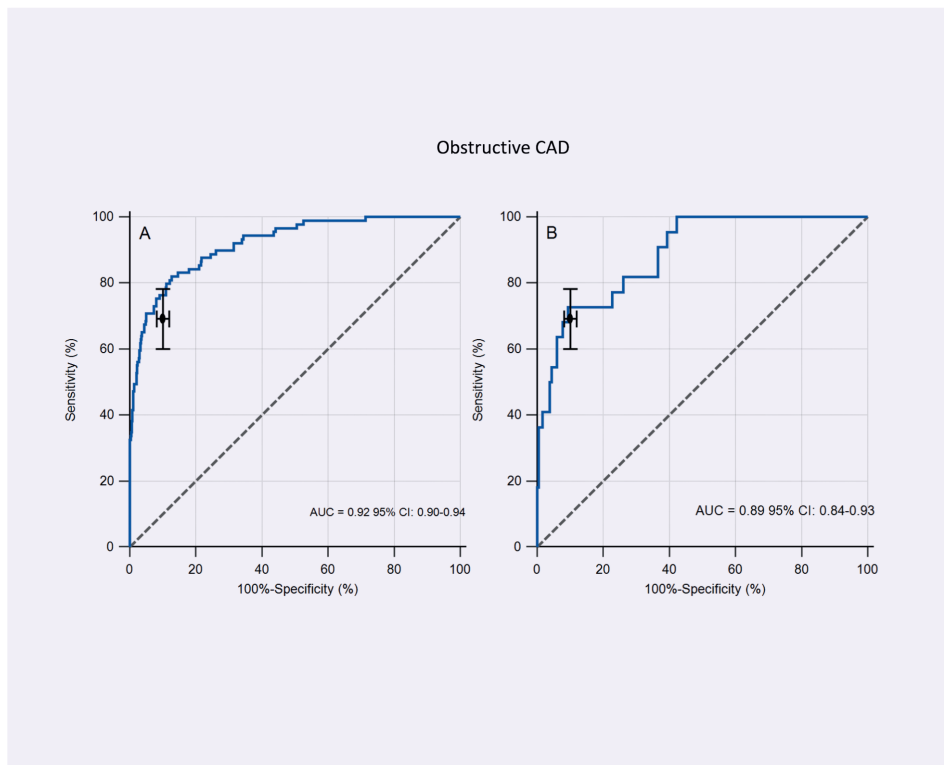
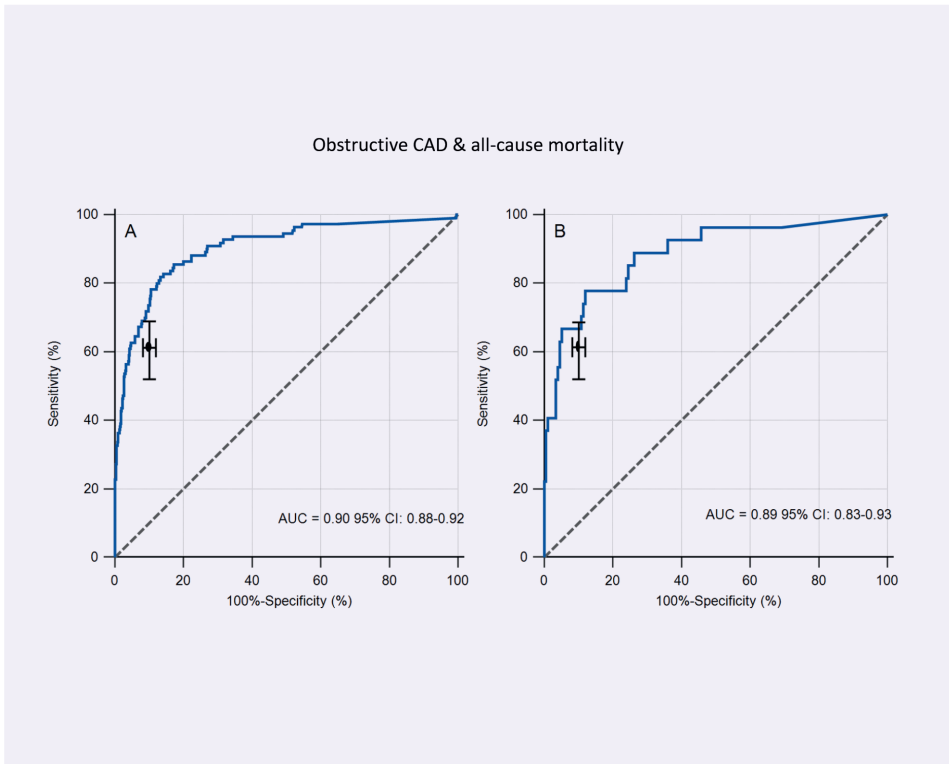


Figure 3. ROC curve of the XGBoost model for detection of obstructive CAD on the A) training (n=805) and B) test (n=202) dataset. The sensitivity and specificity of the expert readers, is plotted (black dot) with corresponding 95% confidence intervals.

Table 2. Diagnostic performance of expert readers and the ML model for the detection of obstructive CAD. By definition the 69% sensitivity and the 90% specificity of the training data are equal to those of the expert readers.

	Expert readers (reference)	Training data		Test data	
		Threshold <sub>sens</sub>	Threshold <sub>spec</sub>	Threshold <sub>sens</sub>	Threshold <sub>spec</sub>
Accuracy	88%	92%*	88%	89%	82%
Sensitivity	69%	69%	76%	68%	73%
Specificity	90%	95%*	90%	92%	83%

\*p<0.013



**Figure 4.** ROC curve of the XGBoost model for detection of obstructive CAD and all-cause mortality on the A) training (n=805) and B) test (n=202) dataset. The sensitivity and specificity of the expert readers, is plotted (black dot) with corresponding 95% confidence intervals.

**Table 3.** Diagnostic performance of expert readers and the ML model for the detection of obstructive CAD and all-cause mortality. By definition the 61% sensitivity and the 90% specificity of the training data are equal to those of the expert readers.

	Expert readers (reference)	Training data		Test data	
		Threshold <sub>sens</sub>	Threshold <sub>spec</sub>	Threshold <sub>sens</sub>	Threshold <sub>spec</sub>
Accuracy	86%	91%*	88%	89%	84%
Sensitivity	61%	61%	74%*	67%	78%
Specificity	90%	96%*	90%	92%	85%

\*p<0.013

## DISCUSSION

In this study we have developed and tested an XGBoost model to diagnose patients with oCAD, using clinical data, CACS and Rb-82 PET imaging data. The ML model resulted in high AUCs (0.89) on the test data and showed a comparable performance to that of the expert readers. In clinical practice, such a model can serve as a post-test likelihood test for oCAD and be used to improve risk stratification and thereby decisions in low to intermediate risk patients regarding further testing or therapies.

We were also able to identify the most important predictors of oCAD via feature importance ranking of the XGBoost model. PET derived (semi-)quantitative values including SDS, SSS, MBF and MFR, as well as CACS were much stronger predictors as compared to classical risk factors such as smoking and hypertension. The importance of PET and CACS features is not unexpected, since these are well established as independent and complementary predictors<sup>17, 18</sup>. Furthermore, the creatinine serum level was ranked as a relatively strong predictor. This may be explained by the experience that renal dysfunction increases the likelihood of CAD and has a negative impact on the prognosis<sup>19</sup>.

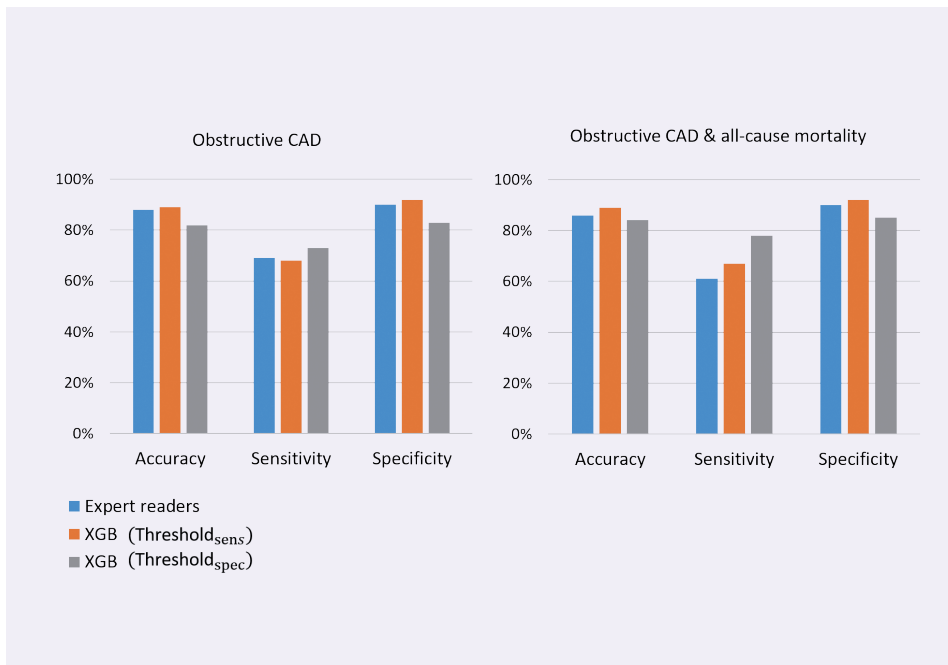


**Figure 5.** Column chart showing the performance of detecting obstructive CAD (A) and a composite of obstructive CAD and all-cause mortality (B) on the test dataset (n=202) by expert physicians (blue bars) and the XGBoost model using threshold<sub>sens</sub> (orange) and threshold<sub>spec</sub> (grey). No significant differences were observed in detecting obstructive CAD with and without all-cause mortality between the experts and the XGBoost model using either threshold<sub>sens</sub> or threshold<sub>spec</sub>. No significant differences were found in detecting obstructive CAD including all-cause mortality.

There are several studies on the performance of models on the basis of clinical data, CACS and/or nuclear imaging data (SPECT or PET), but none of them combined all these features into one model. In 2013, Arsanjani et al.<sup>8</sup> already showed that ML significantly improved diagnostic performance of MPI with SPECT by computational integration of quantitative perfusion and clinical data to the level rivaling expert analysis. The added predictive value of combining clinical information and SPECT MPI data using ML was also studied by Bentancur et al.<sup>20</sup>. They showed that the combination resulted in a high predictive accuracy for 3-year risk of MACE with an AUC of 0.81. Fathala et al.<sup>3</sup> showed that the addition of CACS to MPI with PET may help in the detection of subclinical CAD, especially in patients with unknown history of CAD. Al'Aref et al. compared the performance of a ML model alone, ML model with CACS, CAD consortium clinical score, CAD consortium score with CACS and updated Diamon-Forrester score to predict the presence of oCAD on CCTA<sup>21</sup>. They concluded that ML using clinical data in addition to CACS can accurately estimate the pretest likelihood of oCAD. ML with CACS produced the best performance with an AUC of 0.87. In our study all relevant data (clinical, CACS and PET) were combined and the ML model resulted in a performance with an AUC of 0.89 on the test data using oCAD on ICA as reference.

This study has several limitations. First, we used data of one hospital which makes generalizability to other centers not straight forward. Although most input parameters of the ML model are or can be standardized (clinical information and CACS), MBF measurements based on PET are generally not standardized among different centers and depend on several technical aspects such as reconstructions settings and post-processing software<sup>22-25</sup>. Still, for each center it is possible and even recommendable to retrain and test the ML model to their unique patient data. Although this will take effort, it will lead to center-specific optimized hyperparameter values and hence likely to the best diagnostic performance.

Second, we classified patients as having oCAD if follow-up included either a conclusive invasive coronary angiography (ICA) for CAD<sup>7</sup> or a revascularization during follow-up. Inherently, we might have missed patients with oCAD as not all were referred for ICA. This bias may lead to underestimation of the positive cases. Moreover, as a second endpoint we used a composite of oCAD and occurrence of all-cause mortality as a reference. Some bias in our results can be expected as probably not all deceased patients died of oCAD. However, as the number of deceased patients was relatively low we expect the influence on our results to be limited.

Third, the number of patients included was relatively low. In particular we had an imbalanced dataset as the number of patients who were classified as having oCAD was only 111 (11%) of the total population. Furthermore, only 20% of the patients were included in the test dataset, which resulted in performance metrics with relatively large confidence intervals. This only allowed us to demonstrate that the ML model performance did not significantly differ from the readers' performance. Using a larger database might possibly show a superiority of the ML model. Moreover, the retrospective study design may have led to some bias in our study population, since we only included patients who were referred to our institution for both CACS and Rb-82 PET imaging.

Finally, the ML model was only trained and tested on patients without prior history of CAD. Therefore, the ML model might not be generalizable to patients with a prior history of CAD. However, by retraining the model on data from a different patient population we expect that a high diagnostic performance can be obtained as well.

## **CLINICAL IMPLICATIONS**

The XGBoost model derived in this study is an objective classification approach for identifying patients with oCAD and led to a similar performance compared to that of expert physicians. It is therefore expected to facilitate the detection of oCAD, risk stratification and finally optimize patient-specific treatment when using it as a post-test likelihood tool. As this technological innovation provides automated interpretation of data it might also help physicians in training.

## **CONCLUSION**

We have developed and validated a machine-learning model to diagnose obstructive CAD in patients without prior history of CAD, based on clinical risk factors, medication and imaging data, including CACS and Rb-82 PET. It resulted in similar performance as compared to the performance of experts imaging physicians. Therefore, utilization of such a model is promising in the diagnosis of obstructive CAD. It may be used for risk stratification and eventually for guiding further patient treatment.

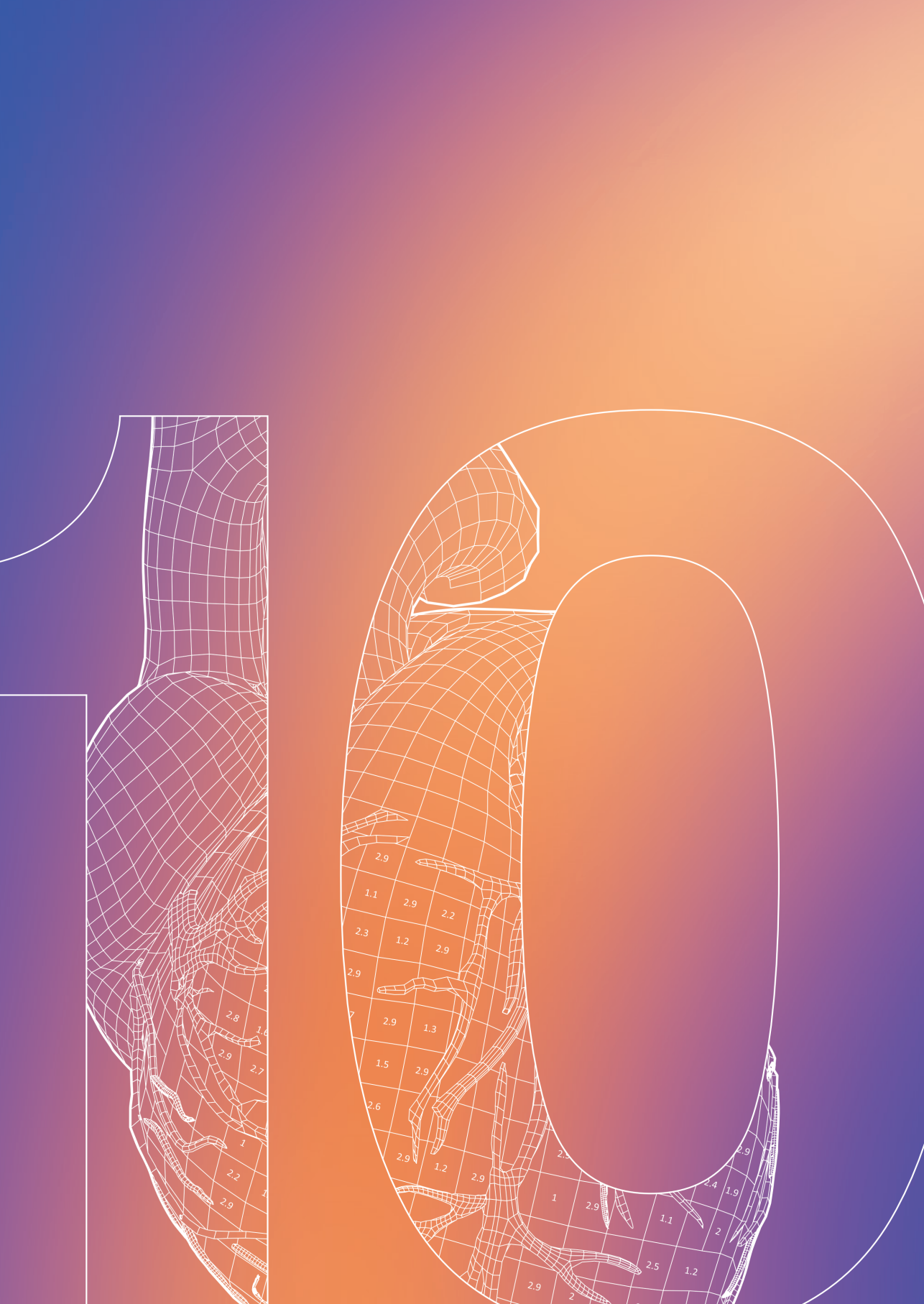
## REFERENCES

1. Montalescot G, Sechtem U, Achenbach S, Andreotti F, Arden C, Budaj A, et al. 2013 ESC guidelines on the management of stable coronary artery disease: The task force on the management of stable coronary artery disease of the European Society of Cardiology. *Eur Heart J*. 2013;34:2949-3003.
2. Carpeggiani C, Picano E, Brambilla M, Michelassi C, Knuuti J, Kauffman P, et al. Variability of radiation doses of cardiac diagnostic imaging tests: The RADIO-EVINCI study (RADIation and Ose subproject of the EVINCI study). *BMC Cardiovasc Disord*. 2017;17:1-8.
3. Fathala A, Aboulkheir M, Shoukri MM, Alsergani H. Diagnostic accuracy of 13N-ammonia myocardial perfusion imaging with PET-CT in the detection of coronary artery disease. *Cardiovasc Diagn Ther*. 2019;9:35.
4. van Diemen PA, Schumacher SP, Driessen RS, Bom MJ, Stuijzand WJ, Everaars H, et al. Coronary computed tomography angiography and [<sup>15</sup>O] H<sub>2</sub>O positron emission tomography perfusion imaging for the assessment of coronary artery disease. *Neth Hear J*. 2020;28:57-65.
5. Slart RH, Williams MC, Juarez-Orozco LE, Rischpler C, Dweck MR, Glaudemans AW, et al. Position paper of the EACVI and EANM on artificial intelligence applications in multimodality cardiovascular imaging using SPECT/CT, PET/CT, and cardiac CT. *Eur J Nucl Med Mol Imaging*. 2021;48:1399-413.
6. Chan S, Bailey J, Ros PR. Artificial intelligence in radiology: Summary of the AUR academic radiology and industry leaders roundtable. *Acad Radiol*. 2020;27:117-20.
7. Juarez-Orozco LE, Knol RJ, Sanchez-Catasus CA, Martinez-Manzanera O, Van der Zant, Friso M, Knuuti J. Machine learning in the integration of simple variables for identifying patients with myocardial ischemia. *J Nucl Cardiol*. 2020;27:147-55.
8. Arsanjani R, Xu Y, Dey D, Vahistha V, Shalev A, Nakanishi R, et al. Improved accuracy of myocardial perfusion SPECT for detection of coronary artery disease by machine learning in a large population. *J Nucl Cardiol*. 2013;20:553-62.
9. Agatston AS, Janowitz WR, Hildner FJ, Zusmer NR, Viamonte M, Detrano R. Quantification of coronary artery calcium using ultrafast computed tomography. *J Am Coll Cardiol*. 1990;15:827-32.
10. Lortie M, Beanlands R, Yoshinaga K, Klein R, DaSilva J, deKemp R. Quantification of myocardial blood flow with 82Rb dynamic PET imaging. *Eur J Nucl Med Mol Imaging*. 2007;34:1765-74.
11. Koenders SS, van Dijk JD, Jager PL, Ottervanger JP, Slump CH, van Dalen JA. Impact of regadenoson-induced myocardial creep on dynamic rubidium-82 PET myocardial blood flow quantification. *J Nucl Cardiol*. 2019;26:719-28.
12. Van Dalen J, Koenders SS, Vendel BN, Jager PL, Van Dijk JD. Entropy-based myocardial blood flow measurements using PET: A way to improve reproducibility. *Eur Heart J Cardiovasc Imaging*. 2021;22:jeab111.066 doi:10.1093/ehjci/jeab111.066.
13. C. E. Shannon. A mathematical theory of communication. *The Bell System Technical Journal*. 1948;27:379-656 doi:10.1002/j.1538-7305.1948.tb01338.x.
14. Yokota S, Mouden M, Ottervanger JP, Engbers E, Jager PL, Timmer JR, et al. Coronary calcium score influences referral for invasive coronary angiography after normal myocardial perfusion SPECT. *J Nucl Cardiol*. 2019;26:602-12.
15. Chen T, Guestrin C. Xgboost: A scalable tree boosting system. *Proc 22nd*

16. ACM SIGKDD International Conference on Knowledge Discovery and Data Mining. 2016:785-94.
17. Pedregosa F, Varoquaux G, Gramfort A, Michel V, Thirion B, Grisel O, et al. Scikit-learn: Machine learning in python. *JMLR*. 2011;12:2825-30.
18. Neves PO, Andrade J, Monção H. Coronary artery calcium score: Current status. *Radiol Bras*. 2017;50:182-9.
19. Ziadi M, deKemp R, Williams K, Guo A, Renaud J, Chow B, et al. Does quantification of myocardial flow reserve using rubidium-82 positron emission tomography facilitate detection of multivessel coronary artery disease? *J Nucl Cardiol*. 2012;19:670-80.
20. Murthy V, Bateman T, Beanlands R, Berman D, Borges-Neto S, Chareonthaitawee P, et al. Clinical quantification of myocardial blood flow using PET: Joint position paper of the SNMMI cardiovascular council and the ASNC. *J Nucl Cardiol*. 2018;25:269-97.
21. Betancur J, Otaki Y, Motwani M, Fish MB, Lemley M, Dey D, et al. Prognostic value of combined clinical and myocardial perfusion imaging data using machine learning. *JACC Cardiovasc Imaging*. 2018;11:1000-9.
22. Al'Aref SJ, Maliakal G, Singh G, van Rosendaal AR, Ma X, Xu Z, et al. Machine learning of clinical variables and coronary artery calcium scoring for the prediction of obstructive coronary artery disease on coronary computed tomography angiography: Analysis from the CONFIRM registry. *Eur Heart J*. 2020;41:359-67.
23. Koenders SS, van Dijk JD, Jager PL, Mouden M, Tegelaar AG, Slump CH, et al. Effect of temporal sampling protocols on myocardial blood flow measurements using rubidium-82 PET. *J Nucl Cardiol*. 2022;29:1729-41.
24. Murthy VL, Lee BC, Sitek A, Naya M, Moody J, Polavarapu V, et al. Comparison and prognostic validation of multiple methods of quantification of myocardial blood flow with <sup>82</sup>Rb PET. *J Nucl Med*. 2014;55:1952-8.
25. Tahari AK, Lee A, Rajaram M, Fukushima K, Lodge MA, Lee BC, et al. Absolute myocardial flow quantification with (<sup>82</sup>)rb PET/CT: Comparison of different software packages and methods. *Eur J Nucl Med Mol Imaging*. 2014;41:126-35.
26. Armstrong I, Tonge C, Arumugam P. Impact of point spread function modeling and time-of-flight on myocardial blood flow and myocardial flow reserve measurements for rubidium-82 cardiac PET. *J Nucl Cardiol*. 2014;21:467-74.







# SUMMARY AND FUTURE PERSPECTIVES

## **Authors**

Sabine S. Koenders<sup>1,2</sup>

## **Author Affiliations**

1. Department of Nuclear Medicine, Isala Hospital, Zwolle, the Netherlands
2. Technical Medical Centre, University of Twente, Enschede, the Netherlands

**Unpublished**

## INTRODUCTION AND AIM

Myocardial perfusion imaging (MPI) using positron emission tomography (PET) has a high diagnostic value in the detection of obstructive coronary artery disease (obstructive CAD) and is growing in its use<sup>1</sup>. The addition of myocardial blood flow (MBF) and myocardial flow reserve (MFR) measurements to the visual assessment of PET images is making its way into clinical routine. MBF and MFR provide valuable additional diagnostic and prognostic information about the extent and functional importance of possible stenosis to visual assessment of PET images<sup>2-7</sup>.

The quantification of MBF is conducted with kinetic modeling of the image-derived time-activity curves (TACs) allowing derivation of MBF in units of mL/min per gram of tissue. MFR is defined as the ratio of MBF during maximal coronary vasodilation to resting MBF<sup>5</sup>. In other words, the MFR gives an indication of the degree of coronary vasodilator capacity and reflects the extent of which a stenosis actually impairs the supply of blood to the myocardium when the demand increases.

In the process of data acquisition, image reconstruction, post-processing and interpretation of quantitative myocardial PET, there are several pitfalls that can result in unreliable blood flow quantification. In order for MBF and MFR quantification to achieve its full clinical potential, the technical aspects of MBF and MFR quantification must be well understood and standardized so that reliable MBF and MFR values can be routinely produced<sup>8</sup>.

The aim of this thesis was to study and optimize technical aspects to obtain reliable MBF and MFR values with Rubidium-82 (Rb-82) PET MPI. Furthermore, we studied the clinical value of MFR. This thesis is therefore divided into two parts.

## THESIS OVERVIEW

### PART I: OPTIMIZING OF MBF QUANTIFICATION

Part I of this thesis consists of five chapters in which we focused on how different steps in the process from data acquisition to image reconstruction and processing can affect quantitative PET MPI. Accordingly, we described how to deal with these aspects to obtain reliable MBF and MFR values.

The first step in performing MPI with PET is the data acquisition which requires the administration of Rb-82 activity. **Chapter 2** of this thesis contains an editorial to a study conducted by Hoff et al.<sup>9</sup>. The tracer activity to administer recommended in prescribing information by a commercial Rb-82 infusion system manufacturer is higher than what is recommended in current literature<sup>10, 11</sup>. Hoff et al. compared the effect of different administered activities (1110 MBq versus either 740 MBq or 370 MBq) on relative MPI images and on MBF and MFR values. They showed that the low tracer activity of 740 MBq is sufficient for both semi-quantitative and quantitative MPI whereas the injected tracer activity of 370 MBq only provided acceptable quantitative MPI. In our opinion their study has extended the current knowledge

on the (technical) pitfalls in MBF and MFR quantification using PET and contributes to the integration of flow quantification in clinical practice.

Once the activity is administered, it is important that the PET scanner is capable of dealing with the accompanying high count-rates in order to prevent detector saturation during the first-pass phase<sup>10, 11</sup>. Inaccurate count-rate measurements can result in unreliable MBF and MFR values<sup>12</sup>. Recent developments in PET technology include PET systems using silicon photomultipliers (SiPM) with digital readout instead of conventional photomultiplier tubes (PMTs)<sup>13-16</sup>. These SiPM-based PET systems have a relatively high count-rate capability and an improved spatial and timing resolution as compared to PMT-based PET<sup>13-15, 17, 18</sup>. In **Chapter 3** we determined the value of a SiPM-based PET scanner (Vereos, Philips Healthcare) in MPI as compared to a PMT-based PET scanner (Discovery 690, GE Healthcare). We performed a prospective study in which 30 patients referred for Rb-82 PET/computed tomography (CT) were scanned using both scanners. We compared image quality, defect interpretation, interpreter's confidence, MBF and MFR values between both systems. We showed that defect interpretation, interpreter's confidence and blood flow measurements were comparable between both systems. However, SiPM-based PET provided an improved image quality ( $p=0.03$ ) in comparison to PMT-based PET.

After data acquisition PET images are reconstructed and processed. A temporal sampling protocol is used to reconstruct the dynamic images which are used for MBF and MFR quantification. In **Chapter 4** we determined the effect of different temporal sampling protocols on MBF and MFR quantification. Rb-82 PET data of 20 patients referred for rest and regadenoson-induced stress Rb-82 PET/CT were reconstructed using 14 different temporal sampling protocols. MBF and MFR values were calculated for all protocols and compared to a reference protocol. We found different rest and stress MBF values in six out of the 14 protocols ( $p \leq 0.003$ ). However, MFR did not differ for any of the protocols ( $p \geq 0.11$ ). Therefore, MFR seems to be a more suitable parameter to be used between centers and for multicenter trials. For the use of rest and stress MBF across multiple sites in the detection of obstructive CAD and in multicenter trials, harmonization of technical aspects such as temporal sampling is necessary.

After the dynamic images are reconstructed, they need to be processed. During data processing, it is important to check for patient motion as patient motion can significantly affect MBF and MFR quantification<sup>5, 19-22</sup>. In particular, motion can be expected during stress imaging when using pharmacological stress agents. A specific kind of patient motion that we observe is a repositioning of the heart after administration of regadenoson. This so-called myocardial creep is presumably caused by an increasing depth of respiration and lung volume induced by regadenoson which causes the repositioning of the diaphragm and heart<sup>23</sup>. In **Chapter 5** we determined the effect of correcting for this myocardial creep on MBF and MFR values. We retrospectively included 119 patients referred for rest and regadenoson-induced stress Rb-82 PET/CT and visually assessed the presence of myocardial creep. Next, we compared MBF and MFR values before and after correction for myocardial creep for the three vascular territories, the left anterior descending (LAD), left circumflex (LCX) and right coronary artery (RCA) and for the myocardium as a whole. We showed that myocardial creep is a frequent phenomenon

as it was observed in 52% of our patients during the stress scan. We found that especially the MBF value in the RCA territory was affected as the mean MBF decreased from 4.0 to 2.7 mL/min/g after correction for myocardial creep ( $p < 0.001$ ). Therefore, detection and correction of myocardial creep is necessary to provide reliable flow measurements. In **Chapter 6** we provided instructions on how to detect and correct for myocardial creep. In short, first the myocardial contour has to be determined using the tissue phase ( $> 2.15$  min). Next, the myocardium contour needs to be copied to all other time frames. Misalignments between the myocardium contour and the observed activity has to be checked in all time frames and, if present, these have to be adjusted. Once all time frames are free of any misalignments, the MBF and MFR values can be calculated.

## PART II: CLINICAL VALUE OF MBF QUANTIFICATION

Part II of this thesis covers the clinical value of MFR quantification using Rb-82 PET. In clinical practice, visual assessment of Rb-82 PET MPI is usually combined with *global* MFR values to detect obstructive CAD<sup>3, 24</sup>. However, small regional blood flow deficits then may remain unnoticed. In **Chapter 7** we compared the diagnostic value of *regional* MFR to *global* MFR in the detection of obstructive CAD. For this purpose, MFR was determined globally, per vessel territory and per myocardial segment. Vessel MFR was defined as the lowest flow reserve of LAD, LCX and RCA territories and segmental MFR as the lowest flow reserve of the 17 segments. We retrospectively included 1519 patients without prior history of obstructive CAD referred for rest and regadenoson-induced stress Rb-82 PET/CT. The primary endpoint was obstructive CAD on invasive coronary angiography (ICA). We found that the group of 148 patients classified as having obstructive CAD had a lower global MFR (median 1.9 vs. 2.4), lower vessel MFR (1.6 vs. 2.2) and lower segmental MFR (1.3 vs. 1.8) as compared to the non-obstructive CAD patients ( $p < 0.001$ ). The area under the ROC curve (AUC) for segmental MFR (0.81) was larger than the AUC of both global MFR (0.74) and vessel MFR (0.78,  $p \leq 0.005$ ). Hence, regional MFR appears to separate patients with and without obstructive CAD the best. Therefore, we recommend to use regional MFR instead of global MFR as it improves the diagnostic value of Rb-82 PET in the detection of obstructive CAD.

Although important insights are gained to measure reliable MBF and MFR values, it is yet unclear how to combine visual assessment of Rb-82 PET data with quantitative myocardial flow values in situations where conclusions on the presence of obstructive CAD are contradictory. Hence, in **Chapter 8** estimated the probability of obstructive CAD for an individual patient as a function of the MFR value in patients with a visually normal scans as well as in patients with a visually abnormal scan. The same retrospective data of 1519 patients were used as in Chapter 7. Of all 1519 patient scanned, 83% (1259) had a scan which was classified as normal and the remaining patients had a scan which was classified as abnormal (defined as having a reversible and/or irreversible defect) by consensus of two expert physicians. Of the 1259 patients with normal scans, 3.7% (46) had obstructive CAD during follow-up. Of the 260 patients with visually abnormal scans, 39% (102) had obstructive CAD during follow-up. We divided patients into quintiles based on MFR values for both the subgroup of patients with normal and abnormal scans. For each quintile we calculated the mean MFR. Next, we fitted the mean MFR's of the quintiles to the probability of obstructive CAD. We found that based on visual Rb-82 PET interpretation only patients

with >10% probability of obstructive CAD can be distinguished from patients with <10% probability. However, there is a strong dependence of MFR on patient's individual probability of obstructive CAD. Our results provide a patient-tailored risk assessment based on both visual interpretation and MFR which may affect treatment strategy.

After non-invasive imaging, cardiologists combine the imaging data, clinical data and type of complaints to estimate a post-test likelihood and, if needed, determine a specific treatment strategy. However, the human ability to interpret and integrate all available data into one post-test likelihood of obstructive CAD is limited. Artificial intelligence (AI) can help to improve interpretation of all combined data and thereby diagnosis of patients with obstructive CAD. In **Chapter 9** we aimed to develop and validate a machine learning (ML)-based model to diagnose obstructive CAD. The model was based on clinical risk factors, medication and imaging data, including CT-based calcium scoring (CACS) and Rb-82 PET. To assess the value of the ML model in the detection of obstructive CAD, the predictive performance of the model performance was compared to that of the expert readers. We retrospectively included a consecutive cohort of 1007 patients with no prior history of CAD and who underwent CT-based CACS and rest and regadenoson-induced stress Rb-82 PET/CT. Next, we developed a ML-model based on data of 805 patients and tested its performance on unseen data using the remaining 202 patients. We used obstructive CAD on ICA as reference and compared the model performance to that of expert readers. ROC curve analysis showed an AUC of 0.89 for the ML-model. The main predictors of obstructive CAD consisted of CACS and PET-derived features. The expert readers achieved an accuracy of 88%, a sensitivity of 69% and a specificity of 90%. The ML-model resulted in a similar diagnostic performance as compared to the expert readers with an accuracy of 89%, sensitivity of 68% and specificity of 92% ( $p \geq 0.03$ ). Hence, this model can be deployed as a risk stratification tool and eventually be used for guiding patient treatment.

## FUTURE PERSPECTIVES

The studies described in this thesis show that it is important to understand and correctly implement technical aspects of MBF and MFR quantification to obtain reliable blood flow values using Rb-82 PET MPI. Moreover, the clinical value of quantitative myocardial perfusion is described in this thesis. In the following paragraphs, further developments are described that can influence standardization and further improve MBF and MFR quantification in the detection of obstructive CAD in the future.

### Standardization of quantitative PET MPI

MBF and MFR values are influenced by many technical factors including differences in equipment, acquisition and reconstruction settings and processing software, which makes it difficult to define standardized MBF/MFR threshold values to discriminate between obstructive CAD and non-obstructive CAD<sup>25-27</sup>. The European Association of Nuclear Medicine (EANM) launched the EANM research Ltd (EARL) as an initiative to harmonize quantification in nuclear medicine imaging<sup>28, 29</sup>. Currently, EARL is only used for oncology PET studies. To support standardization of quantitative PET MPI, the EANM

did already publish guidelines for acquisition protocols, interpreting and reporting of quantitative PET MPI<sup>24</sup>. Future accreditation programs as EARL might also be useful to further standardize quantitative PET MPI among different medical centers and to support research and multi-center studies. Recently, the foundation was laid for the development of a multimodality validation phantom for ground truth perfusion measurement in quantitative MPI<sup>30</sup>. Although further development of this multimodality MPI phantom is necessary, these phantoms are important for future accreditation programs.

### **Other tracers for PET MPI**

In our studies we only focused on Rb-82 PET. Besides Rb-82 there are two other tracers clinically available: Nitrogen-13 ammonia (N-13) and Oxygen-15 labeled water (O-15). The disadvantages of Rb-82 as compared to the other available tracers is that the spatial resolution is affected by the relatively large positron range and that the myocardial uptake of Rb-82 is non-linear at high blood flows<sup>24</sup>. The advantage of Rb-82 over N-13 ammonia and O-15 is that it is widely available as it requires a strontium-82/Rb-82 generator instead of a cyclotron. Therefore it is likely that the use Rb-82 PET MPI will increase more rapidly in the upcoming years as compared to PET MPI using the other tracers.

Another tracer that can be used for quantitative MPI PET is Fluorine-18 (F-18) flurpiridaz and is currently under investigation<sup>31</sup>. F-18 flurpiridaz has a longer half-life (109 minutes) than the other tracers (Rb-82: 76 seconds, N-13: 9.96 minutes, O-15: 2.06 minutes) and can therefore be produced at radiopharmacy facilities which makes it also widely available<sup>5, 32, 33</sup>. F-18 flurpiridaz might come close to the ideal myocardial perfusion tracer as it has good tracer properties such as a high myocardial retention and low background in adjacent organs resulting in proper image quality and linear myocardial uptake throughout the range of flow values that can be encountered in clinical practice<sup>31, 32, 34, 35</sup>. Although comparison of MBF and MFR quantification between F-18 flurpiridaz and the other available PET perfusion tracers is still lacking, future use of F-18-flurpiridaz seems promising and might facilitate expansion of the use of PET MPI.

### **Other MPI modalities**

In patients suspected of having stable obstructive CAD and with an intermediate pre-test probability, non-invasive cardiac imaging is recommended<sup>36</sup>. Although this thesis focuses on the use of PET MPI as a functional imaging modality to detect obstructive CAD, there are other functional imaging modalities available such as cardiac magnetic resonance (CMR) imaging and single photon emission computed tomography (SPECT). Of these modalities, stress CMR and PET MPI have the best diagnostic performance to detect obstructive CAD<sup>37, 38</sup>.

Another promising modality that is making its way into quantifying myocardial perfusion is CT. Dynamic CT perfusion (CTP) requires a contrast agent instead of a radioactive tracer and samples the myocardial enhancement over time. The results of a study that compared CTP to Rb-82 PET in high-risk patients showed a high correlation for global MBF<sup>39</sup>. Global CTP-based MBF measurements were found to be within 20% of Rb-82 PET-based MBF. However, CTP-based MFR was underestimated<sup>39</sup>. Although more



research is required to optimize CTP and assess its performance in comparison to PET MPI and CMR in the detection of obstructive CAD, the application of CTP is interesting. Especially the possibility of CTP and coronary computed tomography angiography (CCTA) in one examination seems promising<sup>40</sup>. CCTA is well known to be powerful in the evaluation of the anatomical extent and severity of a possible stenosis but is less suitable in assessing the hemodynamically severity of possible stenosis<sup>41</sup>. The use of CCTA and CTP in one examination, providing anatomical and functional imaging at the same time, would be the next step in the non-invasive work-up of patients with suspected stable obstructive CAD. Moreover, the use of CTP likely reduces the costs as compared to Rb-82 PET or stress CMR and has a higher availability which makes it appealing. This raises the question if CTP in the future will replace PET MPI and CMR in the detection of obstructive CAD.

### **Artificial intelligence in cardiac imaging**

AI in nuclear medicine is emerging and AI can be applied in each individual step in the process of cardiac imaging<sup>42</sup>. AI might be beneficial in the synthesis and administration of radiopharmaceuticals, in data acquisition, image reconstruction and analysis<sup>42</sup>. For example, it is well known that proper registration between PET and CT data is important as misalignment can result in artifacts and alter the MBF and MFR measurements<sup>43-45</sup>. ML, which is a subset of AI that focuses on identifying patterns, decision making and can improve itself by data, could improve the accuracy of registration between PET and CT data by not only correcting for patient motion but also correcting for cardiac and respiratory motion<sup>46</sup>. As shown in this thesis, the presence of myocardial creep significantly affects MBF and MFR values<sup>26</sup>. ML might enable automation of detecting and correcting the motion which can save time and decreases inter-operator variability.

Furthermore, the use of AI has other potential benefits as it can result in improved diagnosis<sup>42</sup>. In chapter 9, we showed that ML in the detection of obstructive CAD seems promising and may be deployed as a risk stratification tool. The use of AI in cardiac imaging might even go one step further than “just” risk stratification. It is not inconceivable that ML might be able to guide physicians on the best treatment strategy by determining which patients might benefit most from, for example, optimal medical therapy or revascularization.

Although AI seems promising in the field of nuclear medicine, there are also some concerns regarding generalizability of models, reproducibility of results and inadequate transparency of algorithm development<sup>42</sup>. These concerns can hopefully be avoided by requiring a higher technical standard for studies that involve the development of an AI algorithm and studies that will evaluate developed models<sup>42, 47</sup>. AI has the potential to significantly improve the field of nuclear medicine but also healthcare in general.

## REFERENCES

1. Mc Ardle BA, Dowsley TF, deKemp RA, Wells GA, Beanlands RS. Does rubidium-82 PET have superior accuracy to SPECT perfusion imaging for the diagnosis of obstructive coronary disease?: A systematic review and meta-analysis. *J Am Coll Cardiol.* 2012;60:1828-37.
2. Ziadi MC, deKemp RA, Williams KA, Guo A, Chow BJ, Renaud JM, et al. Impaired myocardial flow reserve on rubidium-82 positron emission tomography imaging predicts adverse outcomes in patients assessed for myocardial ischemia: Cardiac imaging. 2011;58:740-8.
3. Murthy VL, Naya M, Foster CR, Hainer J, Gaber M, Di Carli G, et al. Improved cardiac risk assessment with noninvasive measures of coronary flow reserve. *Circulation.* 2011;124:2215-24.
4. Zigray H, Elman S, Cheng RK, Li S, Lee J, Soine L, et al. Patient factors and outcomes associated with discordance between quantitative and qualitative cardiac PET ischemia information. 2021;16:Epub ahead of print doi:10.1371/journal.pone.0246149.
5. Murthy V, Bateman T, Beanlands R, Berman D, Borges-Neto S, Chareonthaitawee P, et al. Clinical quantification of myocardial blood flow using PET: Joint position paper of the SNMMI cardiovascular council and the ASNC. *J Nucl Cardiol.* 2018;25:269-97.
6. Sciaga R, Passeri A, Bucerius J, Verberne HJ, Slart, Riemer H. J. A., Lindner O, et al. Clinical use of quantitative cardiac perfusion PET: Rationale, modalities and possible indications. position paper of the cardiovascular committee of the european association of nuclear medicine (EANM). *Eur J Nucl Med Mol Imaging.* 2016;43:1530-45.
7. Ziadi MC. Myocardial flow reserve (MFR) with positron emission tomography (PET)/computed tomography (CT): Clinical impact in diagnosis and prognosis. *Cardiovasc Diagn Ther.* 2017;7:206-18.
8. Moody J, Lee B, Corbett J, Ficaro E, Murthy V. Precision and accuracy of clinical quantification of myocardial blood flow by dynamic PET: A technical perspective. *J Nucl Cardiol.* 2015;22:935-51.
9. Hoff CM, Sørensen J, Christensen NL, Bouchelouche K, Tolbod L. Activity regimes for 82Rb cardiac PET: Effects on absolute MBF and MPI. 2020:Epub ahead of print doi:10.1007/s12350-020-02266-2.
10. van Dijk J, Jager P, van Osch J, Khodaverdi M, van Dalen J. Comparison of maximal rubidium-82 activities for myocardial blood flow quantification between digital and conventional PET systems. *J Nucl Cardiol.* 2019;26:1286-91.
11. Renaud JM, Yip K, Guimond J, Trottier M, Pibarot P, Turcotte E, et al. Characterization of 3-dimensional PET systems for accurate quantification of myocardial blood flow. *J Nucl Med.* 2017;58:103-9.
12. deKemp RA, Yoshinaga K, Beanlands RSB. Will 3-dimensional PET-CT enable the routine quantification of myocardial blood flow? *J Nucl Cardiol.* 2007;14:380-97.
13. Slomka PJ, Pan T, Germano G. Recent advances and future progress in PET instrumentation. *Semin Nucl Med.* 2016;46:5-19.
14. Miller M, Zhang J, Binzel K, Griesmer J, Laurence T, Narayanan M, et al. Characterization of the vereos digital photon counting PET system. *J Nucl Med.* 2015;56(supplement 3):434.
15. van Sluis JJ, de Jong J, Schaar J, Noordzij W, van Snick P, Dierckx R, et al. Performance characteristics of the digital biograph vision PET/CT system. *J Nucl Med.* 2019;60:1031-6.

16. Hsu DFC, Ilan E, Peterson WT, Uribe J, Lubberink M, Levin CS. Studies of a next-generation silicon-Photomultiplier–Based time-of-flight PET/CT system. *J Nucl Med*. 2017;58:1511-8.
17. Slomka PJ, Pan T, Berman DS, Germano G. Advances in SPECT and PET hardware. *Prog Cardiovasc Dis*. 2015;57:566-78.
18. Van der Vos, CS, Koopman D, Rijnsdorp S, Arends AJ, Boellaard R, van Dalen JA, et al. Quantification, improvement, and harmonization of small lesion detection with state-of-the-art PET. *Eur J Nucl Med Mol Imaging*. 2017;44:4-16.
19. Memmott M, Tonge C, Saint K, Arumugam P. Impact of pharmacological stress agent on patient motion during rubidium-82 myocardial perfusion PET/CT. *J Nucl Cardiol*. 2018;25:1286-95.
20. Hunter, Chad R. R. N., Klein R, Beanlands RS, DeKemp RA. Patient motion effects on the quantification of regional myocardial blood flow with dynamic PET imaging. 2016;43:1829-40.
21. Koshino K, Watabe H, Enmi J, Hirano Y, Zeniya T, Hasegawa S, et al. Effects of patient movement on measurements of myocardial blood flow and viability in resting 15O-water PET studies. *J Nucl Cardiol*. 2012;19:524-33.
22. Piccinelli M, Votaw JR, Garcia EV. Motion correction and its impact on absolute myocardial blood flow measures with PET. *Curr Cardiol Rep*. 2018;20:1-8.
23. Friedman J, Train KV, Maddahi J, Rozanski A, Prigent F, Bietendorf J, et al. “Upward creep” of the heart: A frequent source of false-positive reversible defects during thallium-201 stress-redistribution SPECT. 1989;30:1718.
24. Sciagrà R, Lubberink M, Hyafil F, Saraste A, Slart, Riemer H. J. A, Agostini D, et al. EANM procedural guidelines for PET/CT quantitative myocardial perfusion imaging. *Eur J Nucl Med Mol Imaging*. 2021;48:1040-69.
25. Koenders SS, van Dijk JD, Jager PL, Mouden M, Tegelaar AG, Slump CH, et al. Effect of temporal sampling protocols on myocardial blood flow measurements using rubidium-82 PET. *J Nucl Cardiol*. 2022;29:1729-41.
26. Koenders SS, van Dijk JD, Jager PL, Ottervanger JP, Slump CH, van Dalen JA. Impact of regadenoson-induced myocardial creep on dynamic rubidium-82 PET myocardial blood flow quantification. *J Nucl Cardiol*. 2019;26:719-28.
27. Koenders SS, van Dalen JA, Jager PL, Knollema S, Timmer JR, Mouden M, et al. Value of SIPM PET in myocardial perfusion imaging using rubidium-82. *J Nucl Cardiol*. 2020.
28. Boellaard R, O’Doherty MJ, Weber WA, Mottaghy FM, Lonsdale MN, Stroobants SG, et al. FDG PET and PET/CT: EANM procedure guidelines for tumour PET imaging: Version 1.0. *Eur J Nucl Med Mol Imaging*. 2010;37:181-200.
29. Boellaard R, Delgado-Bolton R, Oyen WJ, Giammarile F, Tatsch K, Eschner W, et al. FDG PET/CT: EANM procedure guidelines for tumour imaging: Version 2.0. *Eur J Nucl Med Mol Imaging*. 2015;42:328-54.
30. Kamphuis ME. 2022 Quantitative myocardial perfusion imaging: A novel multimodality validation phantom. (Doctoral dissertation) University of Twente <https://doi.org/10.3990/1.9789036553780>.
31. Maddahi J, Lazewatsky J, Udelson JE, Berman DS, Beanlands RS, Heller GV, et al. Phase-III clinical trial of fluorine-18 flurpiridaz positron emission tomography for evaluation of coronary artery disease. *J Am Coll Cardiol*. 2020;76:391-401.

32. Patel KK, Singh A, Bateman TM. The potential of F-18 flurpiridaz PET/CT myocardial perfusion imaging for precision imaging. *Curr Cardiol Rep.* 2022;1-8.
33. Maddahi J, Packard RRS. Cardiac PET perfusion tracers: Current status and future directions. *Semin Nucl Med.* 2014;44:333-43.
34. Maddahi J, Czernin J, Lazewatsky J, Huang S-, Dahlbom M, Schelbert H, et al. Phase I, first-in-human study of BMS747158, a novel 18F-labeled tracer for myocardial perfusion PET: Dosimetry, biodistribution, safety, and imaging characteristics after a single injection at rest. 2011;52:1490-8.
35. Berman DS, Maddahi J, Tamarappoo BK, Czernin J, Taillefer R, Udelson JE, et al. Phase II safety and clinical comparison with single-photon emission computed tomography myocardial perfusion imaging for detection of coronary artery disease. 2013;61:469.
36. Montalescot G, Sechtem U, Achenbach S, Andreotti F, Arden C, Budaj A, et al. 2013 ESC guidelines on the management of stable coronary artery disease: The task force on the management of stable coronary artery disease of the european society of cardiology. *Eur Heart J.* 2013;34:2949-3003.
37. Knuuti J, Ballo H, Juarez-Orozco LE, Saraste A, Kolh P, Rutjes AWS, et al. The performance of non-invasive tests to rule-in and rule-out significant coronary artery stenosis in patients with stable angina: A meta-analysis focused on post-test disease probability. *Eur Heart J.* 2018;39:3322-30.
38. Jaarsma C, Leiner T, Bekkers SC, Crijs HJ, Wildberger JE, Nagel E, et al. Diagnostic performance of noninvasive myocardial perfusion imaging using single-photon emission computed tomography, cardiac magnetic resonance, and positron emission tomography imaging for the detection of obstructive coronary artery disease A meta-analysis. *JACC.* 2012;59:1719-28.
39. Alessio AM, Bindschadler M, Busey JM, Shuman WP, Caldwell JH, Branch KR. Accuracy of myocardial blood flow estimation from dynamic contrast-enhanced cardiac CT compared with PET. *Circ Cardiovasc Imaging.* 2019;12:e008323.
40. Nakamura S, Kitagawa K, Goto Y, Omori T, Kurita T, Yamada A, et al. Incremental prognostic value of myocardial blood flow quantified with stress dynamic computed tomography perfusion imaging. *J Am Coll Cardiol.* 2019;12:1379-87.
41. Schuijf JD, Wijns W, Jukema JW, Atsma DE, de Roos A, Lamb HJ, et al. Relationship between noninvasive coronary angiography with multi-slice computed tomography and myocardial perfusion imaging. *J Am Coll Cardiol.* 2006;48:2508-14.
42. Bradshaw TJ, Boellaard R, Dutta J, Jha AK, Jacobs P, Li Q, et al. Nuclear medicine and artificial intelligence: Best practices for algorithm development. *J Nucl Med.* 2022;63:500-10.
43. Rajaram M, Tahari AK, Lee AH, Lodge MA, Tsui B, Nekolla S, et al. Cardiac PET/CT misregistration causes significant changes in estimated myocardial blood flow. *J Nucl Med.* 2013;54:50-4.
44. Martinez-Moller A, Souvatzoglou M, Navab N, Schwaiger M, Nekolla SG. Artifacts from misaligned CT in cardiac perfusion PET/CT studies: Frequency, effects, and potential solutions. *J Nucl Med.* 2007;48:188.
45. Loghin C, Sdringola S, Gould KL. Common artifacts in PET myocardial perfusion images due to attenuation-emission misregistration: Clinical significance, causes, and solutions. *J Nucl Med.* 2004;45:1029.

46. Slart RH, Williams MC, Juarez-Orozco LE, Rischpler C, Dweck MR, Glaudemans AW, et al. Position paper of the EACVI and EANM on artificial intelligence applications in multimodality cardiovascular imaging using SPECT/CT, PET/CT, and cardiac CT. *Eur J Nucl Med Mol Imaging*. 2021;48:1399-413.
47. Jha AK, Bradshaw TJ, Buvat I, Hatt M, Prabhat KC, Liu C, et al. Nuclear medicine and artificial intelligence: Best practices for evaluation (the RELAINCE guidelines). *J Nucl Med*. 2022.



# NEDERLANDSE SAMENVATTING EN TOEKOMSTPERSPECTIEVEN

## **Authors**

Sabine S. Koenders<sup>1,2</sup>

## **Author Affiliations**

1. Department of Nuclear Medicine, Isala Hospital, Zwolle, the Netherlands
2. Technical Medical Centre, University of Twente, Enschede, the Netherlands

**Unpublished**

## INTRODUCTIE EN DOEL

Myocardperfusie onderzoek (MPI) met behulp van een positron emissie tomografie (PET) scanner levert een grote diagnostische waarde in de detectie van obstructieve coronaire hartziekte (CAD) en wordt in toenemende mate gebruikt<sup>1</sup>. Naast de visuele beoordeling van de PET beelden wordt kwantificatie van de myocardiale bloedstroom (MBF) en de myocardiale bloedstroom reserve (MFR) steeds vaker toegepast in de klinische praktijk. MBF- en MFR-waarden leveren waardevolle aanvullende diagnostische en prognostische informatie over de uitgebreidheid en de functionele gevolgen van mogelijk aanwezige vernauwingen in de kransslagaders ten opzichte van de visuele beoordeling van PET-beelden<sup>2-7</sup>.

MBF kwantificatie wordt uitgevoerd met behulp van een kinetisch model. De tijd-activiteit curves (TACs) die worden afgeleid uit de dynamische PET beelden dienen als input voor een kinetisch model en hiermee is het mogelijk om de MBF te kwantificeren in eenheden van mL/min per gram weefsel. De MFR is gedefinieerd als de ratio tussen MBF tijdens maximale coronaire vasodilatatie en MBF in rust. Met andere woorden, MFR geeft informatie over de mate waarin de kransslagaders in staat zijn om de bloedstroom te laten toenemen als het hart harder moet werken<sup>5</sup>.

In het gehele proces van data-acquisitie, reconstructie, post-processing en interpretatie van de myocardperfusie kwantificatie bestaan verschillende valkuilen die kunnen leiden tot onbetrouwbare MBF- en MFR-waarden. Om ervoor te zorgen dat MBF en MFR kwantificatie betrouwbaar kan worden ingezet in de klinische praktijk, moeten de technische aspecten van MBF en MFR kwantificatie goed begrepen en gestandaardiseerd worden<sup>8</sup>.

Het doel van dit proefschrift was het onderzoeken en optimaliseren van de technische aspecten van MBF en MFR kwantificatie om betrouwbare waarden te verkrijgen met Rubidium-82 (Rb-82) PET. Verder hebben we de klinische waarde van MFR onderzocht. Dit proefschrift is derhalve opgedeeld in twee delen.

## PROEFSCHRIFT OVERZICHT

### DEEL I: OPTIMALISATIE VAN MYOCARDIALE BLOEDSTROOM KWANTIFICATIE

Deel I van dit proefschrift bestaat uit vijf hoofdstukken waarin we hebben beschreven hoe verschillende stappen in het proces van data-acquisitie tot en met beeldreconstructie en verwerking van de PET data de MBF en MFR kwantificatie kunnen beïnvloeden. Daarnaast hebben we beschreven hoe met deze technische aspecten moet worden omgegaan om betrouwbare MBF- en MFR-waarden te verkrijgen.

De eerste stap bij de uitvoering van een MPI met Rb-82 PET is de data-acquisitie. **Hoofdstuk 2** van dit proefschrift bevat een redactioneel commentaar over een studie uitgevoerd door Hoff et al.<sup>9</sup>. De aanbevolen Rb-82 activiteit die toegediend moet worden met PET volgens een fabrikant van Rb-82-toediensystemen is hoger dan die in de literatuur wordt gesuggereerd<sup>10, 11</sup>. Hoff et al. hebben daarom



het effect van verschillende activiteiten (1110 MBq versus 740 MBq of 370 MBq) op de PET-beelden en op de verkregen MBF en MFR waarden bepaald. Zij toonden aan dat 740 MBq Rb-82 voldoende is voor zowel acceptabele beelden als MBF- en MFR-waarden, terwijl 370 MBq enkel resulteerde in acceptabele MBF- en MFR- waarden. Naar onze mening heeft de studie van Hoff et al. onze huidige kennis over de (technische) valkuilen in MBF en MFR kwantificatie met PET verder uitgebreid en bijgedragen aan de integratie van MBF en MFR kwantificatie in de klinische praktijk.

Om detector saturatie tijdens de first-pass fase van het toegediende Rb-82 te voorkomen, is het belangrijk dat de PET-scanner een hoge telsnelheid heeft<sup>10, 11</sup>. Als dit niet het geval is kan het leiden tot onbetrouwbare MBF- en MFR-waarden<sup>12</sup>. Recentelijk zijn PET-systemen ontwikkeld die gebruik maken van silicium photomultipliers (SiPMs) met digitale uitlezing in plaats van conventionele photomultiplier buizen (PMTs)<sup>13-16</sup>. Deze op SiPM gebaseerde PET-systemen zijn in staat om een relatief hoge telsnelheid te realiseren en leveren een verbeterde spatiële en temporele resolutie in vergelijking met PMT-gebaseerde PET systemen<sup>13-15, 17, 18</sup>. In **Hoofdstuk 3** hebben we de waarde van een SiPM-gebaseerde PET scanner (Vereos, Philips Healthcare) bepaald ten opzichte van een PMT-gebaseerde PET scanner (Discovery 690, GE Healthcare) voor MBF en MFR kwantificatie met behulp van Rb-82. In een prospectieve studie werden 30 patiënten geïncludeerd, die waren verwezen voor een rust en regadenoson-geïnduceerde stress Rb-82 PET/CT scan. Alle geïncludeerde patiënten werden gescand op beide PET-systemen. We hebben de beeldkwaliteit, interpretatie van defecten, zekerheid van de interpretatie, en MBF- en MFR-waarden van beide systemen vergeleken. Uit dit onderzoek is gebleken dat de interpretatie van defecten, zekerheid van de interpretatie, en MBF- en MFR-waarden vergelijkbaar waren tussen beide systemen. SiPM-gebaseerde PET resulteerde echter in een betere beeldkwaliteit ( $p=0,03$ ) in vergelijking met PMT-gebaseerde PET.

Een temporeel sampling protocol dient te worden toegepast om dynamische PET data te reconstrueren in een serie beelden die vervolgens wordt gebruikt voor MBF en MFR kwantificatie. In **Hoofdstuk 4** hebben we het effect van verschillende temporele sampling protocollen op MBF en MFR kwantificatie bepaald. Rb-82 PET data van 20 patiënten, die waren verwezen voor een rust en regadenoson-geïnduceerde stress Rb-82 PET/CT scan, werden gereconstrueerd met 14 verschillende temporele sampling protocollen. MBF en MFR werden gekwantificeerd voor alle protocollen en vergeleken met een referentieprotocol. We vonden een verschil ( $p \leq 0,003$ ) in rust en stress MBF waarden in zes van de 14 protocollen. De MFR verschilde echter in geen van de protocollen met de referentie ( $p \geq 0,11$ ). Daarom lijkt de MFR een geschiktere parameter te zijn, specifiek bij gebruik hiervan tussen centra en voor multicenter-onderzoeken. Om rust en stress MBF tussen verschillende centra te kunnen vergelijken in de detectie van obstructieve CAD en in multicenter-onderzoeken is harmonisatie van alle technische aspecten, waaronder temporele sampling noodzakelijk.

Nadat de dynamische PET beelden zijn gereconstrueerd, dienen ze te worden gecontroleerd op beweging van de patiënt, aangezien beweging de MBF en MFR kwantificatie aanzienlijk kan beïnvloeden<sup>5, 19-22</sup>. Bij gebruik van regadenoson kan met name beweging worden verwacht tijdens de stress scan.

Een specifiek soort beweging van de patiënt die we hebben waargenomen, is een herpositionering van het hart na toediening van regadenoson. Deze zogenaamde myocardiale verplaatsing wordt vermoedelijk veroorzaakt door een toenemend longvolume ten gevolge van een diepe ademhaling<sup>23</sup>. In **Hoofdstuk 5** hebben we het effect van een correctie voor deze myocardiale verplaatsing op MBF en MFR metingen bepaald. Hiervoor werden retrospectief 119 patiënten geïncludeerd die waren verwezen voor een rust en regadenoson-geïnduceerde stress Rb-82 PET/CT scan. De aanwezigheid van myocardiale verplaatsing hebben we visueel vastgesteld op de verkregen beelden. Vervolgens hebben we de MBF- en MFR-waarden voor en na correctie van myocardiale verplaatsing vergeleken voor de drie vasculaire gebieden, de afdalende tak van de linker kransslagader (LAD), de linker circumflex (LCX) en de rechter kransslagader (RCA), en voor het myocard als geheel (globaal). Uit ons onderzoek bleek dat myocardiale verplaatsing tijdens stress een veelvoorkomend fenomeen is, aangezien we het hebben waargenomen bij 52% van onze patiënten. Vooral de stress MBF in het RCA-gebied werd beïnvloed: de gemiddelde MBF daalde van 4,0 naar 2,7 mL/min/g ( $p < 0,001$ ) na correctie voor myocardiale verplaatsing. Detectie en zo nodig correctie van myocardiale verplaatsing is dus noodzakelijk voor betrouwbare MBF en MFR metingen. In **Hoofdstuk 6** hebben we praktische instructies opgesteld voor de manier waarop myocardiale verplaatsing kan worden vastgesteld en voor kan worden gecorrigeerd. Eerst dient de contour van het myocard te worden bepaald met behulp van het laatste deel van de PET scan ( $> 2,15$  min na Rb-82 toediening). Vervolgens dient deze contour gekopieerd te worden naar alle andere tijdframes. Eventuele afwijkingen tussen de contour en de waargenomen Rb-82 activiteit in de beelden moeten in alle tijdframes worden vastgesteld en, indien aanwezig, worden aangepast. Pas dan kunnen betrouwbare MBF- en MFR-waarden worden berekend.

## DEEL II: KLINISCHE WAARDE VAN MYOCARDIALE BLOEDSTROOM KWANTIFICATIE

In Deel II van dit proefschrift hebben we de klinische waarde van MBF en MFR kwantificatie met behulp van Rb-82 PET onderzocht. In de praktijk wordt de visuele beoordeling van een MPI met Rb-82 PET meestal gecombineerd met de *globale* MFR om obstructieve CAD te detecteren<sup>3, 24</sup>. Kleine regionale perfusie defecten kunnen hierdoor echter onopgemerkt blijven. In **Hoofdstuk 7** hebben we de diagnostische waarde van *regionale* MFR vergeleken met *globale* MFR in de detectie van obstructieve CAD. De MFR werd globaal, per stroomgebied en per segment bepaald. Voor de regionale MFR werd de MFR van de drie grote stroomgebieden (vasculaire MFR) bepaald en gedefinieerd als de laagste MFR van de LAD-, LCX- en RCA-gebieden en de segmentale MFR als de laagste MFR van de 17 segmenten. Er werden retrospectief 1519 patiënten geïncludeerd die waren verwezen voor een rust en regadenoson-geïnduceerde stress Rb-82 PET/CT scan, zonder bekend obstructieve CAD in de voorgeschiedenis. De groep van 148 patiënten die werd geclassificeerd als patiënten met obstructieve CAD had een lagere globale MFR (mediaan 1,9 vs. 2,4), lagere vasculaire MFR (1,6 vs. 2,2) en lagere segmentale MFR (1,3 vs. 1,8) in vergelijking met de groep patiënten geclassificeerd als non-obstructieve CAD patiënten ( $p < 0,001$ ). Het oppervlak onder de ROC-curve (AUC) voor segmentale MFR (0,81) was groter dan voor globale MFR (0,74) en vasculaire MFR (0,78,  $p < 0,005$ ). Daarom adviseren wij om regionale MFR te gebruiken in plaats van globale MFR, omdat dit de diagnostische waarde van Rb-82 PET voor de detectie van obstructieve CAD verbetert.

Hoewel er belangrijke inzichten zijn verkregen in de technische aspecten die van belang zijn voor het verkrijgen van betrouwbare MBF- en MFR-waarden, is het nog onduidelijk hoe de visuele beoordeling van Rb-82 PET scans het beste gecombineerd kan worden met kwantitatieve waarden. Specifiek in gevallen waarin de visuele beoordeling en kwantitatieve waarden tegenstrijdig zijn over de aanwezigheid van obstructieve CAD. Daarom hebben we in **Hoofdstuk 8** het risico op obstructieve CAD voor een individuele patiënt bepaald als functie van de MFR-waarde bij patiënten met een visueel normale scan en bij patiënten met een visueel abnormale scan. Dezelfde retrospectieve gegevens van 1519 patiënten werden gebruikt als in hoofdstuk 7. Van deze patiënten had 83% (1259) een scan die als normaal werd geïnterpreteerd en de overige patiënten hadden een scan die als abnormaal (gedefinieerd als een reversibel en/of irreversibel defect) werd geïnterpreteerd na consensus van twee deskundige artsen. Van de 1259 patiënten met een normale scan werd tijdens een coronair angiografie (CAG) bij 3,7% (46) obstructieve CAD gediagnosticeerd tijdens de follow-up. Van de 260 patiënten met een visueel afwijkende scan had 39% (102) obstructieve CAD. We verdeelden patiënten in kwintielen op basis van MFR-waarden voor zowel de groep van patiënten met een normale scan als de groep van patiënten met een abnormale scan. Voor ieder kwintiel hebben we de gemiddelde MFR berekend. Vervolgens hebben we deze gebruikt voor een fit met een exponentiele functie aan de kans op obstructieve CAD. We toonden aan dat patiënten met >10% kans op obstructieve CAD kunnen worden onderscheiden van patiënten met <10% kans enkel op basis van een visuele beoordeling van de Rb-82 PET scans. Tegelijkertijd vonden we dat de kans op obstructieve CAD bij een individuele patiënt sterk afhangt van de MFR, voor zowel de groep van patiënten met een normale als abnormale scan: deze varieerden van <1% tot >70%. Onze studieresultaten geven een kwantitatieve risicobeoordeling voor een individuele patiënt gebaseerd op zowel visuele interpretatie van Rb-82 PET beelden als MFR metingen, die mogelijk van invloed kan zijn op de behandelstrategie.

Naast beeldvorming met PET zijn er andere factoren die van invloed zijn bij het diagnosticeren van obstructieve CAD. Zo combineren cardiologen de beschikbare scanuitkomsten met de klinische gegevens en het type klachten van de patiënt om het risico op obstructieve CAD in te schatten en, indien nodig, een specifieke behandeling te bepalen. Het menselijk brein is echter maar beperkt in staat om alle beschikbare gegevens te interpreteren en te integreren om dit risico goed te kunnen bepalen. Kunstmatige intelligentie (AI) kan helpen om de interpretatie van alle beschikbare informatie te combineren en hierdoor mogelijk ook de diagnose van patiënten met obstructieve CAD te verbeteren. In **Hoofdstuk 9** hebben we een machine learning (ML) model ontwikkeld en gevalideerd dat obstructieve CAD kan diagnosticeren. Hierbij zijn klinische risicofactoren, medicatie en beeldvorming, waaronder CT calciumscores (CACS) en Rb-82 PET als input gebruikt. Dit betrof een retrospectieve studie waarbij 1007 patiënten zonder cardiale voorgeschiedenis werden geïncludeerd die CT CACS en rust en regadenoson-geïnduceerde stress Rb-82 PET/CT hebben ondergaan. Het ML-model hebben we ontwikkeld op basis van gegevens van 805 patiënten en gevalideerd op basis van een dataset bestaande uit de resterende 202 patiënten. De referentie was obstructieve CAD gediagnosticeerd met CAG. De uitkomsten van het model hebben we vergeleken met de beoordeling van de artsen. Het ML-model resulteerde in een

oppervlakte onder de ROC curve van 0,89. De belangrijkste voorspellers voor het ML-model bestonden uit CACS en PET-afgeleide data. De artsen behaalden met de beoordeling een nauwkeurigheid van 88%, een sensitiviteit van 69% en een specificiteit van 90%. Het ML-model resulteerde in vergelijkbare nauwkeurigheid van 89%, sensitiviteit van 68% en specificiteit van 92% ( $p \geq 0,03$ ). Hieruit blijkt dat het ML-model kan worden ingezet als een risicostratificatie-model en uiteindelijk gebruikt kan worden voor het bepalen van een behandelplan.

## TOEKOMSTPERSPECTIEVEN

De studies beschreven in dit proefschrift laten zien dat het belangrijk is om de technische aspecten van MBF en MFR kwantificatie goed te begrijpen en correct te implementeren zodat betrouwbare MBF- en MFR-waarden kunnen worden verkregen met behulp van Rb-82 PET. Daarnaast is de klinische waarde van kwantitatieve myocardiële perfusie beschreven. In de volgende paragrafen worden toekomstige ontwikkelingen beschreven die standaardisatie van MBF en MFR kwantificatie in de detectie van obstructieve CAD kunnen beïnvloeden en de kwaliteit verder kunnen verbeteren.

### **Standaardisatie van kwantitatief MPI met PET**

Zoals in dit proefschrift is laten zien, worden MBF- en MFR-waarden beïnvloed door vele technische factoren, waaronder het type PET scanner, acquisitie- en reconstructie-instellingen en software om PET data uit te werken<sup>25-27</sup>. Hierdoor is het moeilijk om gestandaardiseerde MBF- en MFR-drempelwaarden te definiëren om onderscheid te kunnen maken tussen obstructieve CAD en niet-obstructieve CAD. De European Association of Nuclear Medicine (EANM) lanceerde de EANM research Ltd (EARL) als een initiatief om kwantificatie in nucleaire beeldvorming te harmoniseren<sup>28, 29</sup>. Momenteel wordt EARL echter alleen gebruikt voor oncologische PET-onderzoeken. Om standaardisatie van kwantitatieve cardiologische PET-onderzoeken te ondersteunen, heeft de EANM al wel richtlijnen gepubliceerd voor acquisitieprotocollen, interpretatie en rapportage van kwantitatief MPI met PET<sup>24</sup>. Toekomstige accreditatieprogramma's zoals EARL zijn mogelijk de volgende stap om kwantitatieve cardiologische PET-onderzoeken verder te standaardiseren en om onderzoek en multicenter studies te ondersteunen. Onlangs is de basis gelegd voor de ontwikkeling van een validatiefantom voor reproduceerbare referentie-perfusiemetingen in kwantitatief MPI dat geschikt is voor verschillende beeldvormende modaliteiten<sup>30</sup>. Hoewel verdere ontwikkeling van dit fantoom nodig is, biedt het mogelijkheden voor toekomstige accreditatieprogramma's.

### **Andere radiofarmaca voor MPI met PET**

In onze studies hebben we ons alleen gericht op Rb-82 PET. Naast Rb-82 zijn er nog twee andere radiofarmaca die in de klinische praktijk kunnen worden ingezet: stikstof-13 (N-13) ammonia en zuurstof-15 (O-15) gelabeld water. De nadelen van Rb-82 in vergelijking met deze twee radiofarmaca is dat de spatiale resolutie van de PET scan wordt beïnvloed door de relatief grote dracht van het positron en de niet lineaire myocardiële opname van Rb-82 bij hoge bloedstroomwaarden<sup>24</sup>. Het voordeel van Rb-82 ten opzichte van N-13 en O-15 is echter dat het op grote schaal verkrijgbaar is omdat het

geproduceerd kan worden met een Strontium-82/Rb-82 generator in plaats van met een cyclotron. Hierdoor is het waarschijnlijk dat het gebruik van Rb-82 bij cardiologische PET onderzoekende komende jaren sneller zal toenemen dan het gebruik van de andere twee radiofarmaca.

Een ander radiofarmacon voor kwantitatieve MPI met PET dat momenteel onderzocht wordt, is Fluorine-18 (F-18) flurpiridaz<sup>31</sup>. F-18 flurpiridaz heeft een langere halfwaardetijd (109 minuten) dan de eerdergenoemde radiofarmaca (Rb-82: 76 seconden, N-13: 9,96 minuten, O-15: 2,06 minuten) en kan hierdoor buiten het ziekenhuis worden geproduceerd waardoor het op grote schaal ingezet kan worden<sup>5, 32, 33</sup>. F-18 flurpiridaz zou bovendien in de buurt kunnen komen van het ideale myocard perfusie radiofarmacon omdat het een hoge myocardiale retentie heeft en weinig achtergrondactiviteit in aangrenzende organen laat zien. Dit zorgt voor een goede beeldkwaliteit en lineaire opname in het myocard over het hele bereik van bloedstroomwaarden die kunnen worden aangetroffen in de klinische praktijk<sup>31, 32, 34, 35</sup>. Hoewel een vergelijking van MBF- en MFR-kwantificatie tussen F-18 flurpiridaz en de andere beschikbare PET-perfusie radiofarmaca nog ontbreekt, lijkt F-18 flurpiridaz veelbelovend en zou het een toename van het gebruik van cardiologische PET kunnen stimuleren.

#### **Beeldvormende modaliteiten voor MPI met PET**

Bij patiënten met een vermoeden op obstructieve CAD en een intermediaire pre-test waarschijnlijkheid wordt niet-invasieve cardiale beeldvorming aanbevolen<sup>36</sup>. Hoewel dit proefschrift zich richt op het gebruik van PET voor MPI om obstructieve CAD te detecteren, zijn er andere opties beschikbaar zoals MPI met magnetische resonantie (CMR) en enkelvoudige fotonemissie computertomografie (SPECT). Van deze drie modaliteiten hebben CMR en PET de hoogste diagnostische waarde<sup>37, 38</sup>.

Een andere veelbelovende modaliteit die zijn weg vindt in het kwantificeren van de myocardiale bloedstroom is CT. In plaats van een radioactieve stof gebruikt CT-perfusie (CTP) een contrastmiddel en wordt het verloop van contrastaanclering in het myocard in de tijd gemeten. De resultaten van een onderzoek waarin CTP werd vergeleken met Rb-82 PET bij patiënten met een hoog risico op obstructieve CAD toonden een goede correlatie voor globale MBF<sup>39</sup>. Globale CTP-gebaseerde MBF-waarden bleken binnen 20% van Rb-82 PET-gebaseerde MBF-waarden te liggen. De op CTP-gebaseerde MFR werd echter wel systematisch onderschat<sup>39</sup>. Hoewel CTP nog verder geoptimaliseerd moet worden en er meer studies nodig zijn die de CTP vergelijken met PET en CMR voor de detectie van obstructieve CAD, is de toepassing van CTP interessant. Zo lijkt de combinatie van CTP en coronair computertomografie-angiografie (CCTA) in één onderzoek veelbelovend<sup>40</sup>. CCTA wordt vooral gebruikt om anatomisch de omvang en ernst van een mogelijke stenose te bepalen, maar is minder geschikt voor het beoordelen van de hemodynamische significantie van een mogelijke stenose<sup>41</sup>. Het gebruik van CCTA en CTP in één onderzoek resulteert in zowel anatomische als functionele informatie. Dit zou een volgende stap kunnen zijn in de niet-invasieve workflow van patiënten met verdenking op obstructieve CAD. Bovendien is het waarschijnlijk dat CTP leidt tot lagere kosten in vergelijking met Rb-82 PET of CMR. Daarnaast is een CT scanner vaker en sneller beschikbaar dan een PET of MRI scanner wat het gebruik van CTP toegankelijk maakt. Dit roept de vraag op of CTP in de toekomst PET en CMR zal vervangen in de detectie van obstructieve CAD.

**Kunstmatige intelligentie in cardiale beeldvorming**

De interesse en het gebruik van AI in de nucleaire geneeskunde is in opkomst en kan worden toegepast in het gehele proces van cardiale beeldvorming<sup>42</sup>. AI kan van toegevoegde waarde zijn bij de synthese en toediening van radiofarmaca, bij data-acquisitie, beeldreconstructie en analyse<sup>42</sup>. Het is bijvoorbeeld bekend dat een goede registratie tussen PET- en CT-beelden belangrijk is, omdat misregistratie kan leiden tot artefacten en onbetrouwbare MBF- en MFR-waarden<sup>43-45</sup>. Zo zou machine learning (ML), een onderdeel van AI dat zich toespitst op technieken waarmee computers kunnen bijleren op basis van ingevoerde data en patronen, de nauwkeurigheid van registratie tussen PET- en CT-gegevens kunnen verbeteren door niet alleen te corrigeren voor beweging van de patiënt, maar ook te corrigeren voor hart- en ademhalingsbewegingen<sup>46</sup>. Zoals aangetoond in dit proefschrift heeft een myocardiale verplaatsing een significante invloed op MBF- en MFR-metingen<sup>26</sup>. ML zou kunnen bijdragen aan automatische detectie en correctie van deze beweging. Dit zou tijd kunnen besparen en daarnaast de operatorvariabiliteit kunnen verminderen.

Daarnaast is de verwachting dat AI ook op andere gebieden voordelen zal leveren, zoals bij het stellen van een diagnose<sup>42</sup>. In hoofdstuk 9 hebben we laten zien dat ML in de detectie van obstructieve CAD veelbelovend is en kan worden ingezet als een risicofratificatie-model. Het gebruik van AI bij cardiale beeldvorming zou zelfs een stap verder kunnen gaan dan 'slechts' risicofratificatie. Het is niet ondenkbaar dat ML artsen zou kunnen assisteren bij het bepalen van de beste behandelstrategie door te voorspellen welke patiënten het meeste baat zullen hebben bij bijvoorbeeld medicatie of revascularisatie.

Hoewel AI veelbelovend lijkt op het gebied van nucleaire geneeskunde, zijn er ook enkele zorgen over de generaliseerbaarheid van modellen, de reproduceerbaarheid van resultaten en onvoldoende transparantie over de ontwikkeling van het algoritme<sup>42</sup>. Deze zorgen kunnen mogelijk worden weggenomen door in ieder geval een hogere technische standaard te eisen voor onderzoeken die betrekking hebben op de ontwikkeling van een AI-algoritme en voor onderzoeken die ontwikkelde modellen evalueren<sup>42, 47</sup>. Samengevat, AI heeft het potentieel om de nucleaire geneeskunde, maar ook de gezondheidszorg in het algemeen, aanzienlijk te verbeteren.

## REFERENCES

1. Mc Ardle BA, Dowsley TF, deKemp RA, Wells GA, Beanlands RS. Does rubidium-82 PET have superior accuracy to SPECT perfusion imaging for the diagnosis of obstructive coronary disease?: A systematic review and meta-analysis. *J Am Coll Cardiol.* 2012;60:1828-37.
2. Ziadi MC, deKemp RA, Williams KA, Guo A, Chow BJ, Renaud JM, et al. Impaired myocardial flow reserve on rubidium-82 positron emission tomography imaging predicts adverse outcomes in patients assessed for myocardial ischemia: Cardiac imaging. 2011;58:740-8.
3. Murthy VL, Naya M, Foster CR, Hainer J, Gaber M, Di Carli G, et al. Improved cardiac risk assessment with noninvasive measures of coronary flow reserve. *Circulation.* 2011;124:2215-24.
4. Zigray H, Elman S, Cheng RK, Li S, Lee J, Soine L, et al. Patient factors and outcomes associated with discordance between quantitative and qualitative cardiac PET ischemia information. 2021;16:Epub ahead of print doi:10.1371/journal.pone.0246149.
5. Murthy V, Bateman T, Beanlands R, Berman D, Borges-Neto S, Chareonthaitawee P, et al. Clinical quantification of myocardial blood flow using PET: Joint position paper of the SNMMI cardiovascular council and the ASNC. *J Nucl Cardiol.* 2018;25:269-97.
6. Sciagra R, Passeri A, Bucerus J, Verberne HJ, Slart, Riemer H. J. A., Lindner O, et al. Clinical use of quantitative cardiac perfusion PET: Rationale, modalities and possible indications. position paper of the cardiovascular committee of the european association of nuclear medicine (EANM). *Eur J Nucl Med Mol Imaging.* 2016;43:1530-45.
7. Ziadi MC. Myocardial flow reserve (MFR) with positron emission tomography (PET)/computed tomography (CT): Clinical impact in diagnosis and prognosis. *Cardiovasc Diagn Ther.* 2017;7:206-18.
8. Moody J, Lee B, Corbett J, Ficaro E, Murthy V. Precision and accuracy of clinical quantification of myocardial blood flow by dynamic PET: A technical perspective. *J Nucl Cardiol.* 2015;22:935-51.
9. Hoff CM, Sørensen J, Christensen NL, Bouchelouche K, Tolbod L. Activity regimes for 82Rb cardiac PET: Effects on absolute MBF and MPI. 2020:Epub ahead of print doi:10.1007/s12350-020-02266-2.
10. van Dijk J, Jager P, van Osch J, Khodaverdi M, van Dalen J. Comparison of maximal rubidium-82 activities for myocardial blood flow quantification between digital and conventional PET systems. *J Nucl Cardiol.* 2019;26:1286-91.
11. Renaud JM, Yip K, Guimond J, Trottier M, Pibarot P, Turcotte E, et al. Characterization of 3-dimensional PET systems for accurate quantification of myocardial blood flow. *J Nucl Med.* 2017;58:103-9.
12. deKemp RA, Yoshinaga K, Beanlands RSB. Will 3-dimensional PET-CT enable the routine quantification of myocardial blood flow? *J Nucl Cardiol.* 2007;14:380-97.
13. Slomka PJ, Pan T, Germano G. Recent advances and future progress in PET instrumentation. *Semin Nucl Med.* 2016;46:5-19.
14. Miller M, Zhang J, Binzel K, Griesmer J, Laurence T, Narayanan M, et al. Characterization of the vereos digital photon counting PET system. *J Nucl Med.* 2015;56(supplement 3):434.
15. van Sluis JJ, de Jong J, Schaar J, Noordzij W, van Snick P, Dierckx R, et al. Performance characteristics of the digital biograph vision PET/CT system. *J Nucl Med.* 2019;60:1031-6.

16. Hsu DFC, Ilan E, Peterson WT, Uribe J, Lubberink M, Levin CS. Studies of a next-generation silicon-Photomultiplier–Based time-of-flight PET/CT system. *J Nucl Med*. 2017;58:1511-8.
17. Slomka PJ, Pan T, Berman DS, Germano G. Advances in SPECT and PET hardware. *Prog Cardiovasc Dis*. 2015;57:566-78.
18. Van der Vos, CS, Koopman D, Rijnsdorp S, Arends AJ, Boellaard R, van Dalen JA, et al. Quantification, improvement, and harmonization of small lesion detection with state-of-the-art PET. *Eur J Nucl Med Mol Imaging*. 2017;44:4-16.
19. Memmott M, Tonge C, Saint K, Arumugam P. Impact of pharmacological stress agent on patient motion during rubidium-82 myocardial perfusion PET/CT. *J Nucl Cardiol*. 2018;25:1286-95.
20. Hunter, Chad R. R. N., Klein R, Beanlands RS, DeKemp RA. Patient motion effects on the quantification of regional myocardial blood flow with dynamic PET imaging. 2016;43:1829-40.
21. Koshino K, Watabe H, Enmi J, Hirano Y, Zeniya T, Hasegawa S, et al. Effects of patient movement on measurements of myocardial blood flow and viability in resting 15O-water PET studies. *J Nucl Cardiol*. 2012;19:524-33.
22. Piccinelli M, Votaw JR, Garcia EV. Motion correction and its impact on absolute myocardial blood flow measures with PET. *Curr Cardiol Rep*. 2018;20:1-8.
23. Friedman J, Train KV, Maddahi J, Rozanski A, Prigent F, Bietendorf J, et al. “Upward creep” of the heart: A frequent source of false-positive reversible defects during thallium-201 stress-redistribution SPECT. 1989;30:1718.
24. Scigrà R, Lubberink M, Hyafil F, Saraste A, Slart, Riemer H. J. A, Agostini D, et al. EANM procedural guidelines for PET/CT quantitative myocardial perfusion imaging. *Eur J Nucl Med Mol Imaging*. 2021;48:1040-69.
25. Koenders SS, van Dijk JD, Jager PL, Mouden M, Tegelaar AG, Slump CH, et al. Effect of temporal sampling protocols on myocardial blood flow measurements using rubidium-82 PET. *J Nucl Cardiol*. 2022;29;1729-41.
26. Koenders SS, van Dijk JD, Jager PL, Ottervanger JP, Slump CH, van Dalen JA. Impact of regadenoson-induced myocardial creep on dynamic rubidium-82 PET myocardial blood flow quantification. *J Nucl Cardiol*. 2019;26:719-28.
27. Koenders SS, van Dalen JA, Jager PL, Knollemans S, Timmer JR, Mouden M, et al. Value of SiPM PET in myocardial perfusion imaging using rubidium-82. *J Nucl Cardiol*. 2020.
28. Boellaard R, O’Doherty MJ, Weber WA, Mottaghy FM, Lonsdale MN, Stroobants SG, et al. FDG PET and PET/CT: EANM procedure guidelines for tumour PET imaging: Version 1.0. *Eur J Nucl Med Mol Imaging*. 2010;37:181-200.
29. Boellaard R, Delgado-Bolton R, Oyen WJ, Giammarile F, Tatsch K, Eschner W, et al. FDG PET/CT: EANM procedure guidelines for tumour imaging: Version 2.0. *Eur J Nucl Med Mol Imaging*. 2015;42:328-54.
30. Kamphuis ME. 2022 Quantitative myocardial perfusion imaging: A novel multimodality validation phantom. (Doctoral dissertation) University of Twente <https://doi.org/10.3990/1.9789036553780>.
31. Maddahi J, Lazewatsky J, Udelson JE, Berman DS, Beanlands RS, Heller GV, et al. Phase-III clinical trial of fluorine-18 flurpiridaz positron emission tomography for evaluation of coronary artery disease. *J Am Coll Cardiol*. 2020;76:391-401.



32. Patel KK, Singh A, Bateman TM. The potential of F-18 flurpiridaz PET/CT myocardial perfusion imaging for precision imaging. *Curr Cardiol Rep.* 2022;1-8.
33. Maddahi J, Packard RRS. Cardiac PET perfusion tracers: Current status and future directions. *Semin Nucl Med.* 2014;44:333-43.
34. Maddahi J, Czernin J, Lazewatsky J, Huang S-, Dahlbom M, Schelbert H, et al. Phase I, first-in-human study of BMS747158, a novel 18F-labeled tracer for myocardial perfusion PET: Dosimetry, biodistribution, safety, and imaging characteristics after a single injection at rest. 2011;52:1490-8.
35. Berman DS, Maddahi J, Tamarappoo BK, Czernin J, Taillefer R, Udelson JE, et al. Phase II safety and clinical comparison with single-photon emission computed tomography myocardial perfusion imaging for detection of coronary artery disease. 2013;61:469.
36. Montalescot G, Sechtem U, Achenbach S, Andreotti F, Arden C, Budaj A, et al. 2013 ESC guidelines on the management of stable coronary artery disease: The task force on the management of stable coronary artery disease of the European Society of Cardiology. *Eur Heart J.* 2013;34:2949-3003.
37. Knuuti J, Ballo H, Juarez-Orozco LE, Saraste A, Kolh P, Rutjes AWS, et al. The performance of non-invasive tests to rule-in and rule-out significant coronary artery stenosis in patients with stable angina: A meta-analysis focused on post-test disease probability. *Eur Heart J.* 2018;39:3322-30.
38. Jaarsma C, Leiner T, Bekkers SC, Crijns HJ, Wildberger JE, Nagel E, et al. Diagnostic performance of noninvasive myocardial perfusion imaging using single-photon emission computed tomography, cardiac magnetic resonance, and positron emission tomography imaging for the detection of obstructive coronary artery disease A meta-analysis. *JACC.* 2012;59:1719-28.
39. Alessio AM, Bindschadler M, Busey JM, Shuman WP, Caldwell JH, Branch KR. Accuracy of myocardial blood flow estimation from dynamic contrast-enhanced cardiac CT compared with PET. *Circ Cardiovasc Imaging.* 2019;12:e008323.
40. Nakamura S, Kitagawa K, Goto Y, Omori T, Kurita T, Yamada A, et al. Incremental prognostic value of myocardial blood flow quantified with stress dynamic computed tomography perfusion imaging. *J Am Coll Cardiol.* 2019;12:1379-87.
41. Schuijff JD, Wijns W, Jukema JW, Atsma DE, de Roos A, Lamb HJ, et al. Relationship between noninvasive coronary angiography with multi-slice computed tomography and myocardial perfusion imaging. *J Am Coll Cardiol.* 2006;48:2508-14.
42. Bradshaw TJ, Boellaard R, Dutta J, Jha AK, Jacobs P, Li Q, et al. Nuclear medicine and artificial intelligence: Best practices for algorithm development. *J Nucl Med.* 2022;63:500-10.
43. Rajaram M, Tahari AK, Lee AH, Lodge MA, Tsui B, Nekolla S, et al. Cardiac PET/CT misregistration causes significant changes in estimated myocardial blood flow. *J Nucl Med.* 2013;54:50-4.
44. Martinez-Moller A, Souvatzoglou M, Navab N, Schwaiger M, Nekolla SG. Artifacts from misaligned CT in cardiac perfusion PET/CT studies: Frequency, effects, and potential solutions. *J Nucl Med.* 2007;48:188.
45. Loghin C, Sdringola S, Gould KL. Common artifacts in PET myocardial perfusion images due to attenuation-emission misregistration: Clinical significance, causes, and solutions. *J Nucl Med.* 2004;45:1029.

46. Slart RH, Williams MC, Juarez-Orozco LE, Rischpler C, Dweck MR, Glaudemans AW, et al. Position paper of the EACVI and EANM on artificial intelligence applications in multimodality cardiovascular imaging using SPECT/CT, PET/CT, and cardiac CT. *Eur J Nucl Med Mol Imaging*. 2021;48:1399-413.
47. Jha AK, Bradshaw TJ, Buvat I, Hatt M, Prabhat KC, Liu C, et al. Nuclear medicine and artificial intelligence: Best practices for evaluation (the RELAINCE guidelines). *J Nucl Med*. 2022.





2.9

1.1

2.9

2.2

2.3

1.2

2.9

2.9

1.4

2.6

1.7

2.9

1.3

2.7

1

2.9

2.8

5

1.5

2.9

2.9

2.1

1

2.9

2

2.6

2.9

2.2

1.7

2.9

2

2.9

2.9

1.2

2.9

2.9

2.9

2.3

1.8

2.9

1.1

2.9

1

2.9

1.1

2.4

1.9

1

1.8

2

2.5

# APPENDICES

**LIST OF ABBREVIATIONS**

AI	Artificial intelligence
ASIR	Adaptive statistical iterative reconstruction
AUC	Area under the curve
BMI	Body mass index
CABG	Coronary artery bypass grafting
CACS	Coronary artery calcium scoring
CAD	Coronary artery disease
CCTA	Coronary computed tomography angiography
CMR	Cardiac magnetic resonance
CT	Computed tomography
CTP	Computed tomography perfusion
EANM	European Association of Nuclear Medicine
EARL	EANM research ltd
ECG	Electrocardiogram
F-18	Fluorine-18
FBV	Fractional blood volume
ICA	Invasive coronary angiography
LAD	Left anterior descending
LCX	Left circumflex
LV	Left ventricle
MBF	Myocardial blood flow
MFR	Myocardial flow reserve
ML	Machine learning
MPI	Myocardial perfusion imaging
N-13	Nitrogen-13
NaCl	Sodium chloride
O-15	Oxygen-15
OSEM	3D-ordered subset expectation maximization
PCI	Percutaneous coronary intervention
PET	Positron emission tomography
PMT	Photomultiplier tube
Rb-82	Rubidium-82
RC	Recovery coefficient
RCA	Right coronary artery
ROC	Receiver-operating characteristic
ROI	Region of interest
SD	Standard deviation
SiPM	Silicon photomultipliers

SPECT	Single photon emission computed tomography
Sr-82	Strontium-82
TAC	Time activity curve

## LIST OF PUBLICATIONS

### Peer-reviewed publications

1. S. S. Koenders, J. D. van Dijk MSc, P. L. Jager, J. P. Ottervanger, C. H. Slump, J. A. van Dalen. Impact of regadenoson-induced myocardial creep on dynamic Rubidium-82 PET myocardial blood flow quantification. *J. Nucl. Cardiol.* 2019 26:719–728.
2. S. S. Koenders, J.D. van Dijk, P.L. Jager, J.P. Ottervanger, C.H. Slump, J.A. van Dalen. How to detect and correct myocardial creep in myocardial perfusion imaging using Rubidium-82 PET? *J. Nucl. Cardiol.* 2019 26:729-734.
3. S.S. Koenders, J.A. van Dalen, P.L. Jager, S. Knollema, J.R. Timmer, M. Mouden, C.H. Slump, J.D. van Dijk. Value of SiPM PET in myocardial perfusion imaging using Rubidium-82. *J. Nucl. Cardiol.* 2020;Epub ahead of print doi:10.1007/s12350-020-02141-0.
4. S.S. Koenders, J.D. van Dijk, P.L. Jager, M. Mouden, A.G. Tegelaar, C.H. Slump, J.A. van Dalen. Effect of temporal sampling protocols on myocardial blood flow measurements using Rubidium-82 PET. *J Nucl Cardiol.* 2022;29;1729-41.
5. S.S. Koenders, J.A. van Dalen, P.L. Jager, M. Mouden, C.H. Slump, J.D. van Dijk. Diagnostic value of regional myocardial flow reserve measurements using Rubidium-82 PET. *Int J Cardiovasc Imaging.* 2022;Epub ahead of print doi:10.1007/s10554-022-02644-6.

### Non-peer reviewed articles

6. S.S. Koenders, J.A. van Dalen, J.D. van Dijk. The next step in improving (semi-)quantitative MPI PET. *J Nucl Cardiol.* 2020, Sep 17, Epub ahead of print.

### Conference proceedings

7. S.S. Koenders, J.D. van Dijk, P.L. Jager, C.H. Slump, J. P. Ottervanger, J.A. van Dalen. Need for correction of myocardium movement during dynamic Rubidium-82 stress PET for accurate myocardial blood flow quantification. Oral presentation at the annual meeting of the European Association of Nuclear Medicine 2017, Vienna.
8. J. A. van Dalen, J. D. van Dijk, J. van Osch, S.S. Koenders, L. Poot, P. L. Jager. A simple alternative to compartment models for myocardial flow reserve measurements using Rubidium-PET. ePoster presentation at the annual meeting of the European Association of Nuclear Medicine 2018, Düsseldorf.
9. S.S. Koenders, J.D. Van Dijk, P.L. Jager, J.P. Ottervanger, C.H. Slump, J.A. Van Dalen. Minimization of temporal sampling for myocardial blood flow quantification using Rubidium-82 PET. Poster presentation at the International Conference on Nuclear Cardiology and Cardiac CT, 2019, Lisbon.
10. S.S. Koenders, J.A. Van Dalen, P.L. Jager, M. Mouden, C.H. Slump, J.D. Van Dijk. Feasibility of a digital PET system for myocardial blood flow quantification using Rubidium-82 PET. Poster presentation at the International Conference on Nuclear Cardiology and Cardiac CT, 2019, Lisbon.



11. S.S. Koenders, J.D. Dijk, P.L. Jager, H. Arkies, J.R. Timmer, M. Mouden, C.H. Slump, J.A. Dalen. Favorable image reconstruction for adequate myocardial perfusion imaging using Rubidium-82 on a digital PET system. ePoster presentation at the annual meeting of the European Association of Nuclear Medicine 2019, Barcelona.
12. S.S. Koenders, J.A. Dalen, P.L. Jager, S. Knollema, J.R. Timmer, C.H. Slump, J.D. van Dijk. Value of Digital PET in Myocardial Perfusion Imaging Using Rubidium-82 PET. Oral presentation at the annual meeting of the European Association of Nuclear Medicine 2019, Barcelona.
13. S.S. Koenders, J.D. van Dijk, P.L. Jager, M. Mouden, C.H. Slump, A.G. Tegelaar, J.A. van Dalen. Effect of temporal sampling on myocardial blood flow measurements using Rubidium-82 PET. Virtual oral presentation at the annual meeting of the European Association of Nuclear Medicine 2020.
14. A.G. Tegelaar, S.S. Koenders, D. Koopman, P.G. Sanches, B.N. Vendel, H. Arkies, J.A. van Dalen. Dose reduction in FDG-PET by reconstruction optimization using resolution modelling. Virtual oral presentation at the annual meeting of the European Association of Nuclear Medicine 2020, Second best oral presentation technologists.
15. S.S. Koenders, J.A. van Dalen, P.L. Jager, M. Mouden, C.H. Slump, J.D. van Dijk. Value of regional myocardial flow measurements using Rubidium-82 PET. Virtual oral presentation at the International Conference on Nuclear Cardiology and Cardiac CT, 2021. Selected as a Young Investigator Finalist.
16. J.A. Van Dalen, S.S. Koenders, B.N. Vendel, P.L. Jager, J.D. Van Dijk. Entropy-based myocardial blood flow measurements using PET: a way to improve reproducibility. ePoster presentation at the International Conference on Nuclear Cardiology and Cardiac CT, 2021.

## CURRICULUM VITAE

Sabine Koenders was born on October the 30th 1993 in Almelo, The Netherlands. She graduated from secondary school in 2012 at Pius X College in Almelo. Afterwards she started with the bachelor Technical Medicine, from which she received the undergraduate degree in 2015. She continued with the master Technical Medicine (Medical Imaging and Interventions). During the second year of the master program she completed four 10-week internships at the departments of radiology (Radboudumc), Orthopedics (OCON orthopedic clinic at ziekenhuisgroep Twente), obstetrics & gynaecology (Radboudumc) and nuclear medicine (Isala). She also performed her clinical graduation assignment at the nuclear medicine department of Isala. Her graduation assignment was continued as she started as a PhD candidate. The PhD project focused on optimization and clinical value of myocardial blood flow quantification using Rubidium-82 PET. Her PhD supervisors were dr. Joris D. van Dijk, MSc, MBA, dr. Jorn A. van Dalen en dr. Pieter L. Jager, all representing Isala and prof. dr. ir. Cornelis H. Slump from the University of Twente.





## DANKWOORD

Het is zo ver, voor jullie ligt mijn proefschrift! Dit proefschrift was niet tot stand gekomen zonder de hulp en steun van mijn collega's, vrienden en familie. Ik wil graag een aantal personen specifiek bedanken.

Ik wil beginnen met mijn (co)-promotoren. Beste promotor, Prof. dr. ir. C.H. Slump, beste Kees, bedankt voor uw supervisie tijdens mijn stages, afstuderen en nu ook mijn promotietraject. U weet tot in de kleinste details feedback te geven wat ik waardeer. Ook wil ik dr. J.D. van Dijk, MSc, MBA en dr. J.A. van Dalen bedanken. Beste Joris en Jorn, tijdens mijn M2 stage was ik er al vrij snel uit (volgens mij na 2 à 3 weken al) dat ik jullie begeleiding erg prettig vond en graag bij jullie wilde afstuderen. Gelukkig zagen jullie dit ook zitten en wie had toen gedacht dat dit zelfs heeft geleid tot mijn PhD traject met als resultaat dit proefschrift? Ik niet! Ik wil jullie bedanken voor al jullie kennis en input die jullie geleverd hebben. De afgelopen jaren heb ik veel van jullie mogen leren en heb ik een hele leuke tijd gehad. Joris, jouw aanstekelijke enthousiasme en positiviteit hebben me meerdere malen weer motivatie gegeven om vol energie door te gaan. Jorn, de rust en positiviteit die je uitstraalt maakt dat ik onze samenwerking altijd erg prettig vond. Ik wil jullie bedanken voor jullie vertrouwen. Jullie waren altijd toegankelijk wat ik als erg prettig heb ervaren. Jullie hebben een grote bijdrage geleverd aan mijn artikelen en daarmee ook dit proefschrift.

Dr. P.L. Jager, beste Piet, bedankt voor jouw kritische maar zinvolle input op klinisch en wetenschappelijk gebied de afgelopen jaren. Ook jij hebt op deze manier een grote bijdrage geleverd aan mijn artikelen en daarmee ook dit proefschrift, dank daarvoor.

Ik wil graag de promotiecommissie bedanken voor het nemen van de tijd om mijn proefschrift te lezen en voor het deelnemen aan mijn verdediging.

Ook wil ik graag mijn (voormalige) research collega's van de Nucleaire Geneeskunde en Cardiologie bedanken. Siert, bedankt voor het mogelijk maken van mijn promotietraject. Brian, Tonke, Daniëlle, Jochen, Mohamed, Jorik, Jan Paul en Nanette bedankt voor jullie hulp bij mijn onderzoek en de leuke tijd de afgelopen jaren. Mandy, bedankt voor de gezelligheid, je hulp en de vele serieuze maar zeker ook minder serieuze gesprekken onder het genot van een goede kop cappuccino. Ik wens jou veel succes bij het voortzetten van jouw promotieonderzoek!

Daarnaast wil ik al mijn andere collega's, waaronder alle artsen, PA'ers, OL'ers, laboranten, administratie en voormalige TG-studenten van de Nucleaire Geneeskunde van Isala bedanken. Bedankt voor de ondersteuning en hulp bij mijn onderzoek de afgelopen jaren, voor de leuke tijd en gezelligheid tijdens congressen! Dames van de werkkamer, vele uren zaten we samen in de werkkamer met Qmusic op de achtergrond. De serieuze gesprekken, maar ook zeker de kletspraatjes maakten dat ik met veel plezier naar mijn werk ging. Alina, ook jou wil ik bedanken voor de behulpzame en leuke maandelijkse "interview" momenten. Rutger, bedankt voor al jouw werk en hulp dat geleid heeft tot hoofdstuk 9 van dit proefschrift.

Dan mijn paranimfen Aline en Lisan. Aline bedankt dat je altijd klaar stond om mijn praktische vragen te beantwoorden en te helpen bij het uitvoeren van verschillende onderzoeken. Ik ben blij dat ik de afgelopen jaren heb mogen werken met een collega zoals jij en dat je vandaag als paranimf naast mij staat. Lisan, sinds de kleuterklas ben je al één van mijn beste vriendinnen. Ik ben blij dat we nu nog steeds mooie herinneringen samen maken. Ik vind het dan ook erg fijn dat je vandaag als paranimf naast mij staat. Op naar nog veel meer mooie momenten en herinneringen!

Maartje, bedankt voor al je hulp bij het opmaken van mijn proefschrift. Zonder jou was mijn proefschrift lang niet zo mooi geworden, ik ben erg blij met het resultaat!

Ook wil ik mijn lieve vriendinnen “Vrouwkes”, bedanken voor jullie interesse en vriendschap. Ook al zien we elkaar niet wekelijks, het is altijd een erg gezellige boel als we samen zijn.

Dan Papa, Mama, Hans en (schoon)familie bedankt voor jullie interesse en betrokkenheid! Lieve Pap en Mam bedankt voor jullie onvoorwaardelijke liefde en vertrouwen in mij. Ik ben jullie erg dankbaar voor alles.

Last but not least, lieve Nolan bedankt dat je er altijd voor mij bent. Ik houd ervan dat wij hetzelfde in het leven staan en kunnen genieten van dezelfde dingen. Samen met jou is alles leuker. Ik kijk uit naar onze toekomst samen! ♥











